Université de Sherbrooke

Faculté de génie

Département de génie chimique et de génie biotechnologique

Modélisation et simulation des piles aux lithium ions

Thèse de doctorat

Spécialité : génie chimique

Sara Taslimi Taleghani

Jury : Prof. Bernard Marcos (directeur)

Dr. Gaétan Lantagne (codirecteur)

Prof. Martin Désilets

Prof. João Pedro Trovao

Dr. Chisu Kim

Sherbrooke (Québec) Canada Avril 2019

À mes parents

À mes sœurs, Sahar et Setareh

Et à mon mari, Farhad

Résumé

Aujourd'hui, les batteries au lithium-ion (Li-ion) en tant que sources de stockage d'énergie sont largement utilisées dans différentes technologies de pointe, telles que l'aérospatiale, le médical, l'automobile, les appareils photo numériques et les téléphones portables, en raison de leurs caractéristiques spécifiques dont la haute densité de puissance/énergie et leur durabilité. Le développement de telles batteries dans l'industrie automobile peut aider à diminuer les préoccupations concernant l'épuisement des combustibles fossiles et les problèmes environnementaux attribués à l'émission de dioxyde de carbone.

Malgré leur temps de calcul plus élevé, les modèles de batteries basés sur la physique comme le modèle pseudo-bidimensionnel (P2D) sont plus fiables et plus robustes que les autres modèles de batteries. Ces modèles comprennent différents mécanismes de transport de charges et d'espèces en phases solide et solution, ainsi que la cinétique de réaction à l'interface solide-solution. Comprendre ces phénomènes est un facteur crucial pour concevoir, optimiser et contrôler les cellules Li-ion.

La performance de la batterie est considérablement affectée par ses propriétés structurelles. Le développement de nouveaux matériaux d'électrode et de nouvelles structures sont d'une importance significative pour les concepteurs de batteries afin d'améliorer leur efficacité. Alors qu'une électrode est composée de particules de différentes tailles, la plupart des modèles dans la littérature utilisent des électrodes avec des particules de même taille (modèle monomodale) pour simplifier les calculs. L'un des principaux objectifs de cette thèse est de comprendre les effets de propriétés structurelles, telles que la distribution granulométrique et la porosité de l'électrode sur le voltage, l'énergie spécifique, la puissance spécifique et la polarisation totale d'une cellule composée des électrodes Graphite et $Li_yMn_2O_4$. En outre, cette thèse quantifiera l'influence de la position des particules dans la morphologie de l'électrode positive sur la performance de la cellule.

La sécurité est un problème essentiel pour les fabricants de batteries. La température résultant de la chaleur générée peut diminuer la performance de la cellule et entraîner un emballement thermique et même une explosion dans le cas le plus défavorable. Par conséquent, le développement d'un modèle de couplage électrothermique robuste qui peut prédire les comportements électrochimiques et thermiques à travers la cellule est crucial pour les concepteurs de batteries. La polarisation ou la perte de potentiel dans chaque partie d'une cellule peut contribuer à la génération de chaleur. Ainsi, connaître chaque polarisation à l'intérieur de la cellule et trouver les principaux facteurs limitant la performance de la cellule peuvent fournir aux concepteurs de batteries de nouvelles connaissances qui les aideront dans leur conception. Un autre objectif de ce projet est de développer un modèle électrochimique pour une cellule cylindrique commerciale de graphite - $LiFePO_4$ (LFP) afin de trouver les principaux mécanismes de transport contrôlant la performance de la cellule pendant le processus de décharge. Le modèle électrochimique est alors couplé à un modèle thermique pour déterminer la contribution de chaque polarisation dans la chaleur totale générée. Les résultats simulés sont validés avec des données expérimentales fournies par Hydro-Québec.

Mots clés: Piles Li-ion, Modèle P2D, Mécanismes de transport, Modèle monomodale, Granulométrie, Porosité, Position des particules, Chaleur totale générée, Performance de cellule, Modèle de couplage électrothermique, Polarisation, Cellule cylindrique de Graphite-LFP, Processus de décharge

Remerciements

Je voudrais sincèrement remercier mon superviseur Pr. Bernard Marcos et mon co-directeur, Dr. Gaétan Lantagne, pour leurs précieux conseils, leur soutien et leurs encouragements durant cette recherche. Vos conseils bienveillants et vos pensées positives m'ont toujours motivé à poursuivre mon travail plus sérieusement.

Je voudrais remercier le professeur Pr. Martin Désilets d'organiser les réunions du groupe de la batterie et de me donner l'occasion de partager des informations avec d'autres membres et d'utiliser d'autres expériences.

Je voudrais exprimer ma profonde gratitude aux membres de mon comité : Prof. Martin Désilets, Prof. João Pedro Trovao and Dr. Kim, pour leurs suggestions et commentaires perspicaces à améliorer cette thèse.

De plus, j'aimerais remercier le Dr Karim Zaghib d'Hydro-Québec pour ses conseils.

J'apprécie vraiment tous mes amis qui m'ont aidé pendent ces années et m'ont fourni un environnement amical.

Enfin et surtout, je voudrais exprimer mes sincères remerciements à mes parents compatissants, à mes sœurs, à mon beau-frère et à mon époux pour leur motivation et leur soutien émotionnel. Les mots ne peuvent exprimer ma profonde gratitude pour toute votre aide tout au long de ma vie.

TABLE DES MATIÈRES

LISTE DES FIGURES

LISTE DES TABLEAUX

LISTE DES SYMBOLES

a	Surface spécifique, $\mathrm{m}^2/\mathrm{m}^3$
c	Concentration d'électrolyte, $\mathrm{mol}/\mathrm{m}^3$
c_1	Concentration de Li dans la phase solide, $\mathrm{mol}/\mathrm{m}^3$
c_1^0	Concentration initiale de Li dans la phase solide, $\mathrm{mol}/\mathrm{m}^3$
$c_{1,max}$	Concentration maximale de Li dans la phase solide, $\mathrm{mol}/\mathrm{m}^3$
c_i	Concentration d'espèces i, $\mathrm{mol}/\mathrm{m}^3$
c_{sl}	Concentration de solvant, $\mathrm{mol}/\mathrm{m}^3$
D	Coefficient de diffusion, m^2/s
$f_{\pm}$	Coefficient d'activité molaire moyenne du sel
F	La constante de Faraday, 96487, C/mol
i_0	Densité de courant d'échange, A/m^2
i_1	Densité de courant électronique de la phase solide, A/m^2
i_2	Densité de courant ionique de la solution, A/m^2
i_m	Densité de courant local, A/m^2
I	Densité de courant totale, A/m^2
j_m	Flux à l'interface du pore, $\mathrm{mol}/\mathrm{m}^2$ s
k	Taux de réaction constant, m/s
N_i	Flux molaire des espèces i, $\mathrm{mol}/\mathrm{m}^2$ s
r	Direction radiale, m
R	Constante universelle des gaz, 8.314 J/mol K
t	Temps, s
t_i^0	Nombre de transport d'espèces i
T	Température absolue, K
U	Potentiel du circuit ouvert, V
v	Vitesse, m/s
x	Direction spatiale, m
z_i	Nombre de charge d'espèces i

Grecque

α_a, α_c	Coefficients de transfert anodique et cathodique
ε	Fraction volumique ou porosité d'une phase
η	Surtension, V
κ	Conductivité de l'électrolyte, S/m
ν_i	Nombre d'espèces ioniques dans lesquelles une mole d'électrolyte se dissocie

σ	Conductivité électronique de la phase solide, $\mathrm{S/m}$
τ	Tortuosité
Φ	Potentiel électrique, V

Indices inférieurs

eff	Valeur effective de la propriété de transport en milieu poreux
neg	Électrode négative
pos	Électrode positive
sl	Solvant
1	Phase solide
2	Phase de solution

Indices supérieurs

0	Valeur initiale

CHAPITRE 1

Introduction

1.1 Batterie Li-ion

Récemment, de nouveaux systèmes d'énergie propre et renouvelable ont été développés pour réduire la pollution causée par la combustion de combustibles fossiles, ce qui entraîne l'émission de gaz à effet de serre dans l'atmosphère, résultant en un réchauffement de la planète et des changements climatiques importants. Un développement important a été réalisé dans les sources d'énergie renouvelables telles que l'énergie éolienne et solaire, qui sont des sources intermittentes. Ainsi, la nécessité de développer des dispositifs de stockage d'énergie est essentielle. Les batteries sont l'un des dispositifs de stockage électrochimique dans lesquels est stockée l'énergie sous forme de différence de potentiel chimique. La conversion de l'énergie libérée par des réactions chimiques spontanées en travail électrique est la base du fonctionnement de la batterie. Une batterie est composée de deux cellules ou plus qui sont connectées électriquement pour fournir la tension et la capacité requises.

Les batteries comme sources de stockage d'énergie ont été divisées en deux catégories; piles primaires et piles secondaires. Les piles primaires ou les piles à usage unique ne sont pas rechargeables, tandis que les piles secondaires rechargeables peuvent être utilisées plusieurs fois. Aujourd'hui, le développement des appareils électriques comme les téléphones portables, les ordinateurs portables et les véhicules a augmenté la demande en batteries rechargeables. Un exemple de ces batteries est la batterie Li-ion qui offre plus de performance et d'efficacité que des technologies alternatives. De plus, la haute densité d'énergie (100-265 Wh/kg or 250-670 Wh/L), la haute densité de puissance, le voltage d'utilisation élevé, le rapport élevé énergie/poids et la faible autodécharge des batteries Li-ion en ont fait des systèmes performants de stockage d'énergie. Le tableau 1.1 illustre les différences entre différents types de batteries [1].

Tableau 1.1: Comparaison entre différents types de batteries [1]

Batteries	Li-ion	Pb-Acide	Ni-Cd	Ni-MH
Durée de vie /Cycle	500~1000	200~500	500	500
Potentiel d'utilisation (V)	3.6	1.0	1.2	1.2
Énergie spécifique (Wh/kg)	100	30	60	70
Énergie volumique (Wh/L)	240	100	155	190

La figure 1.1 montre une représentation de la batterie Li-ion [2]. Les parties constitutives de la batterie sont un collecteur de courant en contact avec l'électrode négative, une électrode négative, un séparateur, un électrolyte, une électrode positive et un collecteur de courant en contact avec l'électrode positive. Les collecteurs de courant et le séparateur servent respectivement de

conducteurs électriques et ioniques. Pendant le processus de charge, une réaction d'oxydation se produit à la surface de l'électrode positive, les Li ions sont désintercalés de l'électrode positive et se dirigent vers l'électrode négative via un séparateur tandis que les électrons sont transférés dans la même direction (positive à négative) via un circuit externe. Le mouvement des électrons et des Li ions vers l'électrode négative entraîne une réaction de réduction à la surface de l'électrode négative. Un processus inverse se produit lors de la décharge d'une batterie.

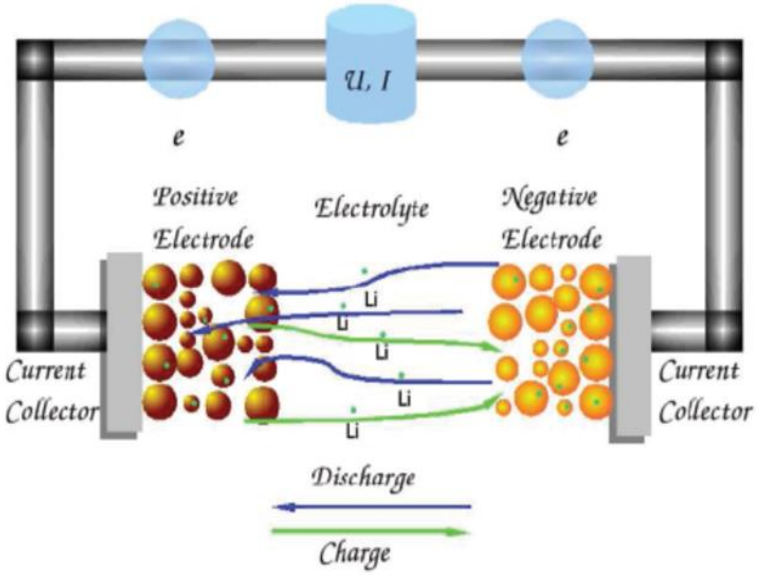

Figure 1.1: Schéma du mouvement des électrons et des Li ions pendant la charge et la décharge d'une batterie [2]

Les matériaux constitutifs des parties de la batterie doivent posséder des caractéristiques spécifiques. Les matériaux de l'électrode positive doivent pouvoir être incorporés avec de grandes quantités de Li pour augmenter la capacité. Ils ne devraient pas se développer/se contracter significativement pendant l'intercalation/désintercalation des ions Li pour atteindre une longue durée de vie. Ils doivent avoir une bonne diffusivité, une bonne conductivité électronique et ils ne doivent pas être solubles dans l'électrolyte. De plus, leur coût de synthèse devrait être faible. Les composés $LiMn_2O_4$ (LMO), $LiCoO_2$ (LCO) and $LiFePO_4$ (LFP) sont utilisés communément comme matériaux pour l'électrode positive. Une comparaison entre ces matériaux pour l'électrode positive est présentée dans le tableau 1.2 [3], [4]. Une électrode négative doit avoir une grande densité énergétique et une capacité élevée. Il ne devrait y avoir aucune intercalation de molécules de solvant dans sa structure menant à la perte de capacité. De plus, le faible coût et la non-toxicité sont d'autres facteurs pour sélectionner les électrodes négatives. Bien que le lithium métallique pur en tant qu'électrode négative fournisse une densité d'énergie efficace, sa réactivité élevée est un problème pour les batteries Li-ion. Il est donc remplacé par des composés de lithium, tels que LiAl and LiC_6. Aujourd'hui, le graphite est très répandu comme matériau d'électrode négative en raison de sa conductivité électrique élevée et de sa stabilité thermique. Le séparateur en tant que conducteur ionique doit être un isolant électronique et empêcher le contact direct entre deux électrodes. La solution électrolytique doit avoir une bonne conductivité ionique et être stable sur une large plage de potentiel. La solution électrolytique consiste généralement en un sel de lithium tel que $LiClO_4$, $LiPF_6$ et une

combinaison de solvants organiques comprenant le carbonate d'éthylène (EC), le carbonate de diméthyle (DMC), le carbonate de diéthyle (DEC) [5], [6].

Tableau 1.2: Comparaison entre les différentes électrodes positives [3], [4]

Chimie de la cellule	$LiCoO_2$	$LiFePO_4$	$LiMn_2O_4$
Tension nominale (Rate Voltage)	3.7 V	3.2 V	3.8 V
Voltage de charge	4.2 V	3.7 V	4.2 V
Voltage de fin de décharge	3.0 V	2.0 V	2.5 V
Energie volumique (Wh/L)	447	222	253
Energie spécifique (Wh/kg)	140-145	90-110	105-115
Capacité spécifique (mAh/g)	272	170	148
Durée de la vie/Cycle	>700	>1800	>500
Taux d'autodécharge (mois)	1%	0.05%	5%
Performance à haute température (55+/-2)	Bien	Excellent	Acceptable
Performance à basse température (-20+/-2)	Bien	Bien	Bien
Préoccupations liées à la sécurité et à l'environnement	Pauvre	Excellent	Bien

1.2 Description du projet de recherche

De nos jours, les batteries Li-ion jouent un rôle important dans les technologies automobiles et autres technologies avancées en raison de leurs caractéristiques distinctives telles que la densité d'énergie/de puissance élevée et la durée de vie. Elles sont développées en tant que sources alternatives de stockage d'énergie pour les combustibles fossiles. Parce que la compréhension des propriétés structurelles des batteries est un facteur clé et accélère le processus de commercialisation, le développement de modèles mathématiques pour estimer les meilleurs paramètres de conception est essentiel. Des modèles théoriques ont été développés pour décrire les phénomènes de transport et électrochimiques se produisant dans les batteries. La plupart de ces modèles ont été basés sur la distribution uniforme de la taille des particules pour l'électrode, qui est en contraste avec la réalité de la morphologie de l'électrode. Seuls quelques articles ont traité de ce sujet important, dont une revue détaillée de la littérature est présentée aux chapitres 3 et 4. Il est évident qu'une véritable électrode est composée de particules de différentes tailles situées à différentes positions. Ainsi, il est essentiel d'étendre le niveau de connaissances sur l'effet des distributions de la taille des particules, de la porosité et de la position des particules dans la morphologie de l'électrode sur la performance de cellule. En fait, notre question de recherche est définie comme suit: “Dans quelle mesure, ces propriétés structurelles peuvent affecter la performance de la cellule, comme le voltage de la cellule, la capacité de la cellule et l’énergie/puissance spécifique de la cellule? ”

La sécurité des batteries est une autre question clé pour les concepteurs de batteries. La polarisation ou la perte de potentiel à l'intérieur de la cellule peut provenir du transport de masse des espèces en phases solide et solution, de la chute de potentiel ohmique en phases solide et solution, de l'activation des réactions électrochimiques et du contact inadéquat entre les différentes parties de l'électrode. Parce que chaque polarisation contribue à la génération de

chaleur, dans une première étape, il est essentiel d'identifier et de comprendre les mécanismes de transport à l'intérieur de la cellule. Récemment, de nombreux chercheurs se sont concentrés sur le développement de modèles électrochimiques et thermiques pour décrire la dynamique de transport dans les batteries à base d'électrode LFP. Une revue de la littérature sur les modèles est présentée dans les chapitres 5 and 6. Elle a montré qu'il n'existe pas de modèle complet qui décrit les principales polarisations limitant la performance de la cellule et qui décrit l'effet des pertes de potentiel à l'intérieur de la cellule sur les problèmes thermiques de la cellule. Ainsi, un modèle électrochimique pour une cellule cylindrique commerciale de graphite-LFP est développé pour détecter les principaux mécanismes de transport contrôlant la performance de la cellule pendant le processus de décharge. Puis le modèle est combiné avec un modèle thermique pour déterminer la portion de la chaleur causée par chaque polarisation. Notre deuxième question de recherche peut être définie comme suit: "Pouvons-nous développer un modèle décrivant le comportement couplé électrochimique et thermique de la cellule, basé sur la reconnaissance des pertes internes survenant dans la cellule? "

1.3 Objectifs

Les principaux objectifs de cette thèse sont définis ci-dessous:

- l'étude de l'effet des propriétés structurelles de l'électrode positive ($Li_yMn_2O_4$) telles que la porosité et la distribution de la taille des particules, sur la performance de la cellule Li-ion en utilisant un modèle P2D pendant le processus de décharge. Trois distributions de tailles de particules comprenant des distributions de taille de monomodale, bimodale et 3 particules ont été sélectionnées pour comparer l'effet de chaque distribution sur le voltage, la polarisation totale, l'énergie spécifique et la puissance spécifique de la cellule.

- l'étude de l'effet de la position des particules dans une distribution bimodale de l'électrode positive sur le voltage de la cellule et les polarisations se produisant à l'intérieur de la cellule en utilisant un modèle P2D pendant le processus de décharge.

- le développement d'un modèle pour une cellule cylindrique commerciale de type graphite-LFP dans une gamme complète de taux de décharge (élevés et faibles) comprenant

    - la description du comportement électrochimique de la cellule Graphite-LFP dans la zone de plateau et la zone de pente raide à la fin de la décharge de la courbe voltage-capacité de la cellule;

    - l'étude en détails des phénomènes de transport se produisant à l'intérieur de la cellule pour prévoir les principales polarisations limitant la performance de la cellule lors de la décharge.

- le développement d'un modèle électrochimique-thermique en couplant le modèle électrochimique susmentionné à un modèle thermique pour

- analyser le comportement thermique d'une cellule cylindrique de Graphite-LFP pendant des taux élevés de décharge

- étudier l'effet de la prise en compte de la variation en fonction de la température des paramètres physicochimiques sur le voltage de la cellule et la température de la surface de la cellule

- prédire le pourcentage de la chaleur causée par chaque polarisation ou perte de potentiel se produisant dans plusieurs zones de la cellule sur l'ensemble de la chaleur produite

- Fournir à l'industrie de la fabrication de piles Li-ion, un outil pour la prédiction du comportement des piles en fonction de leur design et de leurs conditions d'opération.

1.4 Plan de thèse

Cette thèse consiste en sept chapitres comme suit:

- Le chapitre 2 expose une revue de la littérature de la modélisation des batteries Li-ion.

- L'effet des propriétés structurelles telles que la porosité et la distribution de la taille des particules sur les batteries à base d'électrodes de Graphite-$Li_yMn_2O_4$ est étudié en utilisant un modèle basé sur la physique (P2D model) au chapitre 3. Trois distributions de taille des particules comprenant des distributions monomodale, bimodale et composée de 3 tailles de particules dans l'électrode positive sont considérées et comparées. Les particules de différentes tailles sont considérées et sont supposées présentes en tous les points de l'électrode positive.

- Le chapitre 4 développe un modèle pour inclure l'effet de la position des particules selon une distribution bimodale de l'électrode positive sur la performance de la cellule. La validation du modèle mentionné dans les deux chapitres 3 et 4 se fait avec des données expérimentales et simulées de Doyle [7].

- Le chapitre 5 combine un modèle P2D avec un modèle mosaïque pour analyser les phénomènes de transport survenant dans une cellule cylindrique commerciale 18650 de graphite-LFP dans une plage de taux de décharge (C-rates). A partir de la reconnaissance des polarisations dans plusieurs zones de la cellule, les principaux mécanismes de transport limitant la performance de la cellule sont identifiés.

- Le chapitre 6 développe un modèle électrochimique et thermique pour inclure la contribution de chaque polarisation dans la chaleur totale générée pendant des décharges à taux élevés. En se référant au chapitre 5, les polarisations dans les différentes zones de la cellule comprennent la surtension d'activation, la polarisation de diffusion et la chute de potentiel ohmique dans les phases solide et solution. Dans ce modèle électrochimique-thermique, chaque polarisation contribue à la génération de chaleur. Ce modèle est utile pour comprendre le comportement thermique à travers une cellule. Les modèles présentés

aux chapitres 5 et 6 sont validés avec des données expérimentales fournies par Hydro-Québec.

- Finalement, le chapitre 7 présente les principales conclusions de la thèse et propose quelques pistes pour les travaux futurs.

CHAPITRE 2

L’état de l’art: Modélisation des batteries Li-ion

Les modèles mathématiques pour les batteries Li-ion sont classés en fonction de leur précision et de leurs complexités conceptuelles et computationnelles [8].

2.1 Modèles empiriques

Ces modèles sont basés sur des données expérimentales adaptées aux conditions spécifiques d'opération utilisant différentes fonctions d'approximations (polynôme, exponentiel, loi de puissance, logarithmique et trigonométrique) [9]. L'une des caractéristiques de ces modèles est leur faible temps de calcul. Cependant, ils ne sont pas adéquats lorsque différentes conditions d'opération ou de nouveaux matériaux sont appliqués [10]. Contrairement aux modèles d'ingénierie électrochimique, les modèles empiriques ne tiennent pas compte de la physique sous-jacente dans la dynamique de la batterie et ignorent plus généralement les principes physico-chimiques [11].

2.2 Modèles d'ingénierie électrochimique

Ces modèles sont plus précis que les modèles empiriques en raison de l'incorporation des phénomènes de transport et de la cinétique de réaction électrochimique pour prédire le comportement de la batterie. Trois types de modèles d'ingénierie électrochimique sont introduits en fonction de leur niveau de complexité:

2.2.1 Modèle de particule unique (SPM)

Ce modèle est un modèle simple dans lequel les gradients de la concentration et du potentiel en phase de solution sont négligés. Zhang et al. [12] ont modélisé le processus d'intercalation de Li-ion dans une particule unique. Ils ont considéré le mécanisme de diffusion dans la particule et la cinétique de réaction à l'interface particule / électrolyte sans tenir compte de la limitation du transport de l'électrolyte entre les particules. Santhanagopalan et al. [13] ont développé ce modèle en un sandwich simple dans lequel les électrodes négatives et positives étaient représentées comme une particule sphérique unique. La surface de chaque électrode était considérée comme égale à la surface active de la phase solide de l'électrode correspondante dans le modèle d'électrode poreuse. Ce modèle simplifié est rapide à résoudre informatiquement. Cependant, il n’est pas précis, car il ne prend pas en compte tous les phénomènes de transport. Pinson et al. [14] ont montré que la SPM, qui néglige la non-uniformité spatiale, est un modèle valide pour étudier la perte de capacité de la batterie dans des conditions limitées telles que des taux de charge / décharge faibles ou des électrodes minces. Rajabloo et al. ont introduit un modèle de SPM associé à une résistance empirique variable pour décrire les caractéristiques de faible conductivité ionique et électrique du LFP [15]. Une représentation du modèle de SPM est présentée à la Figure 2.1b [13].

2.2.2 Modèle d'électrode poreuse ohmique

Dans ce modèle, les potentiels des phases solide et électrolytique sont considérés tandis que les gradients de concentration sont négligés, ce qui est acceptable pour des particules de petite taille et pour tout système avec un nombre de transport égal à l'unité pour le Li-ion ($t^0 = 1$). Un modèle d'électrode poreuse ohmique a été utilisé dans les problèmes de conception et d'optimisation [16]–[18].

2.2.3 Modèle pseudo-bi-dimensionnel (P2D)

Le modèle pseudo-bidimensionnel (P2D) est une amélioration du modèle d'électrode poreuse ohmique dans lequel sont considérés les gradients de concentration et de potentiel dans les phases solide et électrolytique ainsi que la cinétique de réaction dans l'interface d'électrolyte-solide. Le modèle P2D considère uniquement le mécanisme de diffusion dans la direction r dans la phase solide, tandis que la concentration dans l'électrolyte et les potentiels des phases solide et électrolytique ne varient que dans la direction x. Doyle et al. [19] ont développé un modèle complet basé sur la théorie des solutions concentrées comprenant une électrode négative de Li, un électrolyte plastifié et une électrode positive composite d'insertion. Ce modèle basé sur les principes des phénomènes de transport, de l'électrochimie et de la thermodynamique est décrit par des équations différentielles partielles non linéaires (PDEs) en x, r, et t. La concentration de l'électrolyte, le potentiel d'électrolyte, le potentiel de la phase solide et la concentration de la phase solide dans les électrodes poreuses et la concentration d'électrolyte et le potentiel d'électrolyte dans le séparateur sont obtenus en résolvant numériquement ces équations. Bien que ce modèle soit plus précis que les modèles susmentionnés, il est plus exigeant en termes de temps calcul. Le modèle de Doyle [19] a été largement utilisé par d'autres chercheurs qui ont créé des modèles similaires, y compris d'autres développements dans les systèmes de batteries [13], [20]–[22]. Fuller et al. [23] ont appliqué ce modèle pour étudier la charge ainsi que la décharge galvanostatique d'une cellule à double insertion de Li ions (rocking-chair). Ramadass et al. [24] ont étendu cette approche pour tenir compte de la perte de capacité de la batterie. De plus, une revue des modèles P2D simplifiés des batteries Li-ion a été réalisé par Jokar et al [25]. La figure 2.1a montre une illustration d'un modèle P2D [13].

Les modèles P2D sont basés sur la théorie de solution concentrée et la théorie des électrodes poreuses:

- Théorie de la solution concentrée

Dans la théorie de la solution concentrée, toutes les espèces présentes dans la solution interagissent ensemble tandis que dans la théorie de la solution diluée, les interactions se produisent uniquement entre les ions et le solvant. De plus, les coefficients d'activité dans la théorie de la solution diluée sont supposés égal à l'unité [5]. La théorie de la solution concentrée semble être une hypothèse efficace pour le transport des électrolytes en raison des concentrations élevées de sel utilisées dans les batteries Li-ion (C>l M). Dans cette théorie, la force motrice du transfert de masse est le gradient de potentiel électrochimique pour une espèce ionique. L'hypothèse de neutralité de charge de la phase électrolyte est appliquée à la théorie de la solution concentrée en raison de sa concentration élevée de sel et conduit à un couplage fort du transport des charges et des ions [26].

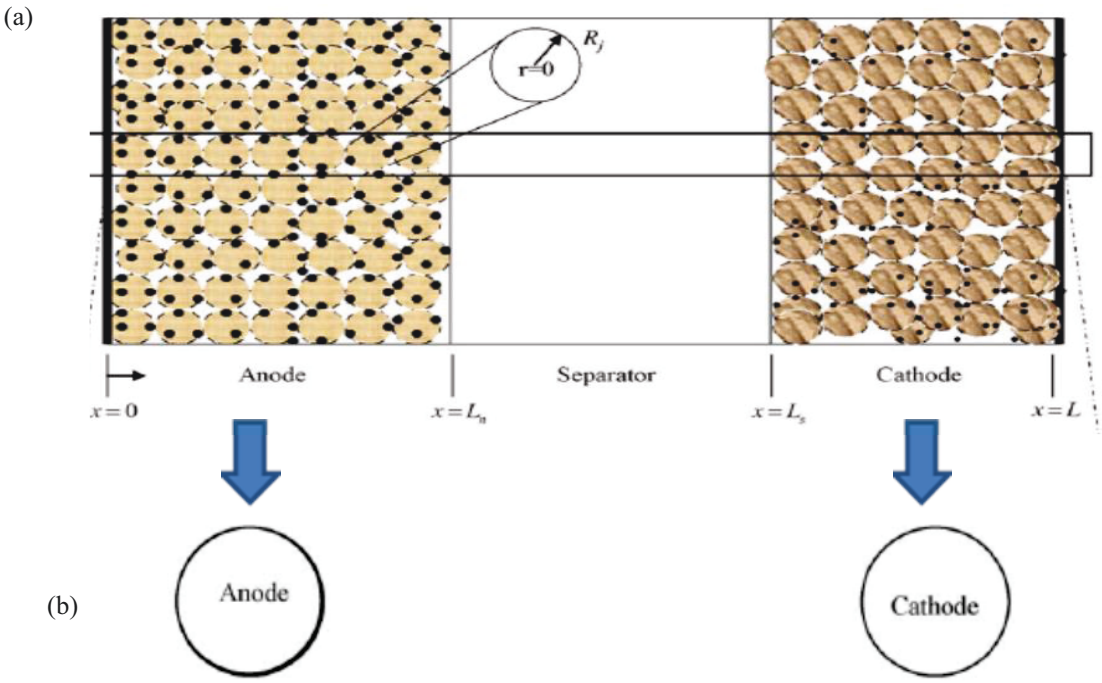

Figure 2.1: Représentation de (a) Modèle P2D (b) SPM [13]

- Théorie des électrodes poreuses

Newman et Tiedemann [27] ont révisé la théorie des électrodes poreuses. Cette théorie est utile en raison de la distance réduite entre les réactifs et la surface, en plus de la grande surface interfaciale de l'électrode poreuse qui améliore le taux de réaction de l'électrode. La théorie de l'électrode poreuse basée sur la technique du volume moyen a été une approche standard pour modéliser les batteries. Selon cette théorie, les propriétés sont moyennées sur un volume qui est petit comparé au volume global de l'électrode mais grand par rapport à la structure des pores. En fait, la géométrie détaillée des pores et les positions et formes exactes des particules dans l'électrode ne sont pas prises en compte. Par contre, une superposition de matière active, de remplisseur (filler) et d'électrolyte est observée et chaque phase a une fraction volumique spécifique. Les phases d'électrode et d'électrolyte sont couplées en raison des équations de bilan de masse et des cinétiques de réaction. Cette théorie a été la base du travail de nombreux chercheurs [19], [23], [28], [29].

2.2.3.1 Équations gouvernantes

Les équations suivantes utilisées dans le modèle P2D sont résumées dans les tableaux 3.2, 3.3, 4.2, 5.1 et 6.2 [19].

- Équations de transport en phase solution pour un électrolyte concentré binaire de sel (Li^+, PF_6^-)

Un électrolyte binaire se compose seulement d'un type d'espèces chargées positivement (cations) et d'un type d'espèces chargées négativement (anions). Le flux molaire (N_i) composé de trois phénomènes de transport, la diffusion, la migration et la convection, s'exprimé par:

$$N_i = -\nu_i \left[1 - \frac{dlnc_{sl}}{dlnc}\right] D\nabla c + \frac{it_i^0}{z_i F} + c_i v_{sl} \tag{2.1}$$

Où t_i^0 est le nombre de transport de l'espèce i et est généralement supposé constant. Il est défini comme la fraction du courant transporté par l'espèce i. La somme des nombres de transport de tous les ions existant en solution doit être égale à l'unité. Pour simplifier, il est courant de négliger le terme de convection (la vitesse de solvant (v_{sl}) est considérée comme nulle) et la variation de la concentration de solvant par rapport à la concentration d'électrolyte ($\frac{dlnc_{sl}}{dlnc}$). L'expression du flux est substituée dans un bilan de masse général pour l'espèce i:

$$\frac{\partial c_i}{\partial t} = -\nabla . N_i + R_i \tag{2.2}$$

Un bilan de masse sur le sel dans les pores de l'électrode est donné par:

$$\varepsilon \frac{\partial c}{\partial t} + \nabla . [c v_{sl}] = \nabla . \left[D_{eff} \left[1 - \frac{d(lnc_{sl})}{d(lnc)}\right] \nabla c\right] + [1 - t_i^0] \frac{a j_m}{\nu_+} - \frac{i_2 \nabla t_i^0}{z_+ \nu_+ F} \tag{2.3}$$

Comme il n'y a pas de réaction dans la zone de séparation, le terme de réaction, j_m , est négligé. On obtient donc un bilan sur le sel dans le séparateur:

$$\varepsilon \frac{\partial c}{\partial t} + \nabla . [c v_{sl}] = \nabla . \left[D_{eff} \left[1 - \frac{d(lnc_{sl})}{d(lnc)}\right] \nabla c\right] - \frac{i_2 \nabla t_i^0}{z_+ \nu_+ F} \tag{2.4}$$

Où $z_+ \nu_+$ est égal à unité pour l'ensemble des sels présents dans la batterie Li-ion ($LiClO_4$, $LiPF_6$) parce que les nombres de charge et les nombres d'ions positifs et négatifs sont égaux à unité.

Conditions aux frontières et conditions initiales: Il y a continuité pour la concentration et le flux molaire aux limites internes (interface de séparateur/électrode positive et interface de séparateur/électrode négative). Il n'y a pas de flux molaire aux frontières extérieures (limites de l'électrode positive/collecteur de courant et limites de l'électrode négative/collecteur de courant). Pour la condition initiale, la concentration à $t = 0$ est égale à la concentration initiale de Li ion en phase de solution.

$$c_2|_{t=0} = c_0 \tag{2.5}$$

La variation de potentiel dans la phase solution du séparateur ou de l'électrode poreuse est calculée à partir de

$$\nabla \Phi_2 = -\frac{i_2}{\kappa_{eff}} + \frac{2RT}{F} \left[1 + \frac{dlnf_{\pm}}{dlnc}\right] [1 - t_i^0] \nabla lnc \tag{2.6}$$

où $f_{\pm}$ est le coefficient d'activité molaire moyen du sel. Le deuxième terme du côté droit montre une surtension de concentration en phase solution. En raison du manque de données expérimentales, le terme de $\frac{dlnf_{\pm}}{dlnc}$ a été généralement négligé dans la plupart des articles.

Conditions aux limites et conditions initiales: Il y a continuité pour le potentiel et la densité de courant dans la phase solution aux frontières internes. La densité de courant dans la phase solution est nulle aux limites extérieures. Pour la condition initiale, le potentiel d'électrolyte à $t = 0$ dans les différents domaines formant la cellule, est supposé être égal au potentiel du circuit ouvert de l'électrode négative qui est une fonction de l'état de charge initial (SOC) du Li dans l'électrode négative.

$$\Phi_2|_{t=0} = -U_{neg}(c_{1,neg}^0/c_{1,max}) \tag{2.7}$$

La relation entre le flux à l'interface interne du pore, j_m, et le gradient de la densité de courant superficielle, i_2, dans la phase solution de l'électrode poreuse est donnée par

$$aj_m = -\frac{1}{F}\frac{\partial i_2}{\partial x} \tag{2.8}$$

La surface spécifique, a, est définie par le rapport de la surface au volume de l'électrode poreuse.

- Équations de transport en phase solide de l'électrode poreuse

Équation de diffusion: Un bilan de masse sur le lithium dans la direction r de la phase solide conduit à:

$$\frac{\partial c_1}{\partial t} = \frac{1}{r^n}\frac{\partial}{\partial r}\left(Dr^n\frac{\partial c_1}{\partial r}\right) \tag{2.9}$$

La valeur de n dépend de la géométrie des particules du matériau actif en phase solide.

Conditions aux limites:

$$\frac{\partial c_1}{\partial r} = 0 \qquad \text{at } r = 0 \tag{2.10}$$

$$j_m = -D\frac{\partial c_1}{\partial r} \qquad \text{at } r = R_s \tag{2.11}$$

Condition initiale:

$$c_1(r, 0) = c_1^0 \tag{2.12}$$

Où c_1^0 est la concentration initiale de Li dans la particule.

La loi d'Ohm: La conduction électrique pure est le phénomène qui régit le transport des charges dans les matériaux actifs. En fait, la contribution de la diffusion des ions par rapport au courant

électrique est négligée, car la mobilité des ions est beaucoup plus faible que celle des électrons. Ainsi, la conduction électrique n'est portée que par des électrons. Le potentiel dans la phase d'électrode est obtenu par la loi d'Ohm:

$$\nabla \Phi_1 = -\frac{i_1}{\sigma_{eff}} \tag{2.13}$$

Où σ_{eff} est une conductivité efficace dans l'électrode poreuse.

Conditions aux limites et conditions initiales: Tout le courant est lié au courant électrique transporté par les électrons à la limite de l'électrode positive / du collecteur de courant. Puisque seulement les différences de potentiel sont significatives, il est courant de définir $\Phi_1 = 0$ à la limite de l'électrode négative/du collecteur de courant. Le potentiel électrique à l'électrode négative à $t = 0$ est considéré comme nul et à l'électrode positive est défini par:

$$\Phi_1|_{t=0} = U_{pos}(c_{1,pos}^0/c_{1,max}) - U_{neg}(c_{1,neg}^0/c_{1,max}) \tag{2.14}$$

La densité de courant totale dans les deux phases est donnée par un bilan de charge:

$$I = i_1 + i_2 \tag{2.15}$$

Où I est la densité de courant totale. La densité de courant de la phase solide, i_1, peut être éliminée des équations gouvernantes mentionnées ci-dessus en appliquant cette expression.

La correction de Bruggeman est généralement utilisée pour convertir les propriétés de transport, κ, D et σ en leurs valeurs effectives en milieu poreux.

$$\kappa_{eff} = \frac{\varepsilon \kappa}{\tau} \tag{2.16}$$

$$D_{eff} = \frac{\varepsilon D}{\tau} \tag{2.17}$$

$$\sigma_{eff} = \frac{\varepsilon \sigma}{\tau} \tag{2.18}$$

Bruggeman a envisagé un processus d'intégration de deux phases différentes dans un échantillon et a pris en compte certaines hypothèses: L'échantillon est constitué de deux phases homogènes et isotropes, Chaque phase est constituée de particules de petite taille en comparant à la taille de l'échantillon et elle est distribuée au hasard dans l'échantillon. De plus, dans le modèle de Bruggeman, les obstacles à transporter étaient supposés être constitués de sphères ou de cylindres [30].

Basé sur ces hypothèses, le facteur de tortuosité, τ, est lié à la porosité par

$$\tau = \varepsilon^{-1/2} \tag{2.19}$$

ce qui conduit à la correction Bruggeman standard pour les propriétés de transport [31]:

$$\kappa_{eff} = \varepsilon^{1.5}\kappa \tag{2.20}$$

$$D_{eff} = \varepsilon^{1.5}D \tag{2.21}$$

$$\sigma_{eff} = \varepsilon^{1.5}\sigma \tag{2.22}$$

- Cinétique des électrodes

Une réaction de transfert de charge pour l'intercalation/dés-intercalation des ions Li à l'interface solide / solution est décrite par

$$\mathrm{Li}^{+} + \Theta_s + \mathrm{e}^{-} \rightleftarrows \mathrm{Li} - \Theta_s \tag{2.23}$$

Où Θ_s représente un site dans le réseau solide. Le taux de réaction ou la densité de courant locale pour le processus d'intercalation et de dés-intercalation est liée à la concentration et à la surtension à travers l'équation de Butler-Volmer.

$$i_m = i_0 \left(exp\left(\frac{\alpha_a F \eta_{sur}}{RT}\right) - exp - \left(\frac{\alpha_c F \eta_{sur}}{RT}\right)\right) \tag{2.24}$$

Où α_a et α_c sont les coefficients de transfert anodique et cathodique de la réaction de l'électrode, F est la constante de Faraday, R la constante universelle de gaz, et T la température absolue en Kelvin.

La densité de courant d'échange, i_0, est donnée par

$$i_0 = F\, k\, (c_{1,max} - c_1)^{\alpha_a} (c_1)^{\alpha_c} ({}^{c}/_{c_{ref}})^{\alpha_a} \tag{2.25}$$

Où k est la constante de taux, c , c_{ref}, $c_{1,max}$ et $(c_{1,max} - c_1)$ sont respectivement la concentration de l'électrolyte, la concentration de référence d'électrolyte, la concentration maximale de Li et la concentration de sites inoccupés dans la phase solide.

La surtension à la surface des particules est calculée par

$$\eta_{sur} = \Phi_1 - \Phi_2 - U(c_1, T) \tag{2.26}$$

Où Φ_1 est le potentiel de la phase solide, Φ_2 est le potentiel de la phase solution et $U(c_1, T)$ est le potentiel du circuit ouvert (OCP) en fonction de la quantité de Li insérée et de la température. La valeur et la dépendance de l'OCP à la concentration de Li insérée sont différentes pour différents matériaux d'insertion.

La relation entre le taux de réaction et le flux à l'interface interne du pore est donnée par

$$i_m = F j_m \tag{2.27}$$

2.3 Modèle thermique

La sécurité, la performance et la durée de vie des batteries Li-ion sont des défis affectés par les températures d'opération des batteries. Bien que la performance de la batterie soit améliorée à des températures d'opération élevées, une exposition prolongée réduira la durée de vie de la batterie. La gestion thermique des batteries est essentielle car la chaleur produite lors de la décharge peut provoquer des phénomènes dommageables tels que la perte de la capacité/de puissance et l'emballement thermique. Bandhauer et al. [32] ont analysé l'effet de la température sur la perte de la capacité/de puissance et l'emballement thermique et ils ont étudié la performance de la batterie à basses températures. Broussely et al. [33] ont indiqué que la dégradation de performance des batteries Li-ion peut être la conséquence d'une perte d'énergie (capacité) ou une perte de puissance. La perte d'énergie peut provenir de la transformation de matériaux actifs d'électrodes en substances inactives entraînant une réduction de la capacité de la batterie. La perte de puissance peut résulter de l'augmentation des résistances internes entraînant une diminution des voltages d'opération.

Ramadass et al. [34] ont montré que la perte de capacité de la cellule Li-ion augmentait en élevant la température. Leurs résultats ont indiqué qu'après 500 cycles, la perte de capacité a atteint 22.5% et 70.6% à des températures de 25 ° C et 55 ° C, respectivement. La perte de capacité trouve son origine dans la formation d'une couche de film à la surface de l'électrode négative. Bloom et al. [10] ont développé un modèle empirique de la perte de capacité pour estimer la durée de vie de la cellule Li-ion. Selon leurs résultats, la durée de vie de la batterie Li-ion était significativement influencée par la température. En fait, l'augmentation de la température a accéléré la perte de puissance des cellules. L'emballement thermique dans les batteries est le résultat de l'élévation de la température entraînant des réactions exothermiques génératrices de chaleur menant à une augmentation de la température, ce qui déclenche des réactions plus destructrices. Spotnitza and Franklin [35] ont indiqué que les réactions exothermiques possibles survenant dans les batteries Li-ion peuvent résulter de la décomposition de la couche d'interface électrolyte/ solide (SEI) à 90-120°C, de la décomposition de l'électrolyte à des températures élevées>200°C, de la décomposition du matériau actif de l'électrode positive et de la réaction du Li intercalé avec l'électrolyte à des températures élevées>120°C. En outre, l'augmentation de la température peut résulter de la libération de chaleur par des processus entropiques, des surtensions et des résistances ohmiques.

La performance de la batterie diminue à basse température, en particulier en dessous -20°C. Zhang et al. [36] ont attribué cette mauvaise performance des batteries Li-ion à la limitation du transfert de charge à l'interface électrode/électrolyte conduisant à un placage significatif (dépôt Li-ion sous forme de lithium métallique) sur l'électrode négative pendant la charge. Pour des raisons de sécurité, les limites de température de charge et de décharge autorisées pour la plupart des appareils équipés de batteries Li-ion sont 0–45 °C and -20–60°C, respectivement. La meilleure température d'opération des batteries Li-ion se situe entre 25 et 40 °C pour laquelle il existe un bon équilibre entre performance et durée de vie [37].

Comme, la performance de la batterie Li-ion est fortement influencée par la température, il est important de comprendre les mécanismes de génération et de transfert de chaleur. Les principales sources de génération/consommation de chaleur comprennent la chaleur entropique, la chaleur de réaction irréversible, la chaleur ohmique et la chaleur de diffusion (la chaleur de relaxation). En

fait, la chaleur totale produite est composée de la chaleur provoquée par la polarisation totale à l'intérieur de la batterie, en plus de la chaleur entropique. Les trois principales sources de polarisation à l'intérieur de la batterie sont les suivantes:

- L'activation (cinétique interfaciale)
- Le transport de masse d'espèces en raison des gradients de concentration dans les phases solide et solution
- La chute de potentiel ohmique en raison d'une conductivité ionique insuffisante en phase solution et d'une conductivité électronique insuffisante en phase solide

Une discussion approfondie sur les sources de génération / consommation de chaleur et la portion de chaque polarisation dans la génération de la chaleur totale ainsi que les équations régissant les modèles thermiques des batteries Li-ion sont étudiées au chapitre 6.

2.4 Modélisation numérique

Le logiciel commercial COMSOL MULTIPHYSICS est utilisé pour simuler le comportement des batteries Li-ion. Ce logiciel a ses propres avantages et désavantages. C'est un logiciel convivial qui résout des équations aux dérivées partielles par la méthode des éléments finis. De plus, COMSOL ne permet pas facilement aux utilisateurs de modifier la structure de l'implantation informatique des algorithmes numériques pour augmenter l'efficacité du calcul.

Il existe de nombreux modules dans COMSOL dont l'un est lié à l'interface batterie Li-ion. Ce module est utilisé pour calculer les distributions de potentiel et de courant. Les matériaux des électrodes et de l'électrolyte sont choisis dans la bibliothèque de matériaux existant dans COMSOL. Le modèle de Newman [28] est la base des équations de l'interface de la batterie Li-ion. L'interface physique comprend les équations de transport de masse et de charge pour les électrodes, les électrolytes et les séparateurs, les expressions cinétiques et les conditions aux frontières applicables pour décrire les caractéristiques de charge et de décharge de la batterie.

L'un des problèmes de l'interface batterie Li-ion est de négliger la distribution granulométrique (la distribution de tailles de particules) des électrodes. En fait, dans le domaine de l'électrode poreuse lié à l'interface de la batterie Li-Ion, une seule taille de particule peut être sélectionnée. Ainsi, il n'est utile que pour une distribution granulométrique uniforme ou monomodale. Pour résoudre ce problème pour des modèles de distribution de taille bimodale ou de 3-particules, la boîte à outils de modélisation basée sur les équations est utilisée. L'interface COMSOL PDE (Partial Differential Equation) de la branche Mathématiques est impliquée dans la modélisation basée sur les équations exécutées par les utilisateurs.

Le modèle électrochimique-thermique est développé en ajoutant l'interface de transfert de chaleur dans les solides à une interface de batterie Li-ion. L'interface de transfert de chaleur dans les solides est utilisée pour modéliser le transfert de chaleur par conduction, convection et radiation. De plus, des contributions supplémentaires telles que des sources de chaleur sont impliqués dans cette interface.

CHAPITRE 3

Une étude sur l'effet de la porosité et de la distribution de la taille des particules sur la performance de batterie Li-ion

Titre original: A Study on the Effect of Porosity and Particles Size Distribution on Li-ion Battery Performance

Auteurs et affiliation:

- **Sara Taslimi Taleghani:** étudiante au doctorat, Université de Sherbrooke, Faculté de génie, Département de génie chimique et de génie biotechnologique.
- **Bernard Marcos:** professeur, Université de Sherbrooke, Faculté de génie, Département de génie chimique et de génie biotechnologique.
- **Karim Zaghib:** Institut de recherche d'Hydro-Québec (IREQ), Varennes, QC, Canada, J3X 1S1.
- **Gaétan Lantagne:** Institut de recherche d'Hydro-Québec (IREQ), Varennes, QC, J3X 1S1.

Date d'acceptation: 19 mai 2017

État de l'acceptation: publié

Référence: Journal of the Electrochemical Society, DOI: 10.1149/2.0211711jes

Résumé

Contenu : Cet article présente un modèle pseudo-bidimensionnel (P2D) qui décrit l'effet des propriétés structurelles de l'électrode positive sur la performance des cellules Li-ion pendant la décharge. La validation du modèle monomodal a été faite en utilisant les données expérimentales et les résultats de Doyle [7]. L'énergie spécifique maximale a été obtenue dans la porosité de 0.55, tandis que la puissance spécifique y avait encore une valeur élevée. De plus, si on s'éloigne de la valeur optimale de la porosité, on observe un changement brusque du voltage et une capacité inférieure. En outre, différents modèles de distribution de la taille des particules, dont les modèles monomodal, bimodal et 3-particules, ont été comparés les uns aux autres. La distribution monomodale est apparue correspondre à la distribution optimale avec la plus faible polarisation totale. Les distributions bimodal et 3-particules ont approché cet état idéal lorsque la fraction volumique des plus petites particules augmente. Cette disposition structurelle a conduit à des profils de distribution de densité de courant locaux plus uniformes entraînant une plus grande diminution de la polarisation des cellules. Différentes densités de courant de décharge ont été appliquées à différents modèles de distribution granulométrique, et les résultats ont montré que la distribution granulométrique a un effet plus important à des densités de courant de décharge plus élevées.

Résultats : Les résultats présentés ont indiqué que les propriétés structurelles peuvent affecter de manière significative le voltage de la cellule, la capacité de la cellule, la polarisation de la cellule, l'énergie spécifique de la cellule et la puissance spécifique.

Contribution à la thèse : Contrairement à la plupart des études antérieures axées sur la distribution granulométrique uniforme de l'électrode, l'article incluait des distributions granulométriques non uniformes. En effet, l'effet des propriétés structurelles telles que la porosité et la distribution granulométrique a été étudié sur la performance de la cellule Li_xC_6-$Li_yMn_2O_4$ pendant la décharge en utilisant un modèle P2D. Différentes distributions de la taille de particules pour l'électrode positive, dont les distributions de taille monomodale, bimodale et 3-particules, ont été prises en compte. Cette étude peut être utilisée pour d'autres technologies de batteries en cours de développement, comme les batteries à haute énergie (le lithium-air et le lithium-soufre).

Abstract

A pseudo two-dimensional model (P2D) is presented that describes the effect of the structural properties of the positive electrode on Li-ion cell performance during discharge. The validation of the mono-modal model was done by using Doyle's experiment and results [7]. A large increase or decrease in the porosity beyond a specific value led to a sharp change in the cell voltage curve and lower cell capacities. The maximum specific energy was obtained in the porosity range of 0.55, while the specific power still had a high value. Furthermore, different particle size distribution models, including mono-modal, bi-modal and 3-particle models, were compared to each other. The mono-modal model was the ideal state with the lowest total polarization. The bi-modal and 3-particle models approached this ideal state when the volume fraction of the smallest particles in their structures increased. This structural arrangement in these models led to more uniform local current density distribution profiles resulting in a greater decrease in cell polarization. Different discharge current densities were applied to different particle size distribution models, and the results showed that the particle size distribution has a greater effect at higher discharge current densities.

List of Symbols

a	Specific surface area, $\mathrm{m^2/m^3}$
c	Concentration of Li, $\mathrm{mol/m^3}$
c_1^0	Initial concentration of lithium in the solid phase, $\mathrm{mol/m^3}$
$c_{1,max}$	Maximum concentration of lithium in the solid phase, $\mathrm{mol/m^3}$
D	Diffusion coefficient, $\mathrm{m^2/s}$
F	Faraday's constant, 96487, $\mathrm{C/mol}$
i_0	Exchange current density, $\mathrm{A/m^2}$
i_m	Local current density in the porous matrix, $\mathrm{A/m^2}$
I_{app}	Applied current density of cell, $\mathrm{A/m^2}$
j_m	Pore wall flux of lithium-ions, $\mathrm{mol/m^2}$ s
k	Reaction rate constant
l	Thickness, m
M	Mass per surface area of cell, $\mathrm{kg/m^2}$
r	Radial coordinate, m
R	Universal gas constant, 8.314 $\mathrm{J/mol\ K}$
t	Time, s
t_+^0	Transference number of species Li^+
T	Absolute temperature, K
U	Open-circuit potential, V
x	Spatial coordinate, m

Greek

α_a, α_c	Anodic and cathodic transfer coefficients
ε	Volume fraction or porosity of a phase
η	Overpotential, V
κ	Ionic conductivity of electrolyte, S/m
σ	Electronic conductivity of the solid phase, S/m
Φ	Electrical potential, V

Subscripts

eff	Effective value of transport property in porous medium
n	Negative electrode
p	Positive electrode
s	Separator
1	Solid phase
2	Solution phase

3.1 Introduction

Li-ion batteries play a significant role in the automotive industry, large-scale utility storage and other advanced technologies due to their beneficial features such as higher energy and power densities along with cycle durability. In addition, the lower environmental impact and improved safety of these new products have clearly demonstrated their advantages as alternatives to fossil fuels [38], [39].

Since understanding structural properties of batteries is of considerable significance to battery designers in order to improve battery systems, many models have appeared in the literature over the years [40], [41].

A reaction-zone model based on fast electrode kinetics and neglecting the concentration gradients was first introduced by Newman [42] to optimize the electrode thickness and porosity. Ramadesigan et al. [18] used a single-electrode model to find the optimal porosity by neglecting the solid-phase intercalation mechanism and considering only the ohmic limitation. The optimization of design parameters, including the thickness and porosity of both electrodes, was done by De et al. [43] to maximize the specific energy delivered from the battery: they used a valid reformulated model to facilitate multi-parameter optimization in which the micro structural effects were neglected. Dai and Srinivasan [44] described a model based on graded electrode porosity to expand the energy density of the battery.

Until recently, most Li-ion battery models used a mono-modal particle size distribution for an intercalation electrode, while it is obvious that a real electrode consists of particles with different sizes. Few studies have addressed the effect of particle size on the intercalation electrode performance. Von Sacken et al. [45] used an accelerating rate calorimeter to investigate the

effect of the specific surface area of the coke used for the negative electrode (LixC6) on the thermal stability. They showed that particle size of the active materials can be beneficial with respect to thermal stability at high temperatures. Tran et al. [46] conducted some experiments to study the influence of particle size and discharge rate on the capacity of a lithium-ion graphite electrode. The results showed that the capacity obtained from small graphite particles (6 μm) at a C/2 discharge rate was 80% of that at a C/24 rate (near steady-state conditions). By contrast, the capacity of larger graphite particles (44 μm) at a discharge rate of C/2 was estimated at 25% of the capacity obtained at a C/24 rate. Darling and Newman [47] investigated the effect of a bi-modal particle size distribution on galvanostatic cycling using a mathematical model. They indicated that the uniform (mono-modal) particle size distribution should have the lowest conformity to experimental data at a high discharge rate compared to a non-uniform particle size distribution. Meyer et al. [48] explained the effect of particle size distribution on the negative electrode and the dependence of local state of charge (SOC) distribution on the distance from the separator. Their results indicated that particles of smaller size, due to their efficient specific surface area, were oxidized faster during the discharge process.

It would appear that a non-uniform particle size distribution in the electrodes is a significant factor to achieve more representative results. Since there are relatively few papers dealing with this important subject in the open literature, it is important to expand the level of knowledge on the effect of different particle size distributions, such as mono-modal, bi-modal and 3-particle size distributions, on the performance of lithium-ion batteries. It should also be stressed that this study is relevant to other battery technologies currently under development, namely high-energy batteries like lithium-air and lithium sulfur [49], [50].

The presented study follows Doyle's model [7] during the discharge process of a dual Li intercalation cell. The mono-model was extended to the bi-modal and 3-particle size models to study the effect of particle size distributions on cell performance. Firstly, this paper evaluated the effect of different porosities on the specific energy and the specific power of the Li-ion cell. Secondly, the importance of the particle size distributions of the positive electrode on the performance of the cell was studied in detail. Then, the influence of discharge current densities or C-rates on the cell voltage, cell capacity and specific power for different particle size distributions is presented.

3.2 Model Development

Modeling a full cell involves the use of complicated coupled partial differential equations (PDEs). The P2D model is a sophisticated model in which mass and charge transport in the electrolyte and solid phases, as well as the reaction kinetics in the electrolyte-solid interface, are considered. Although this model is more accurate when compared to other models, it is computationally more demanding. Doyle et al. [19] developed a P2D model based on the principles of transport phenomena, electrochemistry and thermodynamics. The concentration and potential in the electrolyte, separator and solid phase were found by solving coupled nonlinear PDEs. Doyle's model [19] was extensively used by other researchers to improve battery systems [13], [21], [22], [24], [51], [52].

The present work is an extension of Doyle's model [7] to bi-modal and 3-particle size distribution models. In accordance with his model, the dual lithium-ion intercalation cell consisted of a negative current collector (Cu), negative porous electrode (Li_xC_6), separator, positive porous electrode ($Li_yMn_2O_4$) and positive current collector (Al) [7]. The plasticized electrolyte was composed of $LiPF_6$ salt in a liquid mixture of ethylene carbonate and dimethyl carbonate, as well as a copolymer from vinylidene fluoride and hexafluoropropylene. Figure 3.1 illustrates a P2D model. All the physical and structural parameters were extracted from Doyle's model [7]. A list of these parameters is presented in Table 3.1.

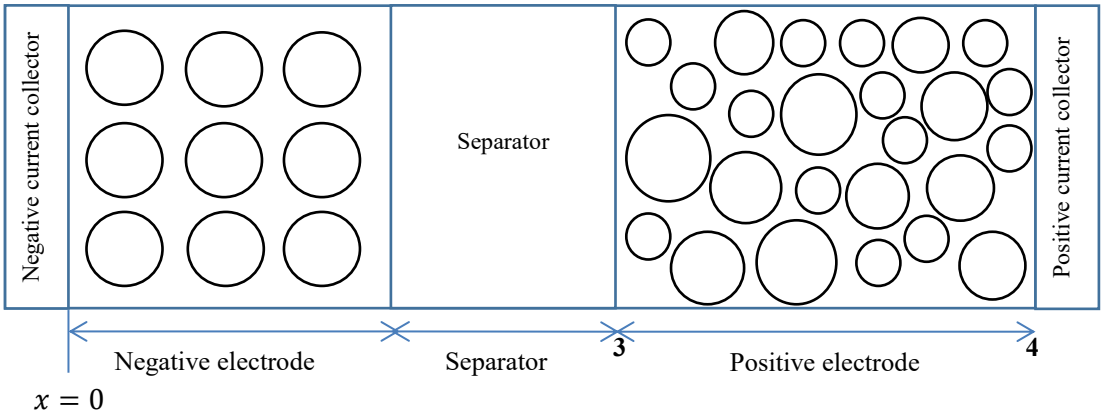

Figure 3.1: A representation of a P2D model

Table 3.1: List of model parameters [7]

Parameter	Symbol	Li_xC_6	Separator	$Li_yMn_2O_4$
Diffusion coefficient (m^2/s)	D	3.9×10^{-14}	9×10^{-11}	1×10^{-13}
Electronic conductivity (S/m)	σ	100		3.8
Initial concentration of lithium in the solid phase (mol/m^3)	c_1^0	14870		3900
Maximum concentration of lithium in the solid phase (mol/m^3)	$c_{1,max}$	26390		22860
Anodic and cathodic transfer coefficients	α	0.5		0.5
Thickness (m)	l	1×10^{-4}	52×10^{-6}	174×10^{-6}
Electrode porosity	ε	0.357		0.444
Transference number of species Li^+	t_i^0		0.363	

All equations were solved in the x direction except for the Li diffusion equation in solid phase that followed Fick's law in the r-direction which defined our approach as a P2D model. These equations were coupled due to the intercalation/de-intercalation reaction of the Li-ions at the solid/solution interface. The local current density or reaction rate was obtained by the well-known Butler-Volmer equation

$$i_m = i_0 \left(exp\left(\frac{\alpha_a F \eta_{sur}}{RT}\right) - exp\left(-\frac{\alpha_c F \eta_{sur}}{RT}\right)\right) \tag{3.1}$$

where the exchange current density, i_0, is given by

$$i_0 = F\ k\ (c_{1,max} - c_1)^{\alpha_a} (c_1)^{\alpha_c} (c_2)^{\alpha_a} \tag{3.2}$$

and where k, c_2 , $c_{1,max}$ and $(c_{1,max} - c_1)$ are the quasi-equilibrium rate constant; concentration of lithium ions in the electrolyte; maximum concentration of lithium and concentration of the unoccupied sites in the solid phase-negative or positive electrode- respectively.

The surface overpotential was calculated at constant temperature by

$$\eta_{sur} = \Phi_1 - \Phi_2 - U(c_1) \tag{3.3}$$

where Φ_1 is the potential in the solid or matrix phase while Φ_2 refers to the solution potential. $U(c_1)$ refers to the open circuit potential of the electrode under consideration evaluated at the concentration $c_1$and constant temperature.

The relation between the reaction rate and the pore wall flux is given by

$$i_m = F j_m \tag{3.4}$$

A summary of the governing equations of the model and the corresponding boundary conditions are presented in Table 3.2 and Table 3.3.

Table 3.2: Governing equations and boundary conditions for positive and negative electrodes in a pseudo-two-dimensional model (x and r)

Governing equations	Boundary conditions	
	Positive electrode	Negative electrode
Mass balance in the electrolyte for a binary salt concentrated electrolyte $\varepsilon_m \frac{\partial c_2}{\partial t} = D_{eff,m} \frac{\partial^2 c_2}{\partial x^2} + a_m(1 - t_+^0) j_m$ Initial condition $c_2\|_{t=0} = c_0$ $m = p \; or \; n$ **Hypotheses** Solvent velocity equals to zero Constant transport properties integrating non-ideality effect Constant porosity Structural properties-porosity and tortuosity-integrated in $D_{eff,m}$	$-D_{eff,p} \left.\frac{\partial c_2}{\partial x}\right\|_{x=l_n+l_s+l_p} = 0$ $c_2\|_{x=l_n+l_s,-} = c_2\|_{x=l_n+l_s,+}$	$-D_{eff,n} \left.\frac{\partial c_2}{\partial x}\right\|_{x=0} = 0$ $-D_{eff,n} \left.\frac{\partial c_2}{\partial x}\right\|_{x=l_n,-} = -D_s \left.\frac{\partial c_2}{\partial x}\right\|_{x=l_n,+}$
Potential distribution in solution $\nabla(-\kappa_{eff,m} \frac{\partial \varphi_2}{\partial x} + \frac{2\kappa_{eff,m} RT}{F}(1 - t_+^0) \frac{\partial \ln c_2}{\partial x}) = a_m F j_m$ **Hypotheses** Structural properties-porosity and tortuosity-integrated in $\kappa_{eff,m}$	$i_2\|_{x=l_n+l_s+l_p} = 0$ $\varphi_2\|_{x=l_n+l_s,-} = \varphi_2\|_{x=l_n+l_s,+}$	$i_2\|_{x=0} = 0$ $i_2\|_{x=l_n,-} = i_2\|_{x=l_n,+}$
Potentiel distribution in matrix/solid phase $\sigma_{eff,m} \frac{\partial^2 \varphi_1}{\partial x^2} = a_m F j_m$ **Hypotheses** Structural properties-porosity and tortuosity-integrated in $\sigma_{eff,m}$	$i_1\|_{x=l_n+l_s} = 0$ $\left.\frac{\partial \varphi_1}{\partial x}\right\|_{x=l_n+l_s+l_p} = -\frac{I_{app}}{\sigma_{eff,p}}$	$\varphi_1\|_{x=0} = 0$ $i_1\|_{x=l_n} = 0$
Mass balance-solid-state diffusion only- in the matrix/solid phase in spherical coordinates $\frac{\partial c_1}{\partial t} = \frac{1}{r^2} \frac{\partial}{\partial r}\left(D_m r^2 \frac{\partial c_1}{\partial r}\right)$ Initial condition $c_1\|_{t=0} = c_1^0$	$\left.\frac{\partial c_1}{\partial r}\right\|_{r=0} = 0 \quad and \quad -D_m \left.\frac{\partial c_1}{\partial r}\right\|_{r=R_m} = j_m$	

Table 3.3: Governing equations and boundary conditions for separator

Governing equations	Boundary conditions
Mass balance in the separator	$c_2\|_{x=l_{n,-}} = c_2\|_{x=l_{n,+}}$
$\frac{\partial c_2}{\partial t} = D_s \frac{\partial^2 c_2}{\partial x^2}$	$-D_s \frac{\partial c_2}{\partial x}\Big\|_{x=l_n+l_s,-} = -D_{eff,p} \frac{\partial c_2}{\partial x}\Big\|_{x=l_n+l_s,+}$
Initial condition $c_2\|_{t=0} = c_0$	
Hypotheses	
Constant transport properties No reaction in the separator	
Potential distribution in the separator	$\varphi_2\|_{x=l_{n,-}} = \varphi_2\|_{x=l_{n,+}}$
$\nabla(-\kappa_s \frac{\partial \varphi_2}{\partial x} + \frac{2\kappa_s RT}{F}(1-t_+^0)\frac{\partial \ln c_2}{\partial x}) = 0$	$i_2\|_{x=l_n+l_s,-} = i_2\|_{x=l_n+l_s,+}$

3.2.1 Numerical Solution

In this paper, COMSOL Multiphysics 5.2 software was used to solve the equations. A time-dependent solver was used to study the cell discharge behavior. The direct solver of MUMPS (MUltifrontal Massively Parallel sparse direct Solver) was applied to solve the equations. The relative and absolute tolerances were equal to 0.001. The geometry was discretized automatically using a physics-controlled mesh. The maximum solution time was about 10 minutes. The simulated model results are discussed in the next section.

3.3 Results and Discussion

First, the cell voltage-capacity data of a mono-modal model simulated by COMSOL Multiphysics 5.2 was validated with the experimental and simulated data of Doyle [7]. The current density was 17.5 A/m^2. Figure 3.2 shows that the model simulated by COMSOL Multiphysics is in a good agreement with the experiment and the model of Doyle [7].

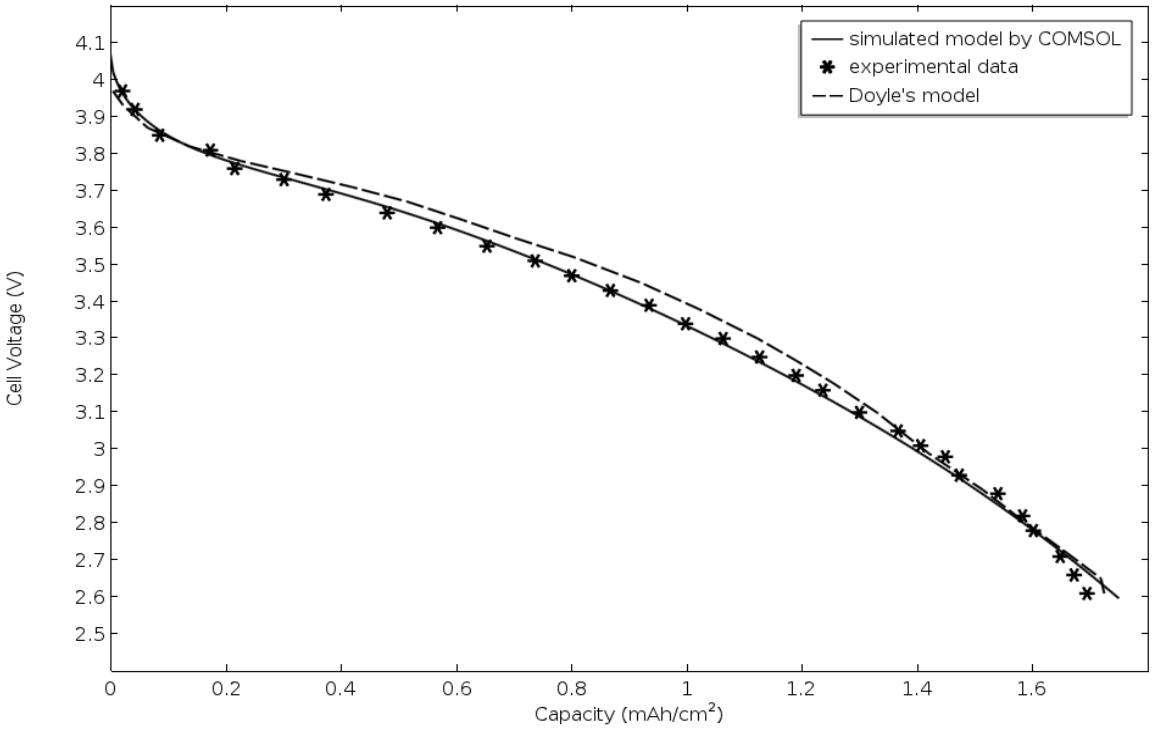

Figure 3.2: Model validation with experimental and simulated data of Doyle [7]

3.3.1 The effect of porosity on cell performance

Figure 3.3 shows the cell voltage curve in terms of cell capacity. The porosity in the positive electrode was considered as a variable while other structural parameters including the thickness of electrodes, separator thickness and negative electrode porosity were kept constant. The end of discharge cell voltage of 3.6 V was chosen for this simulation. With a porosity of 0.65, despite the increased amount of electrolytic solution in the pores of the electrode, a sharp decrease in cell voltage was observed due to the lower amount of active materials, which caused a kinetics limitation in the porous electrode. With a porosity of 0.2, the cell voltage decreased very quickly and the final capacity reached its lowest value. In this situation, despite the fact that the amount of active materials increased, there were not enough Li ions in the solution to reach the reaction zone leading to a mass transfer limitation.

Therefore, it was of significant importance to determine the optimal porosity. To achieve this goal, the cell specific energy was plotted in terms of the specific power of the cell for different porosities in Figure 3.4. The calculations were done with the constant limit of discharge cell voltage of 3.6 V.

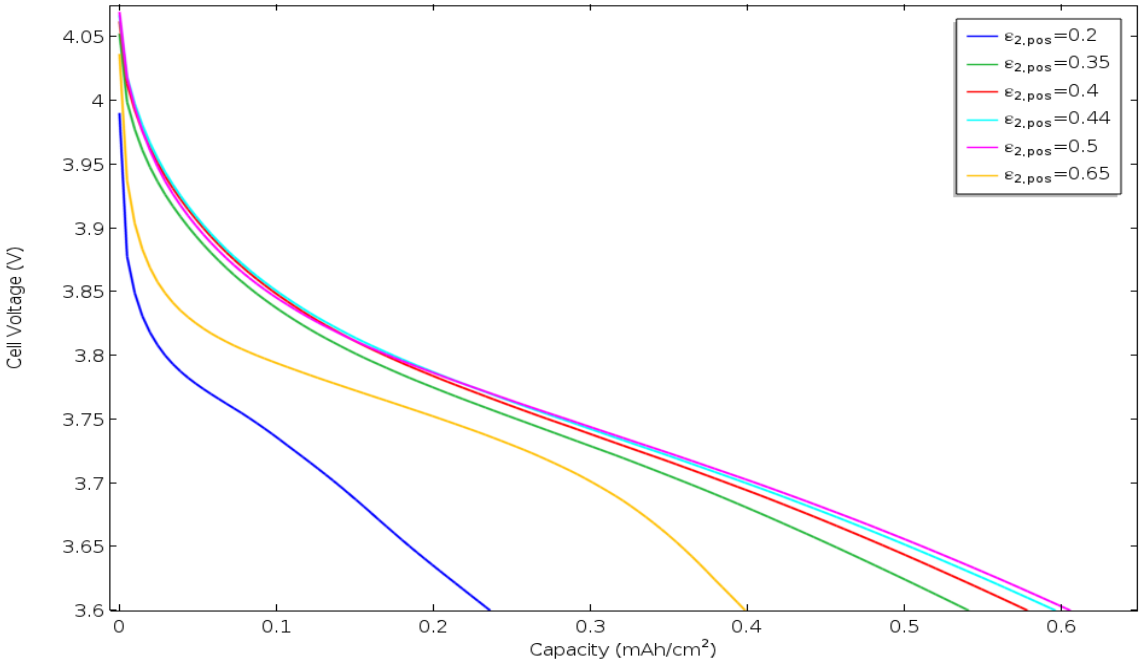

Figure 3.3: Cell voltage as a function of capacity during discharge process for different porosities

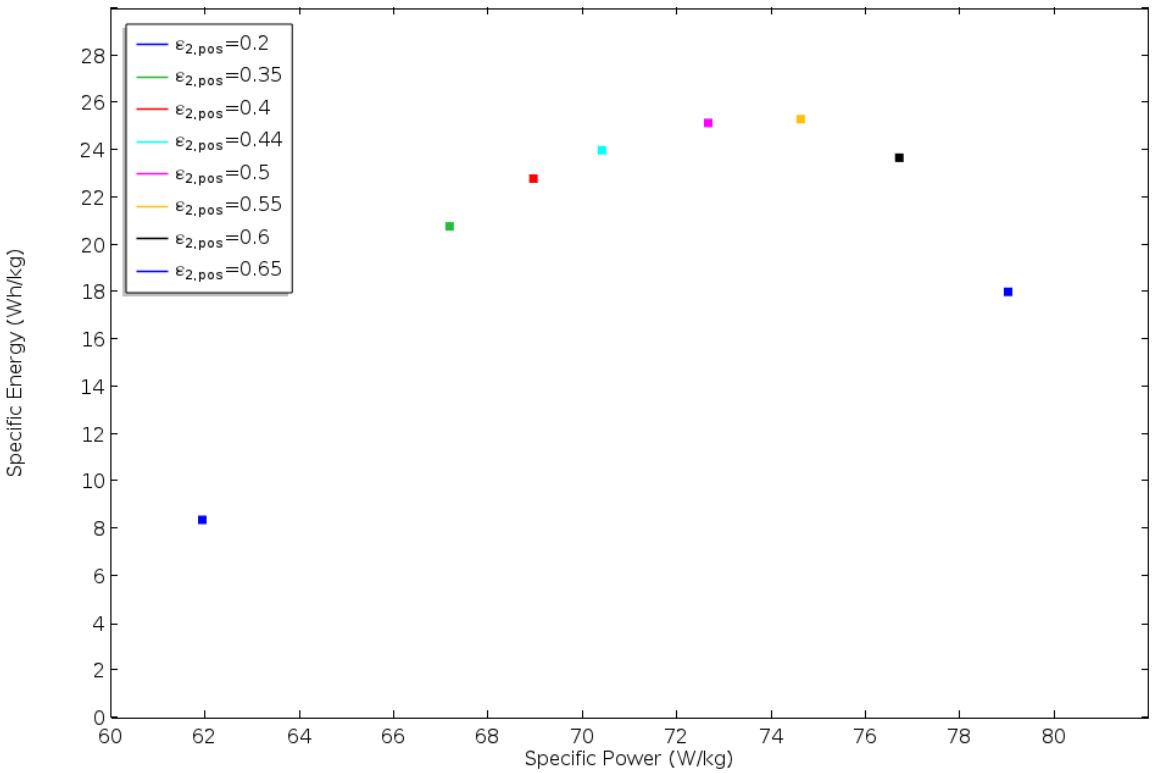

Figure 3.4: Specific energy versus specific power

The specific energy and the average specific power of the cell were calculated by [7]

$$Specific\ Energy = \frac{1}{M}\int_0^{t_f}(I_{app} * E_{cell})dt \tag{3.5}$$

$$Average\ specific\ Power = \frac{Specific\ Energy}{t_f} \tag{3.6}$$

where M and I_{app} are the mass per surface area and the current density applied on the positive current collector, respectively, and t_f is the total discharge time.

According to Figure 3.4, there was an increasing trend in the specific energy by increasing the porosity. Then the specific energy reached its maximum value at a porosity of around 0.55, which was followed by a decreasing trend. Therefore, a porosity equal to 0.55 appeared to be the optimal value for a such cell in which both specific energy and specific power have large values.

3.3.2 The effect of different particle size distributions on cell performance

Three different particle size distribution models were selected to study their effect on the cell voltage. In the bi-modal and 3-particle models, the positive electrode consisted of two particles and three particles with different radii, respectively, while the negative electrode was mono-modal. Active material particles were considered as spheres. Furthermore, the volume fraction of the particles was adjusted such that the radius of the mono-modal particle size distribution was the normal average of radii of particles existing in bi-modal or 3-particle size distributions. To create the bi-modal and 3-particle size distribution models, two assumptions were considered according to Darling's work [47]

1. The mass of active materials in the bi-modal and 3-particle models was the same as that in a mono-modal model.

2. The specific surface area of the active materials of both bi-modal and 3-particle models was equal to that of the mono-modal model.

The particle radii for the bi-modal and 3-particle models were selected by considering the different ranges of the particle size in their distributions. In addition, the particles with different sizes are considered to be present at all locations in the positive electrode. According to the above assumptions, the volume fraction of the two particles in a bi-modal model was calculated by [47]

$$\frac{\varepsilon_{1,b}}{\varepsilon_m} = \frac{\frac{r_{2,b}}{r_m} - 1}{\frac{r_{2,b}}{r_{1,b}} - 1} \tag{3.7}$$

$$\frac{\varepsilon_{1,b}}{\varepsilon_m} + \frac{\varepsilon_{2,b}}{\varepsilon_m} = 1 \tag{3.8}$$

with $r_{1,b} < r_m < r_{2,b}$

$r_{1,b}$ and $\varepsilon_{1,b}$ are the radius and the volume fraction of the smaller particles in a bi-modal particle size distribution, respectively. $r_{2,b}$ is the radius of the larger particles in a bi-modal particle size distribution. r_m and ε_m are the radius and the volume fraction of the active material particles in a mono-modal particle size distribution, respectively.

Furthermore, the volume fraction of each particle in a 3-particle model was computed by

$$\frac{\varepsilon_1}{\varepsilon_m} = \frac{\left(\left(\frac{r_3}{r_m}\right) - 1\right) - \frac{\varepsilon_2}{\varepsilon_m}\left(\left(\frac{r_3}{r_2}\right) - 1\right)}{\left(\left(\frac{r_3}{r_1}\right) - 1\right)} \tag{3.9}$$

$$\frac{\varepsilon_2}{\varepsilon_m} = \frac{\left(\left(\frac{r_1}{r_m}\right) - 1\right) - \frac{\varepsilon_3}{\varepsilon_m}\left(\left(\frac{r_1}{r_3}\right) - 1\right)}{\left(\left(\frac{r_1}{r_2}\right) - 1\right)} \tag{3.10}$$

$$\frac{\varepsilon_1}{\varepsilon_m} + \frac{\varepsilon_2}{\varepsilon_m} + \frac{\varepsilon_3}{\varepsilon_m} = 1 \tag{3.11}$$

By inserting the values of the radii for a specifically selected 3-particle system- $r_1 = 4$ µm , $r_2 = 15$ µm and $r_3 = 7$ µm- in the above equations (Eqs. (3.9) and (3.10)), a restricted range of volume fraction was determined such that:

$$0 < \frac{\varepsilon_1}{\varepsilon_m} < 0.2655$$

$$\frac{\varepsilon_2}{\varepsilon_m} > 0.361$$

$$0 < \frac{\varepsilon_3}{\varepsilon_m} < 0.6388$$

Table 3.4 illustrates the ratio of volume fraction of particles in different particle size distribution models to that in mono-modal model.

Table 3.4: Different particle size distributions

Particle size distribution	Radius (μm)	Volume fraction ratio $(\frac{\varepsilon}{\varepsilon_m})$
Mono-modal		
	8.67	1
Bi-modal		
Case 1	8.5	0.49
	8.84	0.51
Case 2	2.34	0.135
	15	0.865
3-particle model		
Case 1	4	0.265
	15	0.734
	7	0.001
Case 2	4	0.15
	15	0.57
	7	0.28
Case 3	4	0.1
	15	0.5
	7	0.4

Figure 3.5 shows a comparison of the cell voltage for the mono-modal, bi-modal and 3-particle size distribution models. An ascending trend in cell voltage and capacity was observed by increasing the volume fraction of the smallest particle in both bi-modal and 3-particle size distributions. This difference in cell voltage among model curves resulted from the different distribution of the particles size in the positive electrode structure. According to case 1 of the 3-particle model, the volume fraction of the smallest particle was assumed to have its highest limit ($\varepsilon_1 = 0.265\varepsilon_m$). In this case, the cell voltage reached its maximum value which was less than the cell voltage of the bi-modal model (case 1) and that of the mono-modal structure (as an ideal state). Additionally, the total cell polarization during discharge was higher for case 1 of the 3-particle model compared to that of the bi-modal (case 1) and mono-modal models (Figure 3.6).

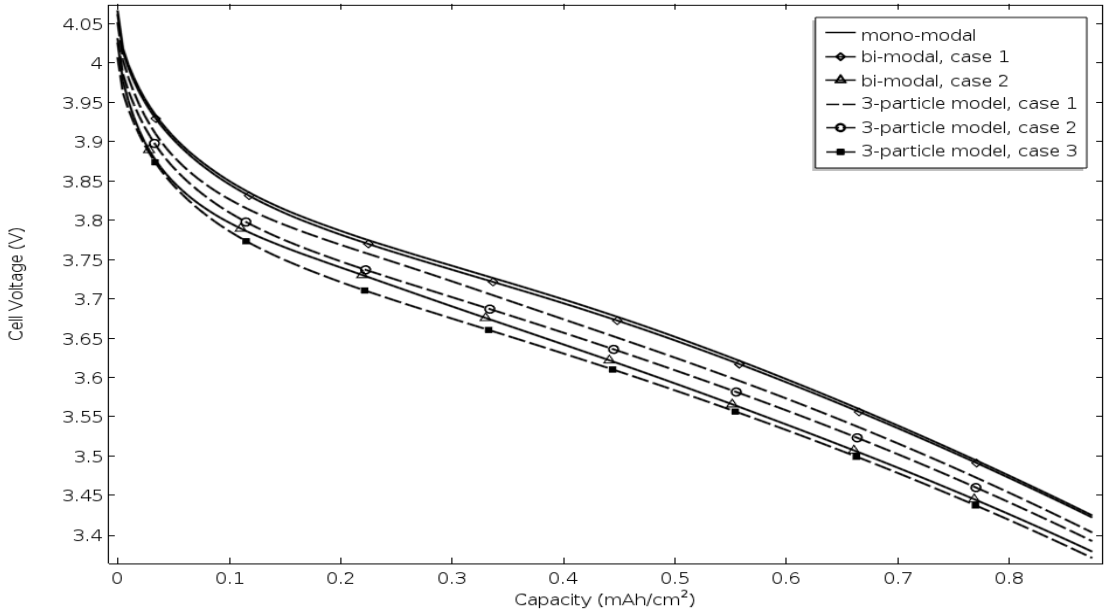

Figure 3.5: Cell voltage variation with capacity for different particle size distributions

The total polarization of the cell was calculated by the following equation

$$total\ polarization = E_{OCV,cell} - E_{cell} \tag{3.12}$$

where $E_{OCV,cell}$ is the open circuit cell voltage.

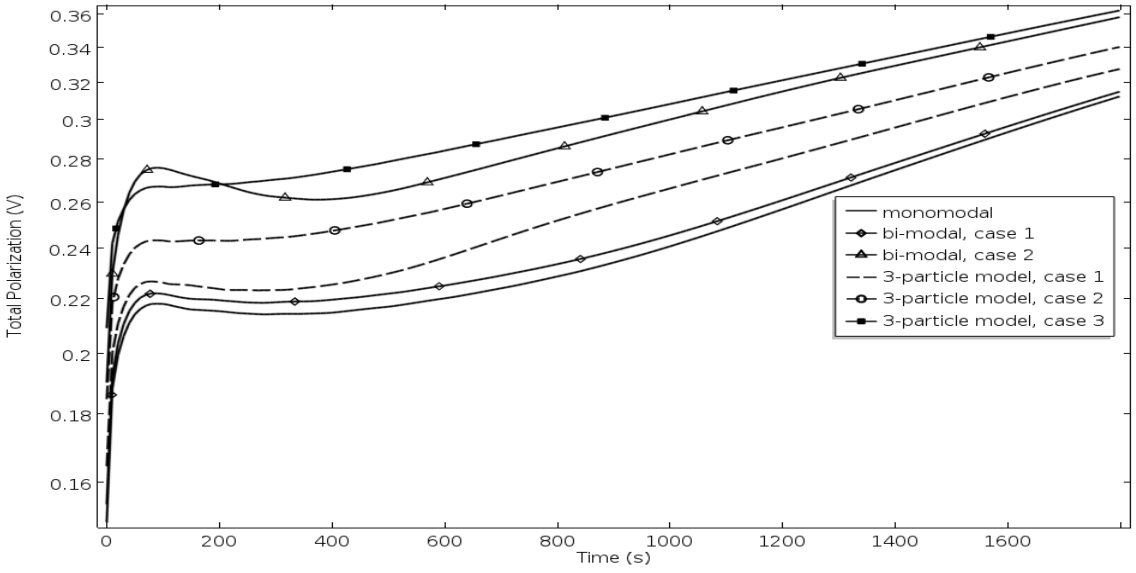

Figure 3.6: The total cell polarization during discharge time for different particle size distributions

The total cell polarization increased by decreasing the volume fraction of the smallest particle in both the bi-modal and 3-particle models, as shown in Figure 3.6. However, since the initial salt concentration was high enough ($2\frac{\text{mol}}{\text{l}}$), the concentration polarization caused by diffusion in the solution phase was not of significant importance. By contrast, the ohmic potential drop was the most important contribution to the total polarization for all three models as revealed in Figure 3.7. The electrolyte potential along the thickness of the cell for different particle size distribution models is presented in Figure 3.7. Despite the fact that the ohmic potential drop was a transport limiting mechanism in all models, the difference in cell total polarization among the different models resulted from the difference in concentration of the different particles in the particle size distribution models. The diffusion polarization in smaller particles is lower compared to that in larger particles because of the lower time constant for diffusion in smaller particles.

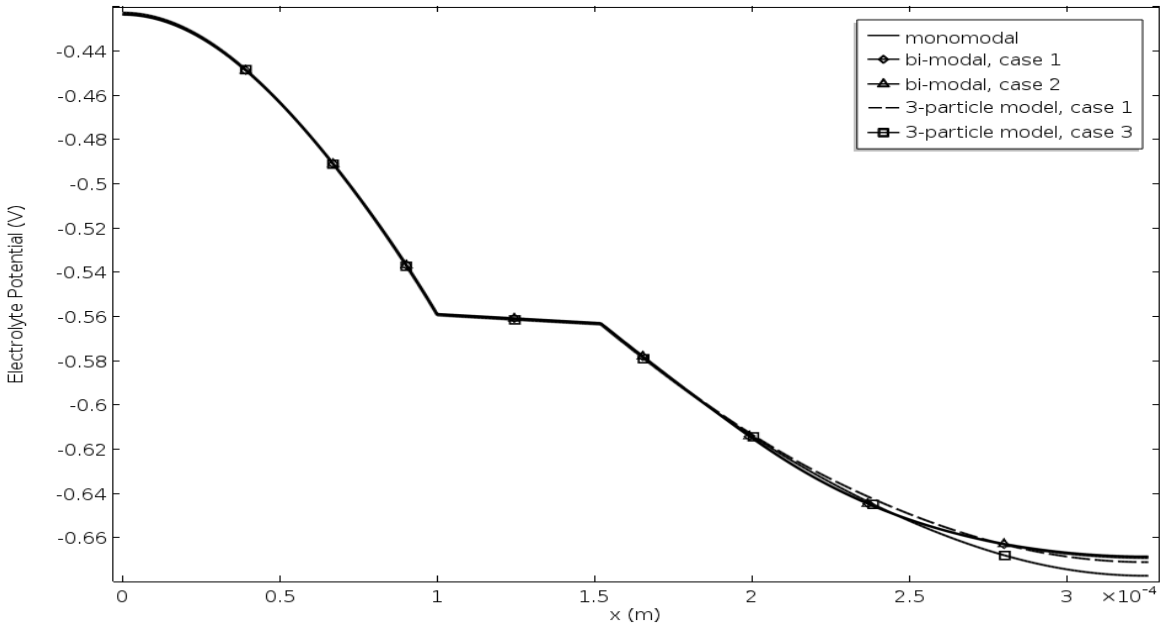

Figure 3.7: The electrolyte potential in the direction of thickness of the electrode at the end of discharge (t=1800s)

Figure 3.8 shows the Li concentration of each particle in different particle size distribution models at the surface point close to the positive current collector (point 4, Figure 3.1) during discharge. The concentration distributions in each particle arose from the different reaction rates occurring at the surface of the particle. Since the smaller particles have the highest specific surface areas, the Li intercalation reaction was faster. The local current density (A/m^2) of the particles of the different particle size distribution models during discharge time is shown in Figure 3.9. The results indicate that particle size distribution with different volume fractions affects the local current density distribution. A more uniform local current distribution is observed for case 1 of both bi-modal and 3-particle size distributions, which have a larger volume fraction of the smallest particles compared to that in the other cases. Additionally, the

non-uniformity of the local current density increased the total cell polarization as shown in Figure 3.6.

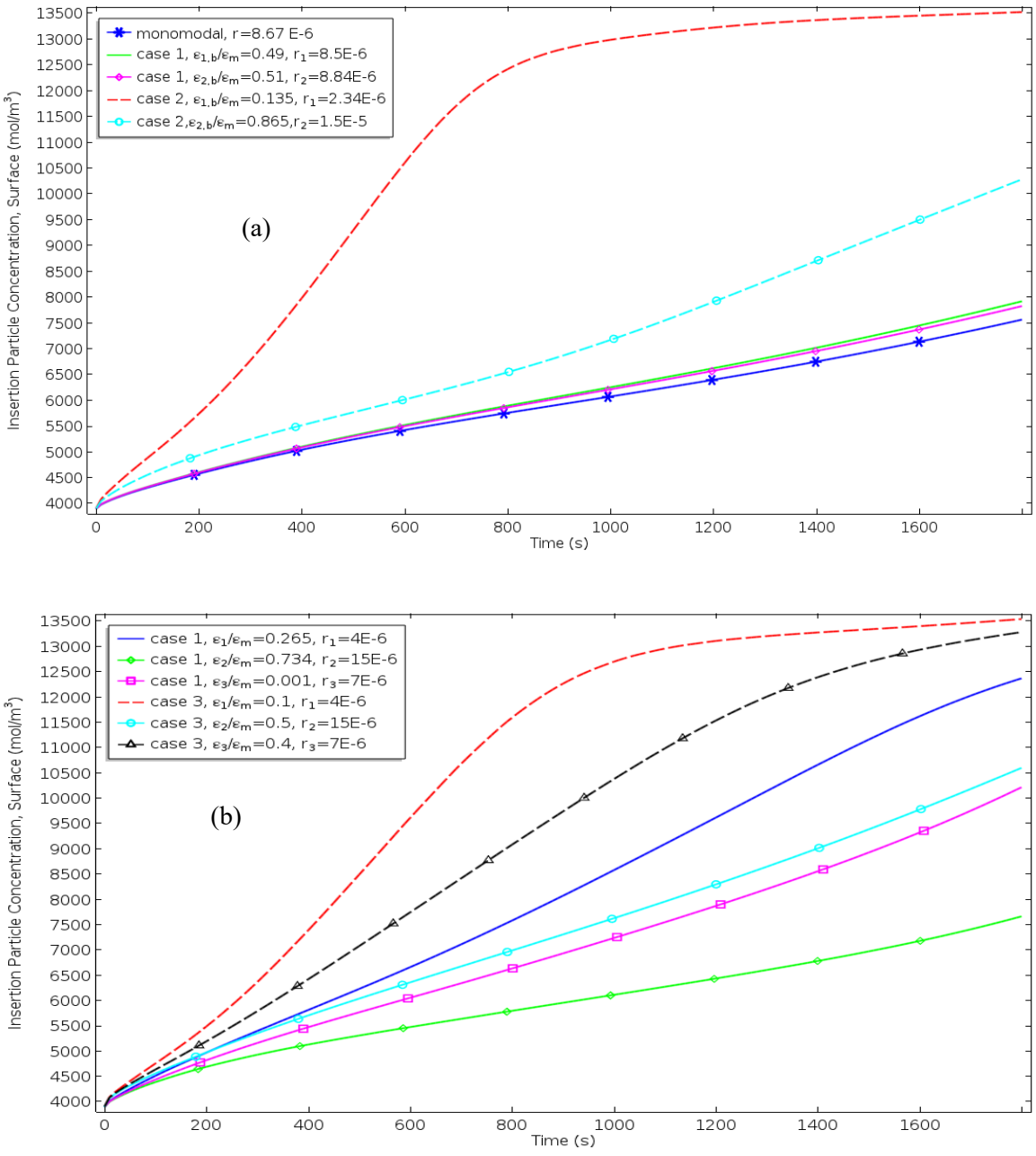

Figure 3.8: Li concentration in the particles during discharge time at the surface point next to the current collector; (a) mono-modal and bi-modal (b) 3-particle size distribution models

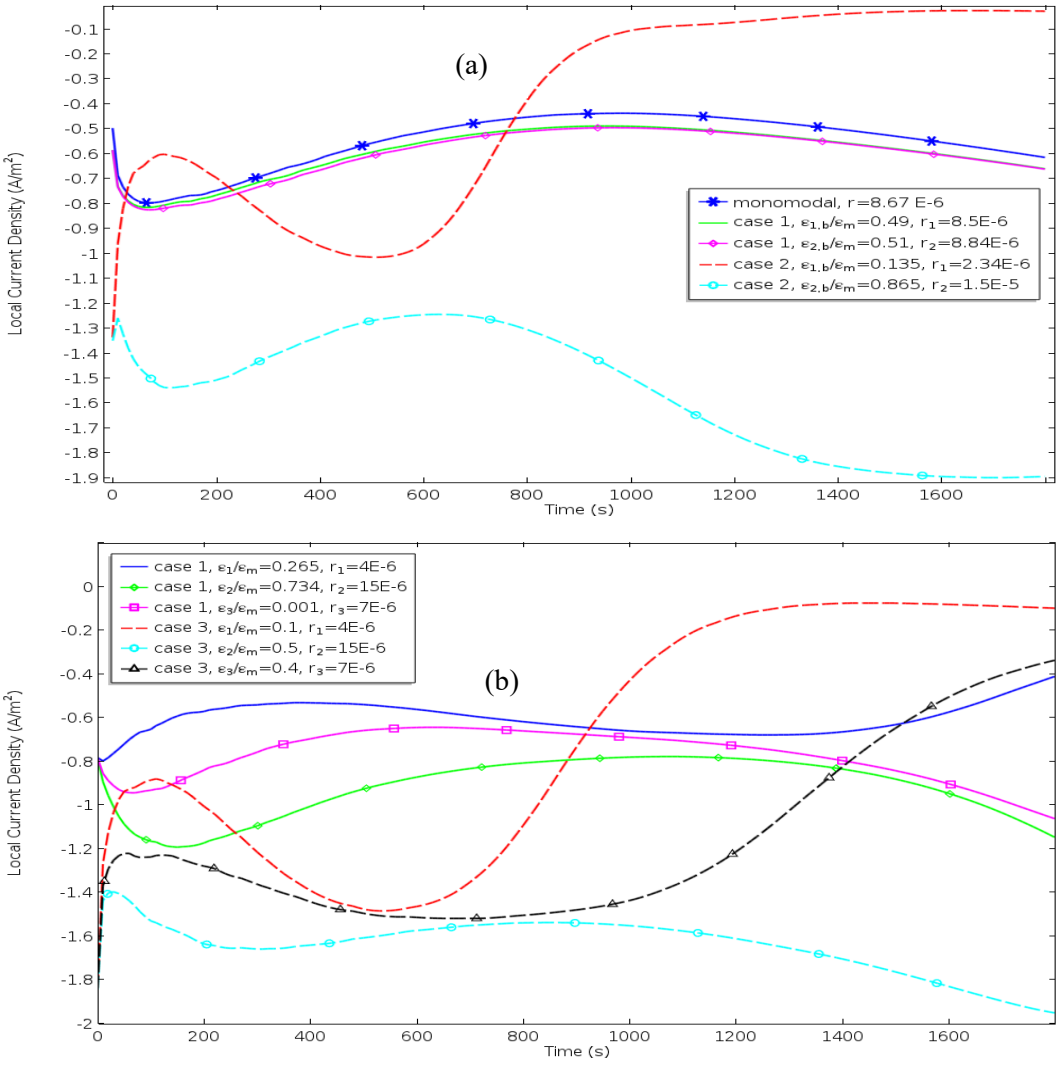

Figure 3.9: Local current density distribution during discharge time at a location next to the current collector; (a) mono-modal and bi-modal (b) 3-particle size distribution models

3.3.3 The effect of different discharge current densities

Figure 3.10 shows a comparison of the effect of the discharge current densities on the cell voltage and capacity for different particle size distributions. Different current densities were applied in accordance with the following equation

$$I = \mathrm{C} * I_{app} \tag{3.13}$$

A 1C-rate means a current density that discharges the cell in 1 hour (here it is equal to 17.5 A/m^2). At a lower discharge current density (0.1C-rate), there is a good overlap in the mono-modal and all cases of the bi-modal and 3-particle size distributions. However, the cell

voltage and cell capacity decreased dramatically at higher current densities (1C-rate and 3C-rate) due to the limitation of Li-ion migration towards the reaction zone leading to the increase of the total polarization. There were clear differences among the mono-modal and case 2 of the bi-modal and case 3 of the 3-particle size distribution at higher C-rates. The results indicated that the effect of the particle size distribution was highlighted at higher discharge current densities, and this effect was more pronounced for the 3-particle size distribution even at the highest value of the volume fraction of the smallest particle ($\varepsilon_1 = 0.265\varepsilon_m$).

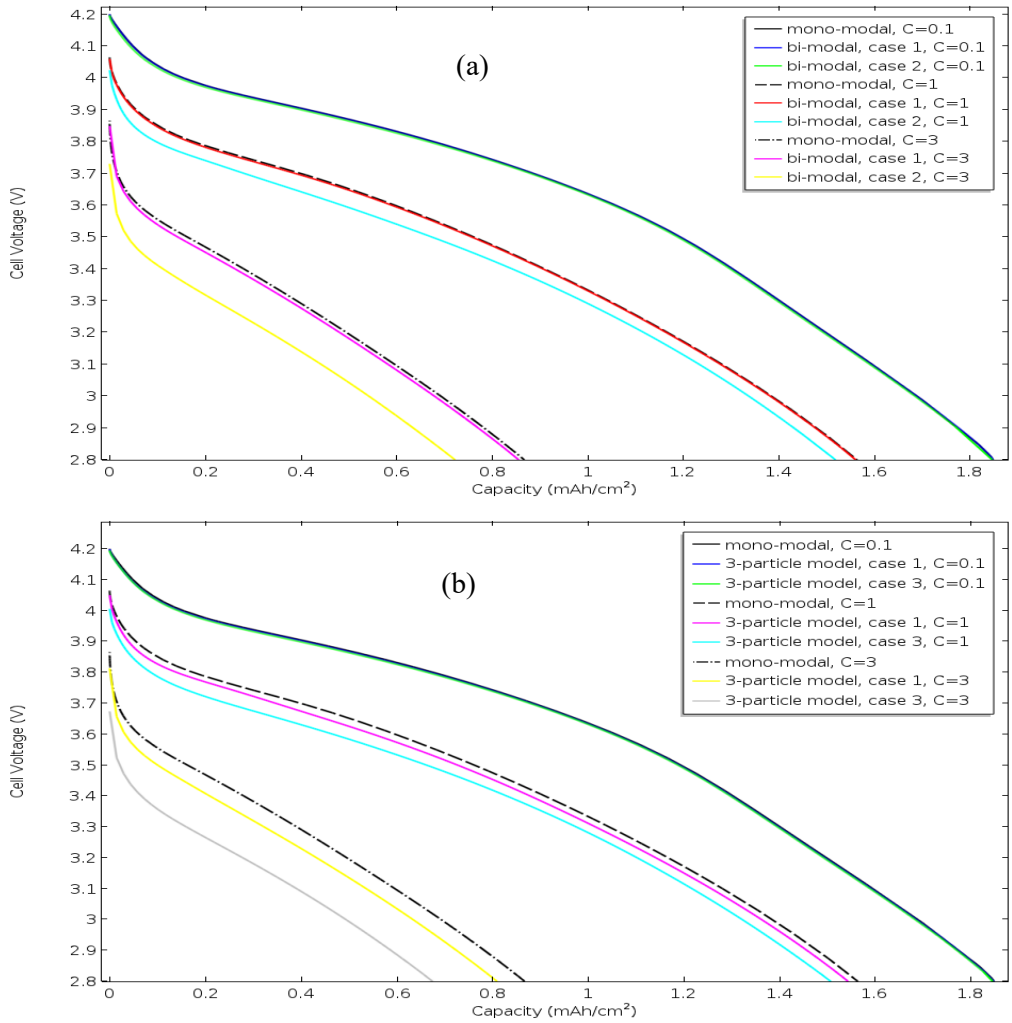

Figure 3.10: A comparison of the effect of the different discharge current densities on cell voltage of (a) mono-modal and bi-modal (b) mono-modal and 3-particle size distribution models

To clarify the effect of the particle size distribution at high discharge current densities, the specific energy curve in terms of the specific power of the cell is shown in Figure 3.11. A comparison of the three models at 1C- and 3C-rates for a final discharge cell voltage of 2.8V is presented. At a higher C-rate, the time required to reach the cut-off voltage decreased and the specific power increased. For both C-rates, the changes in specific energy, in contrast to specific

power for the three models, were minor at any specified time due to their same amount of active materials. At a 3C-rate, the differences in specific power for the three models were more distinct than that at a 1C-rate. The highest specific power was obtained with a mono-modal model as an ideal state. The specific power of the two other models was close to the ideal state (mono-modal) by increasing the volume fraction of the smallest particles in their structures.

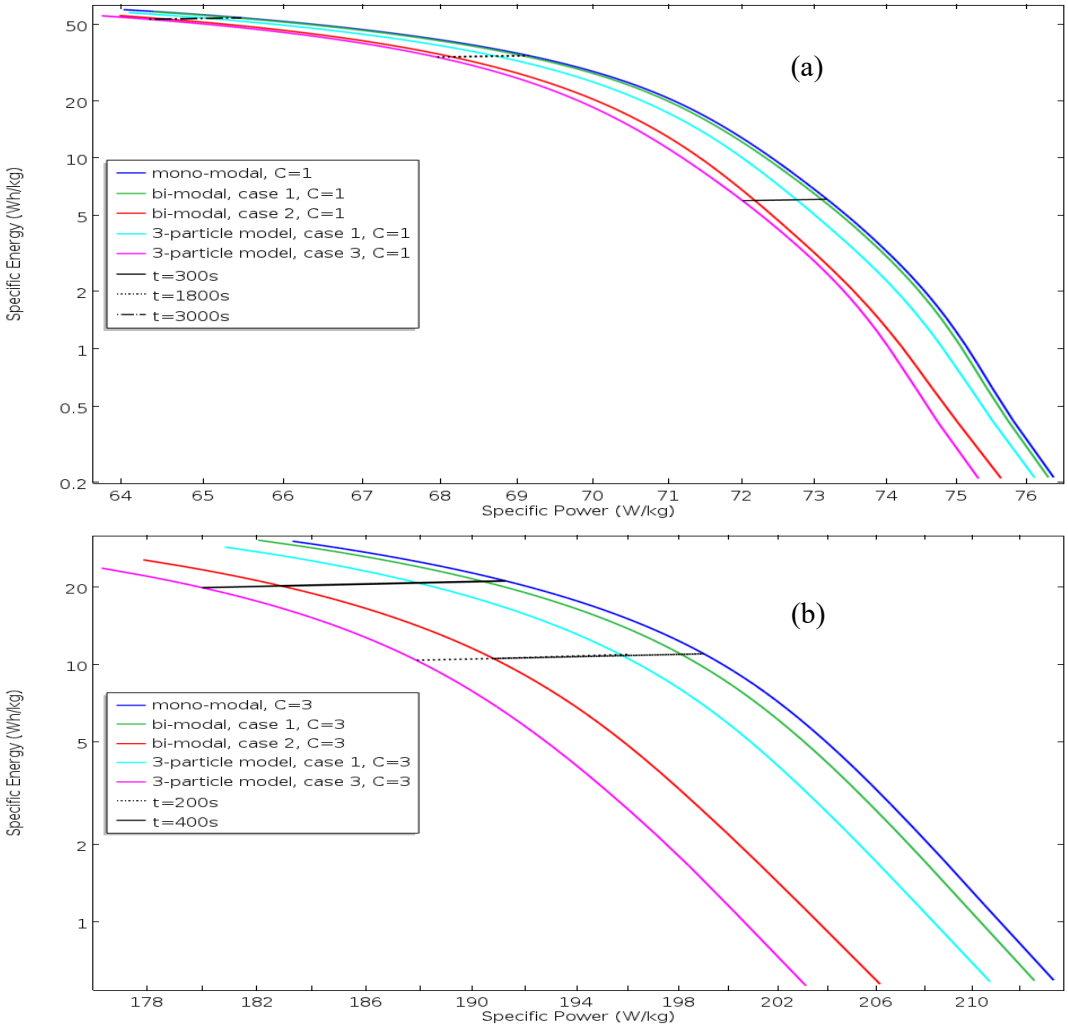

Figure 3.11: The specific energy versus the specific power for different particle size distribution models at (a) 1C-rate (b) 3C-rate

3.4 Conclusion

This work focused on studying the effect of porosity and particle size distribution on Li-ion cell performance during the discharge process. The P2D model of Doyle [7] was used to investigate different mass and charge transfer mechanisms in multi-regions of a dual Li intercalation cell**.** There was good agreement between the cell voltage of a mono-modal model simulated by COMSOL Multiphysics 5.2 and Doyle's results [7] which showed the validity of our approach.

The mono-modal model was developed further to consider bi-modal and 3-particle models to study the effect of particle size distribution in the positive electrode on the overall cell performance. The results showed that there is an optimal porosity beyond which lower cell capacities are observed due to the kinetics and mass transfer limitations in the porous electrode. A porosity of around 0.55 was found as the optimum value for achieving the maximum specific energy while an acceptable amount of specific power was sacrificed.

To study the effect of particle size distributions, mono-modal, bi-modal and 3-particle models with different volume fractions of small and large particles were considered. The results showed that increasing the volume fraction of the smallest particles in both bi-modal and 3-particle models increased the cell voltage and decreased total polarization. The non-uniformity of local current densities on particle surface was the reason of the difference among the models.

The effect of different discharge current densities or C-rates on the cell performance of different particle size distribution was studied. The effect of the particle size distribution on cell voltage, capacity and specific power was more pronounced at higher C-rates. The results showed that at 3C-rate, the difference in the specific power among the different particle size distribution models was more significant than that at 1C-rate.

Overall, the results indicated that the volume fraction of small and large particles in a bi-modal or 3-particle model has a profound effect on battery performance characteristics such as cell capacity, voltage and specific power. In fact, by increasing the portion of the smallest particles in each model, the behavior of the bi-modal and 3-particle models was closer to that of the mono-modal model as an ideal state.

3.5 Acknowledgments

The authors would like to thank Hydro-Québec and the Natural Sciences and Engineering Council of Canada (NSERC) for their financial support.

CHAPITRE 4

L'effet de propriétés structurelles d'une électrode à deux couches sur la polarisation d'une batterie Li-Ion

Titre original: The Effect of Structural Properties of a Two-Layered Electrode on the Li-Ion Battery Polarization

Auteurs et affiliation:

- **Sara Taslimi Taleghani**: étudiante au doctorat, Université de Sherbrooke, Faculté de génie, Département de génie chimique et de génie biotechnologique.
- **Bernard Marcos**: professeur, Université de Sherbrooke, Faculté de génie, Département de génie chimique et de génie biotechnologique.
- **Karim Zaghib**: Center of Excellence on Electric Transportation and Energy Storage, Hydro Québec, Varennes, Québec, J3X1S1, Canada.
- **Gaétan Lantagne**: Institut de recherche d'Hydro-Québec (IREQ), Varennes, QC, J3X 1S1, Canada.

Date d'acceptation: 23 janvier 2019

État de l'acceptation: publié

Référence: Journal of the Electrochemical Society, DOI: 10.1149/2.0681902jes

Résumé

Contenu : Cet article décrit, pour une distribution granulométrique bimodale dans une électrode poreuse positive ($Li_yMn_2O_4$), l'effet de la position des particules sur la performance d'une cellule Li-ion pendant la décharge. Les résultats ont indiqué que, pour une électrode positive composée de deux couches avec des particules de tailles différentes, la fraction volumique de particules à proximité du séparateur devrait être plus petite que celle des particules adjacentes au collecteur de courant. Dans ce cas, la solution d'électrolyte atteint plus efficacement la surface des particules à l'arrière de l'électrode (près du collecteur de courant), meilleur est le processus d'intercalation de Li dans cette zone. Cependant, il est essentiel de déterminer la valeur optimale de la fraction volumique de particules pour laquelle la cellule atteint la polarisation totale la plus faible et la valeur de voltage la plus élevée. En outre, en augmentant l'épaisseur de la couche composée de particules plus petites dans une plage de a = 1.5 à a = 2 (a est le rapport de l'épaisseur totale de l'électrode positive à l'épaisseur de la couche composée de particules plus petites), on atteint une plus faible polarisation totale des cellules.

Résultats : Les résultats présentés indiquent que, pour une conception d'électrode positive constituée d'une distribution granulométrique bimodale- indépendamment de la taille des particules- la fraction volumique de particules à proximité du séparateur doit être inférieure à celle des particules proches du collecteur de courant.

Contribution à la thèse : La principale contribution de cet article à la thèse est de mettre en évidence l'effet important de la position des particules sur la performance des batteries Li-ion. Cet article complétait le travail présenté au chapitre 3 et permettra aux fabricants de batteries de mieux concevoir leur produit.

Abstract

A complete cell model composed of a two-layered positive electrode with single-sized particles in each layer was presented to describe the effects of volume fraction of two particles distributed in the positive electrode and thickness of two layers on the Li-ion cell performance during discharge. It was determined that for such positive electrode, the volume fraction of particles near the separator should be less than the volume fraction of particles adjacent to the current collector, disregarding the particle size. In this situation, more Li-ions reach the particles surface at the back of the electrode (near the current collector) and the Li intercalation reaction proceeds more effectively. One objective of this work was to determine the optimized volume fraction of particles to obtain the lowest total polarization in the cell and the highest voltage with positive electrodes containing two layers of the same thickness. The analysis also showed that the lowest total cell polarization was achieved by increasing the thickness of the layer composed of the smaller particles in the range of $a = 1.5$ to $a = 2$, where a is the ratio of the total thickness of the positive electrode to the thickness of the layer composed of the smaller particles.

List of Symbols

a	Specific surface area, $\mathrm{m^2/m^3}$
c	Concentration of Li, $\mathrm{mol/m^3}$
c_s^0	Initial concentration of lithium in the solid phase, $\mathrm{mol/m^3}$
$c_{s,max}$	Maximum concentration of lithium in the solid phase, $\mathrm{mol/m^3}$
D	$\mathrm{Li^+}$Diffusion coefficient, $\mathrm{m^2/s}$
E_{OCP}	Open-circuit potential of the electrode, V
E_{OCV}	Open-circuit voltage of the cell, V
F	Faraday's constant, 96487, $\mathrm{C/mol}$
i_0	Exchange current density, $\mathrm{A/m^2}$
i_m	Local current density in the porous matrix, $\mathrm{A/m^2}$
I_{app}	Applied current density of cell, $\mathrm{A/m^2}$
j_m	Pore wall flux of lithium-ions, $\mathrm{mol/m^2}$ s
k	Reaction rate constant
r	Radial coordinate, m
R	Universal gas constant, 8.314 $\mathrm{J/mol\ K}$
t	Time, s
t_+^0	Transference number of species $\mathrm{Li^+}$
T	Absolute temperature, K
x	Spatial coordinate, m

Greek

α_a, α_c	Anodic and cathodic transfer coefficients
ε	Volume fraction or porosity of a phase
η	Overpotential, V
κ	Ionic conductivity of electrolyte, S/m
σ	Electronic conductivity of the solid phase, S/m
Φ	Electrical potential, V

Subscripts

ave	Average
eff	Effective value of transport property in porous medium
l	Solution phase
n	Negative electrode
p_1	The first layer of the positive electrode
p_2	The second layer of the positive electrode
s	Solid phase
sep	Separator
sur	Surface

4.1 Introduction

The concerns about the depletion of fossil fuels and the environmental problems caused by emission of carbon dioxide have led to the development of electric vehicles and various storage applications. Li-ion batteries are extensively used in the automobile industry and utilities due to their attractive features such as high energy density, high power density and cycle durability [53]. Furthermore, battery designers are making efforts to discover new electrode materials and new structures to improve battery efficiency [54], [55]. The application of mathematical models is also playing a vital role in reaching those goals.

Many researchers are using a single particle diameter or mono-modal model, but a real electrode is composed of different particle sizes and size distributions. Few researchers have focused on the impact of particles size on the cell performance [56]–[58]. In addition, the effect of particles position in the electrode was not considered in these works.

An influential theoretical model was developed by Darling and Newman [47] to study the effect of a bi-modal particle size distribution on galvanostatic cycling behaviour. A comparison between the results obtained from uniform (mono-modal) and non-uniform particle size distributions showed that the mono-modal particle size distribution has the lowest fit with the experimental data at high discharge rates. Nagarajan et al. [59] also studied the effect of particle size distribution on Li-ion cell performance during discharge. Their results indicated that the capacity of an electrode composed of two different particle sizes was higher than one with a

single particle size. Meyer et al. [48] presented a model that considers a non-uniform particle size distribution in the negative electrode, and analyzed the dependence of local state-of-charge (SOC) distribution as a function of the distance from the separator. Their results indicated that the anode reaction kinetic was faster for smaller particles due to their higher specific surface area. Additionally, Röder et al. [60] showed the effect of particle size distribution on the performance of a graphite-based electrode for a Li-ion battery. They concluded that battery degradation was significantly decreased by narrow distributions with small mean particle radii.

A comparison among mono-modal (as an ideal state), bi-modal and 3-particle size distribution models was reported in our previous paper (Chapter 3) [61]. The results showed that cell voltage, cell capacity and cell specific power were noticeably affected by the volume fraction of small and large particles. In fact, the behavior of the bi-modal and 3-particle size distribution models approached the mono-modal model by increasing the volume fraction of the smallest particles in each model. More uniform local current-density distribution profiles and lower total cell polarization were deduced from the given structural arrangement into bi-modal and 3-particle size distribution models. Recently Wu et al. [62] studied the effect of particle size distribution on the electrochemical behavior of a micro-sized silicon-based negative electrode. They indicated that the distribution of different particle size in the electrode that reduced the porosity in the electrode, decreased ion diffusion in the liquid phase.

In earlier studies, the effect of particles position was neglected and the various particle sizes were assumed to be uniformly distributed at all positions in the positive electrode. However, in the present work, the effect of particles position in the positive electrode (i.e., distance from the separator and/or current collector) was included. The novelty of this paper is the analysis of the effect of volume fraction of two particles distributed in a two-layered positive electrode with single-sized particles in each layer on voltage and the total polarization of cell. Furthermore, the effect of varying the thickness of each layer is studied. It provides a new insight into the structural effects of the electrode on the electrochemical behavior of the cell. To the best of our knowledge, this type of model has not been considered so it seems imperative to explore the subject in detail.

The present study follows our previous work (Chapter 3) [61] in which the validation of the mono-modal model was done by using Doyle's experiment and simulated results [7]. In the mono-modal model, the positive electrode consisted of a layer with single sized particles. The mono-modal model was extended to a bi-modal model in which the positive electrode was composed of two layers with single-sized particles in each layer to study (i) the effect of several volume fractions of particles in the two layers by assuming the same thickness of the two layers in the positive electrode in order to find the optimal volume fraction; and (ii) the influence of the thickness of layers to find the optimal thickness giving the lowest total cell polarization.

4.2 Model development

This work is a continuation of the effort by Taleghani et al. [61] (Chapter 3) in which various particle sizes were assumed to be uniformly distributed at all positions along the thickness of the electrode.

In the present model, the particles were considered to be located in two layers of the positive electrode. Based on the distance of particles from the separator and/or the current collector, the following states were considered:

1) First state: the first and the second layers consisted of the larger particles near the separator and the smaller particles next to the current collector.

2) Second state: the first and the second layers were composed of the smaller particles near the separator and the larger particles next to the current collector.

A pseudo two-dimensional (P2D) model following the model by Doyle [19] was developed as a bi-modal model.

In recent years, many researchers used Doyle's model [19] to guide the improvement of battery performance [13], [22], [24], [52], [63], [64]. Based on Doyle's work [19], a model of a dual Li-ion intercalation cell consisting of a negative current collector (Cu), negative porous electrode (Li_xC_6), separator, positive porous electrode ($Li_yMn_2O_4$) and positive current collector (Al) was constructed. The plasticized electrolyte that includes $LiPF_6$ salt in a liquid mixture of ethylene carbonate and dimethyl carbonate, as well as a copolymer from vinylidene fluoride and hexafluoropropylene was considered. A list of physical and structural parameters extracted from Doyle's model [7] is presented in Table 4.1. The superficial current density (I_{app}) of 17.5 A/m^2 is applied to the positive electrode/current collector interface. The discharge time is considered to be 1800 s. The temperature is constant and equal to the room temperature (T=298.15 K).

Figure 4.1 shows that the negative electrode, separator and positive electrode were modeled as a 1D geometry, and Li diffusion in the negative and positive electrodes was modeled as a two-dimensional (2D) geometry. The solid-phase diffusion in the x direction of the 2D geometry was neglected, while Li diffusion in the r-direction (vertical coordinate) of the solid phase was considered. All mass and charge equations were solved in the x direction of the 1D geometry, except for the Li diffusion equation in the solid phase, which followed Fick's law of diffusion in the r-direction of the 2D geometry. The pore wall flux calculated in the 1D geometry was linked to the top boundary of the 2D geometry (particle surface or pore mouth), and the concentration of Li at the top boundary of the 2D geometry was coupled to the equations defined for the 1D geometry by using a linear extrusion coupling variable in COMSOL Multiphysics. With this approach, all charge and mass transport mechanisms were described in detail. A summary of the governing equations of the model and the corresponding boundary conditions are presented in Table 4.2. As observed in Table 4.2, the ionic conductivity of electrolyte is considered as a function of salt concentration [7].

The sum of mass of the particles in two layers of positive electrode in the bi-modal model is assumed to be the same as that in positive electrode of mono-modal model. By using this assumption, the correlation between the volume fractions of the particles in the two models was obtained as follows:

$$\frac{(a-1)*\varepsilon_{large,b}+\varepsilon_{small,b}}{a}=\varepsilon_{mono-modal} \tag{4.1}$$

Where $\varepsilon_{mono-modal}$, $\varepsilon_{large,b}$ and $\varepsilon_{small,b}$ are the volume fraction of particles in the positive electrode of the mono-modal model and the volume fraction of large and small particles in the layers constituting the positive electrode of the bi-modal model, respectively. The parameter a represents the ratio of the total positive electrode thickness to the thickness of the layer composed of small particles in the positive electrode:

$$\frac{L_{tot}}{L_{small,b}} = \mathrm{a} \tag{4.2}$$

The porosity is considered to be dependent on the volume fractions of conductive filler and polymer phase of plasticized electrolyte [7].

$$\varepsilon_l = 1 - \varepsilon_s - \varepsilon_{filler} - \varepsilon_{polymer} \tag{4.3}$$

Table 4.1: List of model parameters [7]

Parameter	Symbol	Li_xC_6	Separator	$Li_yMn_2O_4$
Li^+ Diffusion coefficient (m^2/s)	D	3.9×10^{-14}	9×10^{-11}	1×10^{-13}
Electronic conductivity (S/m)	σ	100		3.8
Initial concentration of lithium in the solid phase (mol/m^3)	c_s^0	14870		3900
Initial concentration of Li^+ in the solution phase (mol/m^3)	c_l^0	2000	2000	2000
Maximum concentration of lithium in the solid phase (mol/m^3)	$c_{s,max}$	26390		22860
Anodic and cathodic transfer coefficients	α	0.5		0.5
Representative thicknesses of the mono-modal model (m)	$L_{mono-modal}$	1×10^{-4}	52×10^{-6}	174×10^{-6}
Electrode volume fraction of mono-modal model	$\varepsilon_{mono-modal}$	0.471		0.297
Volume fraction of polymer phase of plasticized electrolyte	$\varepsilon_{polymer}$	0.146		0.186
Conductive filler volume fraction	ε_{filler}	0.026		0.073
Transference number of species Li^+	t_+^0		0.363	

Table 4.2: Governing equations and boundary conditions for the positive electrode, the negative electrode and the separator in a P2D model (x and r)

Governing equations	**Boundary conditions**		
	Positive electrode	**Negative electrode**	**Separator**
Mass balance in the electrolyte for a binary salt concentrated electrolyte $\varepsilon_m \frac{\partial c_l}{\partial t} = D_{eff,m} \frac{\partial^2 c_l}{\partial x^2} + a_m(1 - t_+^0) j_m$ Initial condition $c_l\|_{t=0} = c_0$ $m = p_1, p_2, n$ **Hypotheses** Solvent velocity equals to zero Constant transport properties integrating non-ideality effect Constant porosity Structural properties-porosity and tortuosity-integrated in $D_{eff,m}$ No reaction in the separator	$c_l\|_{x=L_n+L_{sep},-} = c_l\|_{x=L_n+L_{sep},+}$ $-D_{eff,p_1} \frac{\partial c_l}{\partial x}\Big\|_{x=L_n+L_{sep}+L_{p_1},-} = -D_{eff,p_2} \frac{\partial c_l}{\partial x}\Big\|_{x=L_n+L_{sep}+L_{p_1},+}$ $c_l\|_{x=L_n+L_{sep}+L_{p_1},-} = c_l\|_{x=L_n+L_{sep}+L_{p_1},+}$ $-D_{eff,p_2} \frac{\partial c_l}{\partial x}\Big\|_{x=L_n+L_{sep}+L_{p_1}+L_{p_2}} = 0$	$-D_{eff,n} \frac{\partial c_l}{\partial x}\Big\|_{x=0} = 0$ $-D_{eff,n} \frac{\partial c_l}{\partial x}\Big\|_{x=L_n,-} = -D_{sep} \frac{\partial c_l}{\partial x}\Big\|_{x=L_n,+}$	$c_l\|_{x=L_n,-} = c_l\|_{x=L_n,+}$ $-D_{sep} \frac{\partial c_l}{\partial x}\Big\|_{x=L_n+L_{sep},-} = -D_{eff,p_1} \frac{\partial c_l}{\partial x}\Big\|_{x=L_n+L_{sep},+}$
$D_{eff} = \varepsilon^{3.3} D$			
Potential distribution in solution $\nabla(-\kappa_{eff,m} \frac{\partial \varphi_l}{\partial x} + \frac{2\kappa_{eff,m} RT}{F}(1 - t_+^0) \frac{\partial \ln c_l}{\partial x}) = a_m F j_m$ **Hypotheses** Structural properties-porosity and tortuosity-integrated in $\kappa_{eff,m}$ No reaction in the separator	$\varphi_l\|_{x=L_n+L_{sep},-} = \varphi_l\|_{x=L_n+L_{sep},+}$ $i_l\|_{x=L_n+L_{sep}+L_{p_1},-} = i_l\|_{x=L_n+L_{sep}+L_{p_1},+}$ $\varphi_l\|_{x=L_n+L_{sep}+L_{p_1},-} = \varphi_l\|_{x=L_n+L_{sep}+L_{p_1},+}$ $i_l\|_{x=L_n+L_{sep}+L_{p_1}+L_{p_2}} = 0$	$i_l\|_{x=0} = 0$ $i_l\|_{x=L_n,-} = i_l\|_{x=L_n,+}$	$\varphi_l\|_{x=L_n,-} = \varphi_l\|_{x=L_n,+}$ $i_l\|_{x=L_n+L_{sep},-} = i_l\|_{x=L_n+L_{sep},+}$
$\kappa = 1.0793 * 10^{-2} + 6.7461 * 10^{-1} c_l - 5.2245 * 10^{-1} {c_l}^2 + 1.3605 * 10^{-1} {c_l}^3 - 1.1724 * 10^{-2} {c_l}^4$ $\kappa_{eff} = \varepsilon^{3.3} \kappa$			
Potentiel distribution in matrix/solid phase $\sigma_{eff,m} \frac{\partial^2 \varphi_s}{\partial x^2} = a_m F j_m$ **Hypotheses** Structural properties-porosity and tortuosity-integrated in $\sigma_{eff,m}$	$i_s\|_{x=L_n+L_{sep}} = 0$ $i_s\|_{x=L_n+L_{sep}+L_{p_1},-} = i_s\|_{x=L_n+L_{sep}+L_{p_1},+}$ $\varphi_s\|_{x=L_n+L_{sep}+L_{p_1},-} = \varphi_s\|_{x=L_n+L_{sep}+L_{p_1},+}$ $\frac{\partial \varphi_s}{\partial x}\Big\|_{x=L_n+L_{sep}+L_{p_1}+L_{p_2}} = -\frac{I_{app}}{\sigma_{eff,p_2}}$	$\varphi_s\|_{x=0} = 0$ $i_s\|_{x=L_n} = 0$	
$\sigma_{eff} = \varepsilon^{1.5} \sigma$			
Mass balance-solid-state diffusion only- in the matrix/solid phase in spherical coordinates $\frac{\partial c_s}{\partial t} = \frac{1}{r^2} \frac{\partial}{\partial r}\left(D_m r^2 \frac{\partial c_s}{\partial r}\right)$ Initial condition $c_s\|_{t=0} = c_s^0$	$\frac{\partial c_s}{\partial r}\Big\|_{r=0} = 0 \quad and \quad -D_m \frac{\partial c_s}{\partial r}\Big\|_{r=R_m} = j_m$		
Reaction rate at the surface of particles (Butler-Volmer equation)			
$i_m = i_0 \left(exp\left(\frac{\alpha_a F(\Phi_s - \Phi_l - E_{OCP}(SOC))}{RT}\right) - exp\left(-\frac{\alpha_c F(\Phi_s - \Phi_l - E_{OCP}(SOC))}{RT}\right)\right)$ $i_0 = F\, k\, (c_{s,max} - c_s)^{\alpha_a} (c_s)^{\alpha_c} (c_l)^{\alpha_a}$			
The relation between the reaction rate and the pore wall flux			
$i_m = F j_m$			

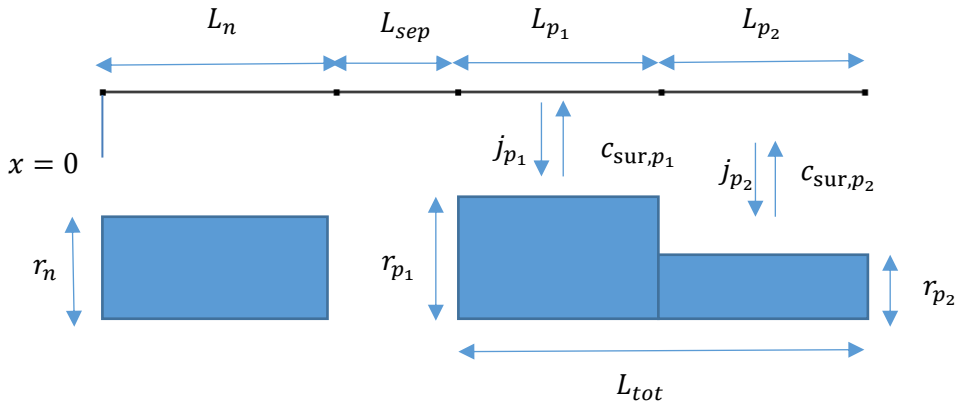

Figure 4.1: A representation of a P2D model

4.2.1 Total cell polarization

The total cell polarization (η_{tot}) is the difference between the cell voltage (E_{cell}) and the cell open circuit voltage ($E_{OCV,cell}$). It was calculated by the following equation:

$$\eta_{tot} = E_{OCV,cell} - E_{cell} \tag{4.4}$$

Referring to Nyman's paper, the total cell polarization is the summation of different polarizations or internal losses occurring in different areas of the cell, as shown in Table 4.3 [65]:

Table 4.3: Polarization calculations [65]

Diffusion polarization- electrolyte phase	$-\frac{1}{\int_0^L a i_{loc}\,dx}\int_0^L \frac{2RT}{C_l F}(1-t_+^0)\frac{\partial C_l}{\partial x} i_l dx$
Diffusion polarization- solid phase	$\frac{1}{\int_0^L a i_{loc}\,dx}\int_0^L a i_{loc}\,(E_{OCP}(SOC_{sur}) - E_{OCP}(SOC_{ave}))dx$
Ohmic potential drop- electrolyte phase	$\frac{1}{\int_0^L a i_{loc}\,dx}\int_0^L \frac{i_l^2}{\kappa_{eff}}dx$
Ohmic potential drop- solid phase	$\frac{1}{\int_0^L a i_{loc}\,dx}\int_0^L \frac{i_s^2}{\sigma_{eff}}$
Activation overpotential	$\frac{1}{\int_0^L a i_{loc}\,dx}\int_0^L a i_{loc}\,(\Phi_s - \Phi_L - E_{OCP}(SOC_{sur}))dx$

4.2.2 Numerical Solution

All equations were solved by COMSOL Multiphysics 5.2 software. A linear extrusion coupling variable in COMSOL Multiphysics 5.2 was applied to link the 1D and 2D geometries to each other. A time-dependent solver and a direct solver of MUMPS (MUltifrontal Massively Parallel sparse direct Solver) were used to solve the equations. The Absolute tolerance was equal to 0.001. The geometry was discretized automatically using a physics-controlled mesh with normal size. The solution time was less than one minute. The results deduced from the simulations are presented in the next section.

4.3 Results and Discussion

In our previous work (Chapter 3) [61], the cell voltage-capacity data of a mono-modal model simulated by COMSOL Multiphysics 5.2 was validated with the experimental and simulated data of Doyle [7]. In the present work, the mono-modal model was extended to a bi-modal model in which the negative electrode was assumed to have a uniform particle size distribution while the positive electrode was composed of two layers with single-sized particles in each layer. Two states for the two layers of the positive electrode were considered: the first layer (next to the separator) was composed of larger particles and the second layer (next to the current collector) consisted of smaller particles. The second state was the reverse of the first one described previously.

Guyomard and Tarascon [66] indicated that a representative range of particle radii in a composite $Li_yMn_2O_4$ electrode was between 5 to 15μm. Based on this range, two particle radii of 7 μm and 15 μm were selected as typical bi-modal particle sizes in the positive electrode.

4.3.1 The effect of particles volume fraction in the positive electrode on cell performance

This section presents the effect of the volume fraction of particles in the positive electrode on cell performance, namely cell voltage and total polarization in the cell. The thickness of the two layers constituting the positive electrode was assumed to be the same and equal to half the thickness of that in the mono-modal model (a=2). Furthermore, the first layer of the positive electrode was composed of larger particles and the second layer consisted of smaller particles. Table 4.4 illustrates a volume fraction distribution in the first and the second layers of the positive electrode.

The effect of volume fractions on cell voltage-capacity curves is shown in Figure 4.2. By increasing the volume fraction of smaller particles in the second layer from 0.15 to 0.35 and decreasing the volume fraction of larger particles in the first layer from 0.444 to 0.244, the cell voltage curve approached the mono-modal curve as an ideal state. However, as the volume fraction of smaller particles increased, and the volume fraction of larger particles decreased beyond the specific values of 0.35 and 0.244, respectively, the cell voltage decreased sharply.

Table 4.4: Volume fraction distribution of particles in the positive electrode of a bi-modal model

Volume fraction of larger particles in the first layer (ε_{large,p_1})	Volume fraction of smaller particles in the second layer (ε_{small,p_2})
0.444	0.15
0.394	0.2
0.294	0.3
0.244	0.35
0.194	0.4
0.144	0.45
0.094	0.5

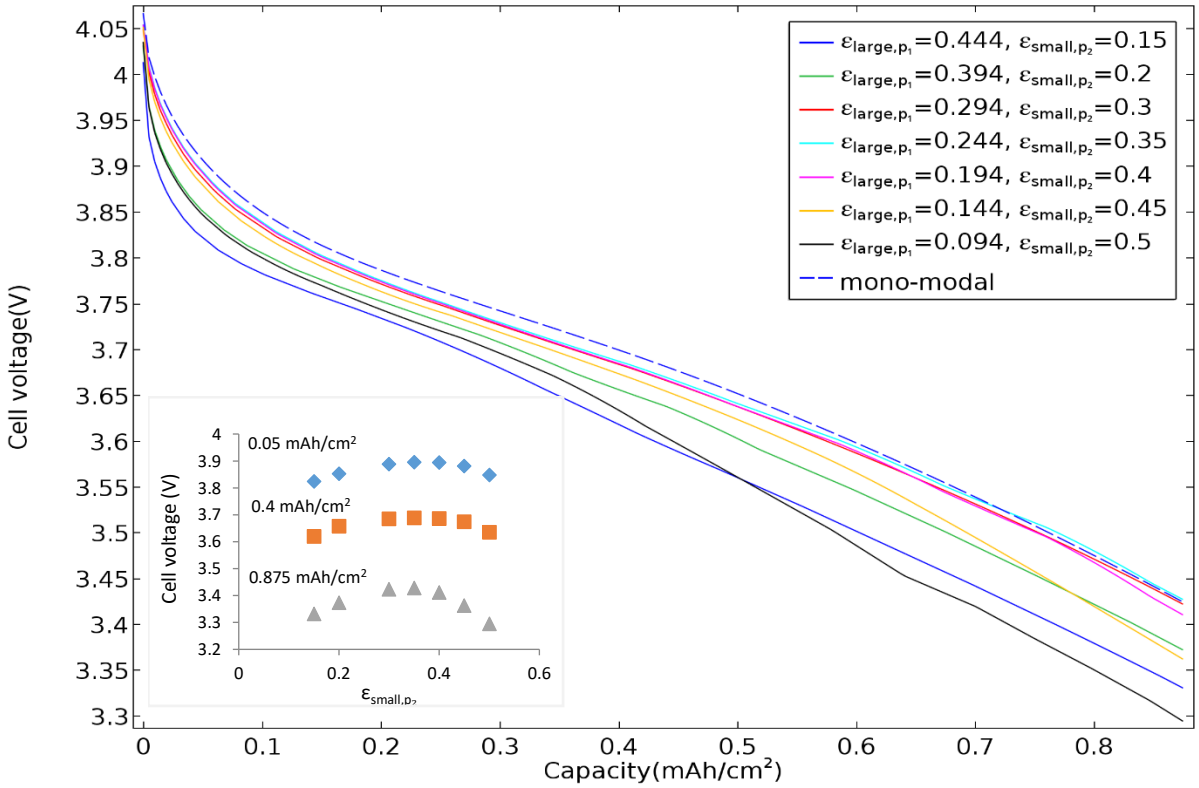

Figure 4.2: Cell voltage versus capacity during discharge for different volume fractions of particles in the positive electrode. Inset: Cell voltage plotted against volume fraction of small particles at selected capacities

At $\varepsilon_{large,p_1} = 0.094$, the first layer has the low amount of active materials and the high porosity. This implies that the concentration decrease in the first layer is low, as seen in Figure 4.3. With a higher ion concentration in the electrolyte, its migration is higher and the potential drop is low in the first layer, as shown in Figure 4.4. The same argument justifies the regular behaviour observed with a higher fraction of large particles in the first layer from $\varepsilon_{large,p_1} = 0.094 < \varepsilon_{large,p_1} = 0.244 < \varepsilon_{large,p_1} = 0.394$.

The analysis of the concentration and potential decrease in the second layer is based on the concentration at the interface between the first and second layer, as well as the volume fraction of small particles in the second layer of the positive electrode.

The case represented by $\varepsilon_{large,p_1} = 0.094$ and $\varepsilon_{small,p_2} = 0.5$ in Figure 4.3 shows that the Li-ions concentration is the highest at the interface between layer 1 and layer 2. Furthermore, with $\varepsilon_{small,p_2} = 0.5$ in the second layer, we have the highest volume fraction of small particles and thus the highest amount of active materials. With those conditions in mind, we expect the sharpest decrease in concentration up to a point where the electrolyte is depleted, as shown in Figure 4.3. The potential drop is directly linked to the decrease in electrolyte concentration, which leads to a sharp potential drop in the second layer. In this situation, mass and charge transport limitations in the solution phase of the second layer is more pronounced.

At the other extreme represented by $\varepsilon_{large,p_1} = 0.394$ and $\varepsilon_{small,p_2} = 0.2$, since the volume fraction of particles in the first layer was larger than that in the second layer, there were the highest amount of active materials and the lowest porosity in this layer leading to a limitation in Li-ions reaching the reaction zone. Thus, the concentration and potential drop in the solution phase of the first layer increased. This is clearly shown in Figure 4.3 and Figure 4.4 and reveals that the electrochemical phenomena occur predominately in layer 1.

Finally, at $\varepsilon_{large,p_1} = 0.244$ and $\varepsilon_{small,p_2} = 0.35$, both layer 1 and layer 2 are clearly active during the discharge of the battery.

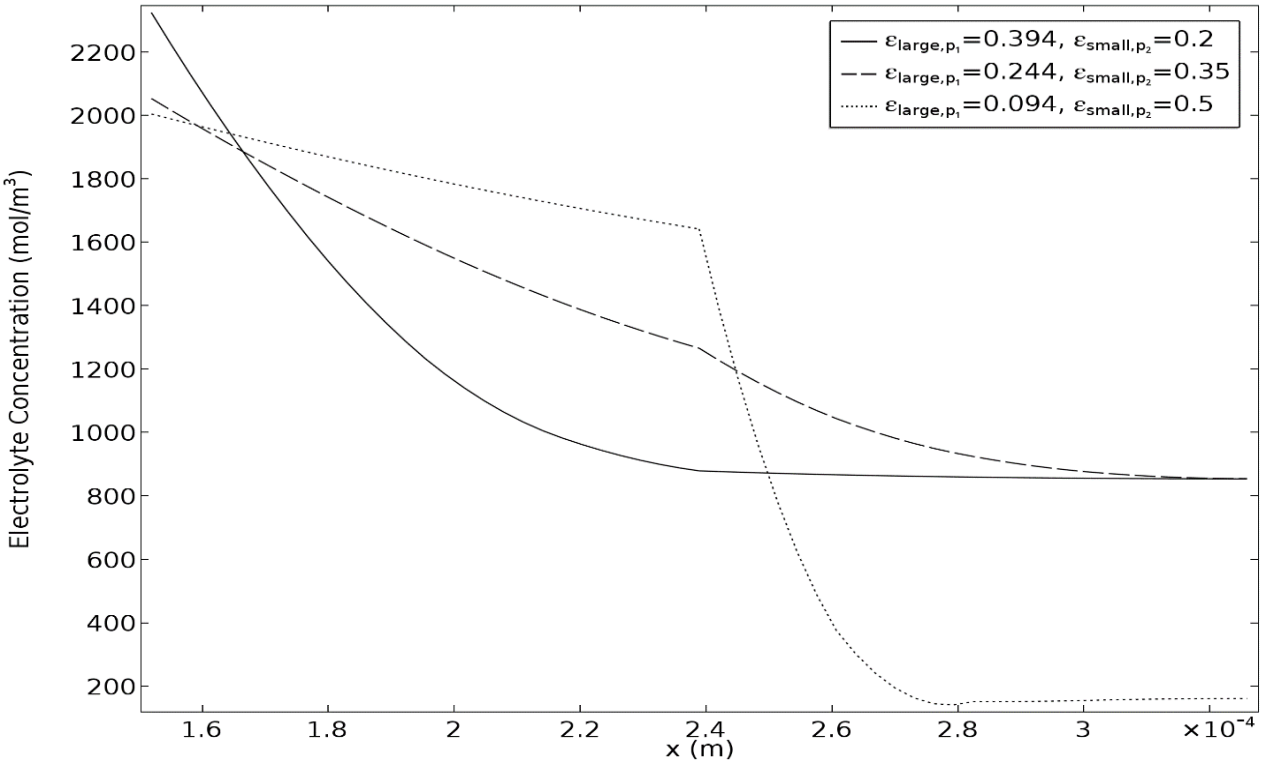

Figure 4.3: Electrolyte concentration in the direction of thickness of the positive electrode at the end of discharge (t=1800s)

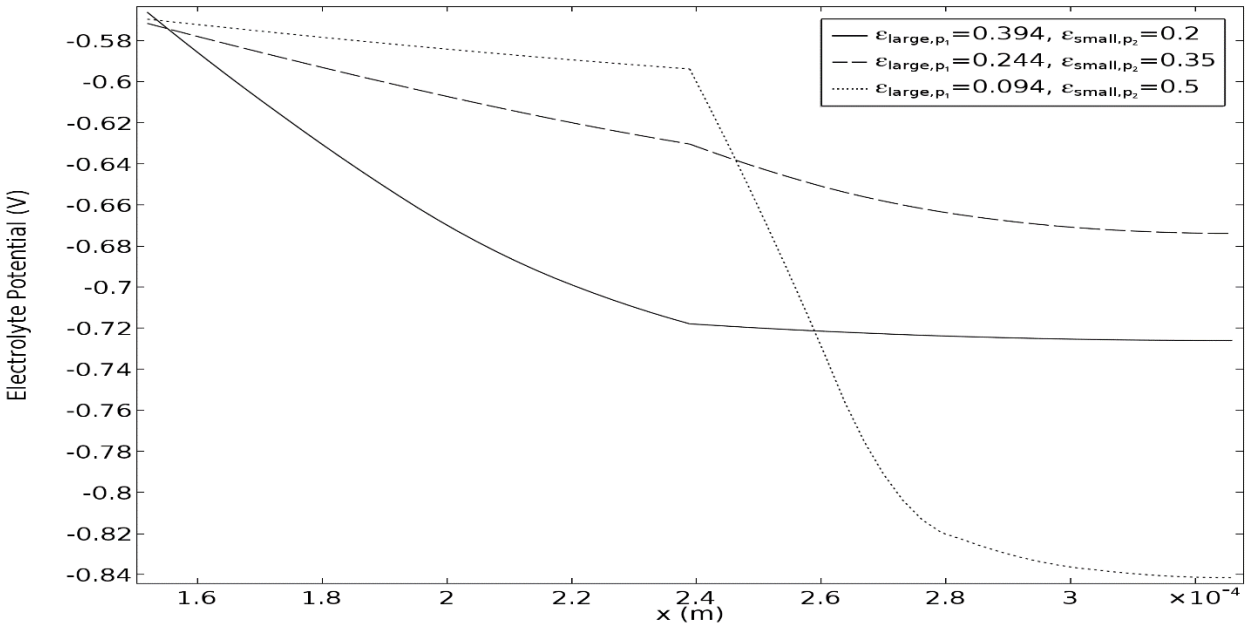

Figure 4.4: Electrolyte potential in the direction of thickness of the positive electrode at the end of discharge (t=1800s)

As a complementary analysis, it is useful to analyze the solid-state concentration profile from the state of charge (SOC), which is the ratio of solid phase concentration to maximum concentration in the positive electrode at the end of discharge (t=1800s), as shown in Figure 4.5. The results illustrate a more uniform SOC distribution in the positive electrode at $\varepsilon_{large,p_1} = 0.244$ and $\varepsilon_{small,p_2} = 0.35$. At $\varepsilon_{large,p_1} = 0.394$ and $\varepsilon_{small,p_2} = 0.2$, the difference in SOC along the thickness of the first layer was higher than for the second layer. At $\varepsilon_{large,p_1} = 0.094$ and $\varepsilon_{small,p_2} = 0.5$, the heterogeneities of SOC in the second layer was more significant. In fact, the SOC distributions along the thickness of the positive electrode is congruent with the analysis presented above and is linked to the rate of Li intercalation occurring at the surface of the particles.

Table 4.5 summarizes the total cell polarization for different volume fraction of particles in the positive electrode at the end of discharge (t=1800s). The total cell polarization was calculated by Eq. (4.4). As predicted, the minimum polarization is related to the case of $\varepsilon_{large,p_1} = 0.244$ and $\varepsilon_{small,p_2} = 0.35$. The contribution from polarization of each transport mechanism (η_i) in the cell to the total polarization (η_{tot}) is illustrated as a bar chart in Figure 4.6. As observed in Figure 4.6, the ohmic potential drop in the electrolyte and the activation overpotential were the two major sources of polarization in the positive electrode. At $\varepsilon_{large,p_1} = 0.244$ and $\varepsilon_{small,p_2} = 0.35$, the diffusion polarization in solid phase of positive electrode is insignificant compared to the ohmic potential drop in the electrolyte and the activation overpotential polarization. At $\varepsilon_{large,p_1} = 0.394$ and $\varepsilon_{small,p_2} = 0.2$, the percentage of the polarization in the first layer dominates, whereas at $\varepsilon_{large,p_1} = 0.094$ and $\varepsilon_{small,p_2} = 0.5$, the total polarization in the second layer dominates in the positive electrode. It is evident that the high polarization of the negative electrode plays an important role in the cell.

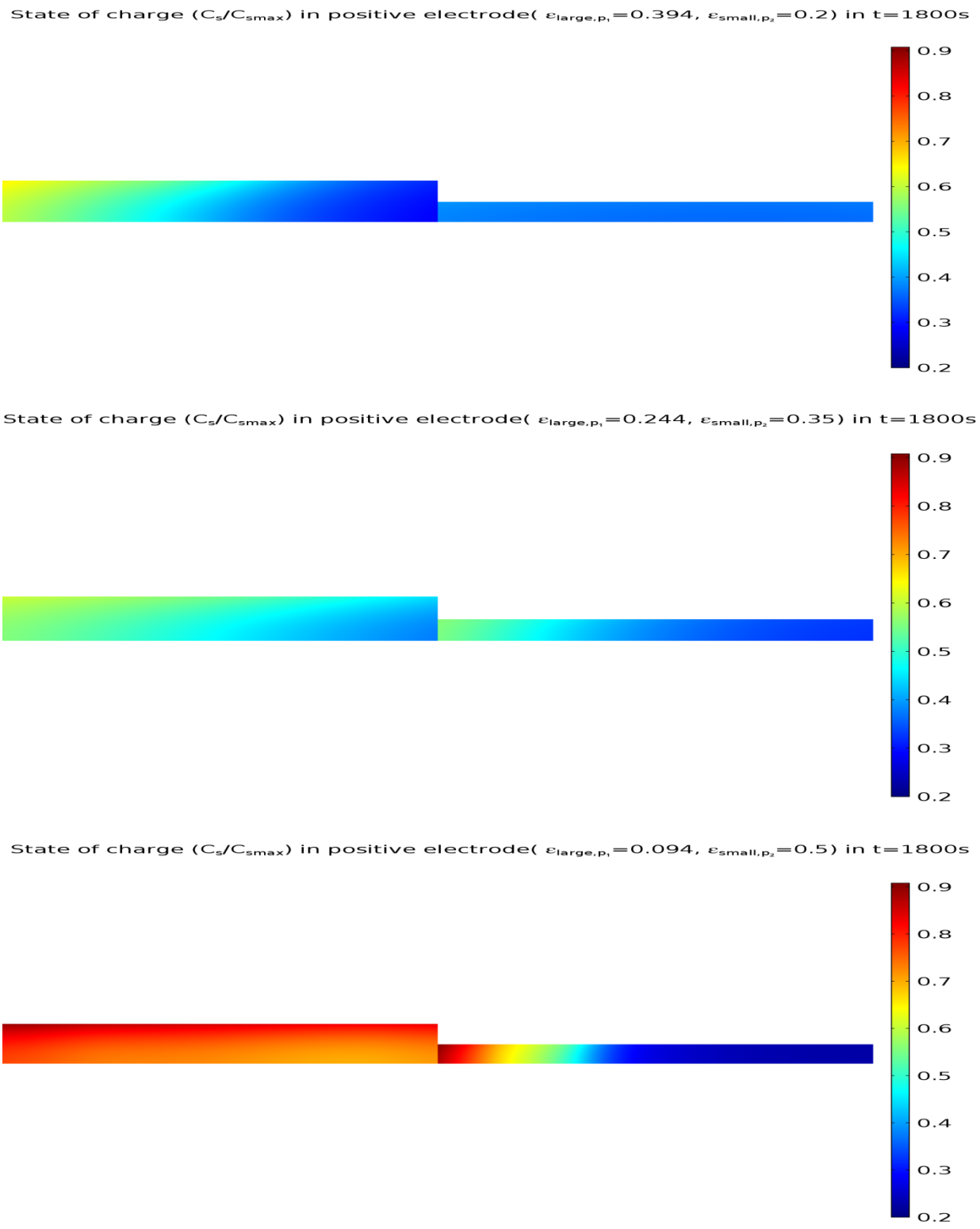

Figure 4.5: SOC distribution in the positive electrode at the end of discharge (t=1800s)

Table 4.5: The total cell polarization at the end of discharge (t=1800s)

Total polarization (V)		
$\varepsilon_{large,p_1} = 0.394, \varepsilon_{small,p_2} = 0.2$	$\varepsilon_{large,p_1} = 0.244, \varepsilon_{small,p_2} = 0.35$	$\varepsilon_{large,p_1} = 0.094, \varepsilon_{small,p_2} = 0.5$
0.42	0.35	0.45

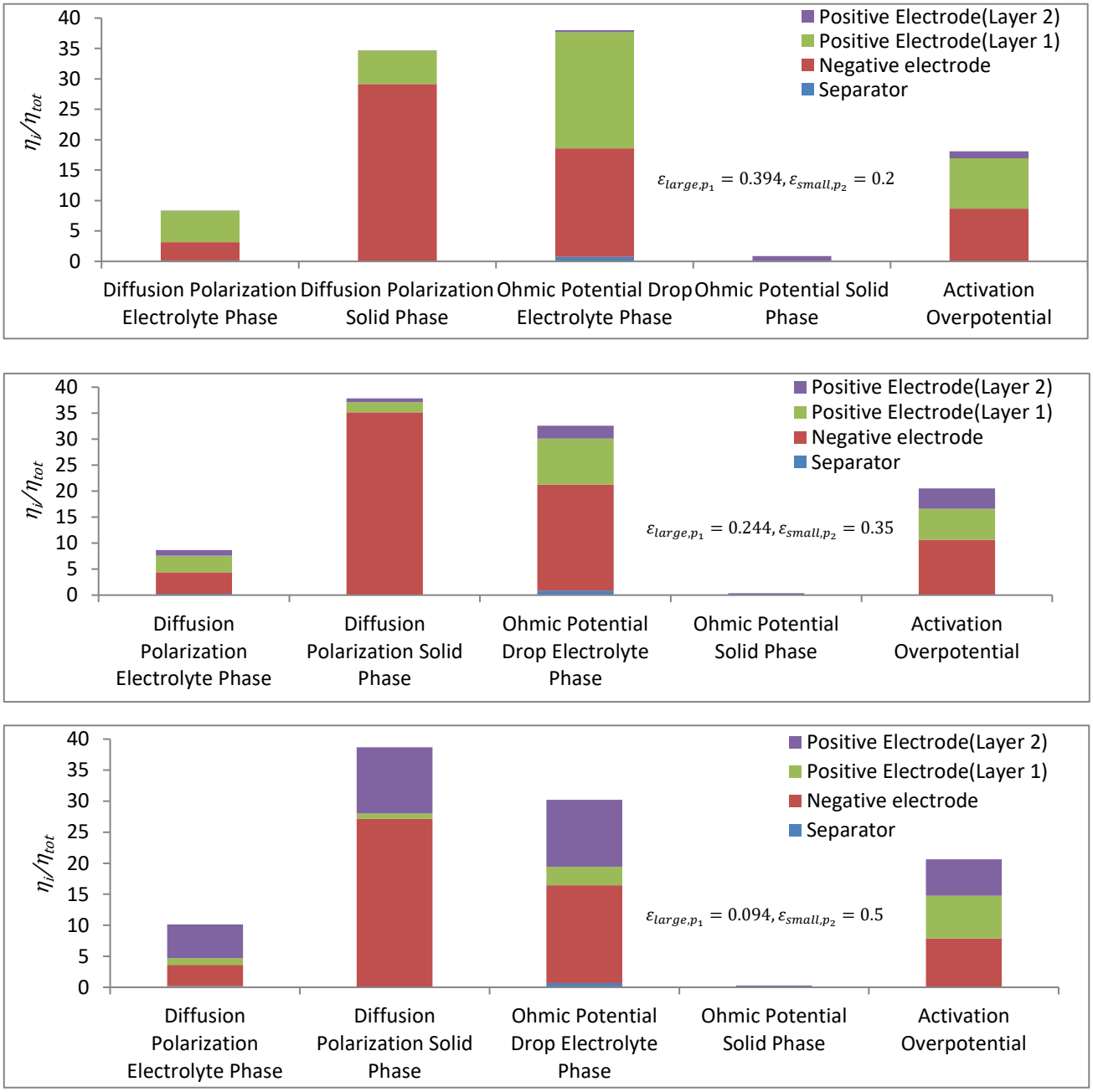

Figure 4.6: A bar chart of the ratio of each polarization to the total cell polarization

In the second state, it was assumed that smaller and larger particles were located in the first layer next to the separator and in the second layer close to the current collector, respectively. Table 4.6 lists the volume fraction distribution of small and large particles in the first and the second layers of the positive electrode.

Table 4.6: Volume fraction distribution of particles in the positive electrode of a bi-modal model

Volume fraction of smaller particles in the first layer (ε_{small,p_1})	Volume fraction of larger particles in the second layer (ε_{large,p_2})
0.1	0.494
0.2	0.394
0.28	0.314
0.35	0.244
0.4	0.194
0.5	0.094

A comparison of the cell voltage versus capacity during discharge time for different volume fractions of particles is shown in Figure 4.7. The best agreement with a mono-modal model was found at $\varepsilon_{small,p_1} = 0.28$ and $\varepsilon_{large,p_2} = 0.314$. An increase over 0.28 and a decrease over 0.314 in the volume fraction of particles decreased the cell voltage dramatically. As observed for the first state, an optimal value of volume fraction of small and large particles in the two layers of the positive electrode of a Li-ion battery is present.

Figure 4.8 shows the SOC distribution in the two layers of the positive electrode for these two volume fractions. The first layer has a higher SOC compared to the second layer due to the higher specific surface area of the smaller particles, and also their proximity to the separator which facilitated their availability to Li-ions.

Recently, some research showed that varying porosity in an electrode composed of a uniform particle size distribution (mono-modal) has no significant improvement in energy density of cell compared to a constant-porosity model [44], [67]. The results explicated in this section confirm the results of previous studies. Our results indicated that there is no improvement in cell polarization and voltage by varying the porosity in an electrode composed of two particles compared to a constant porosity electrode with uniform particle size distribution.

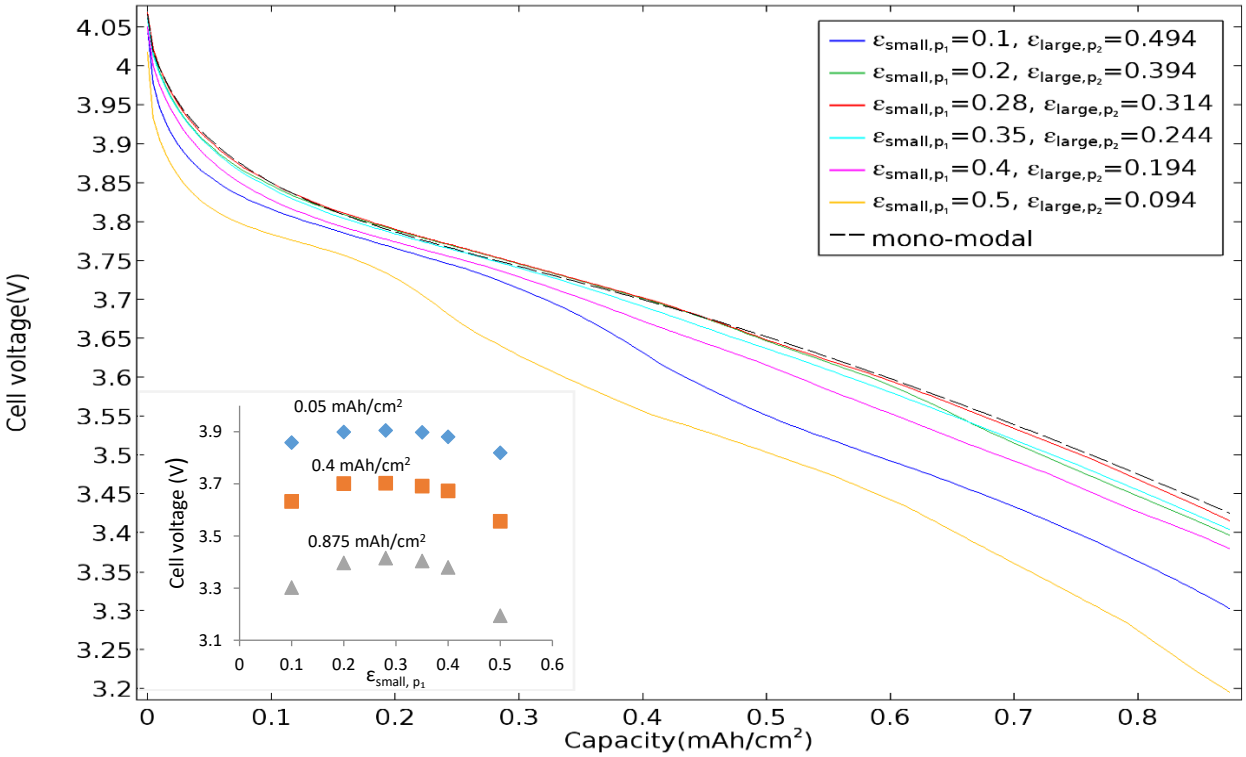

Figure 4.7: Cell voltage versus capacity during discharge for different volume fractions of particles in the positive electrode. Inset: Cell voltage plotted against volume fraction of small particles at selected capacities

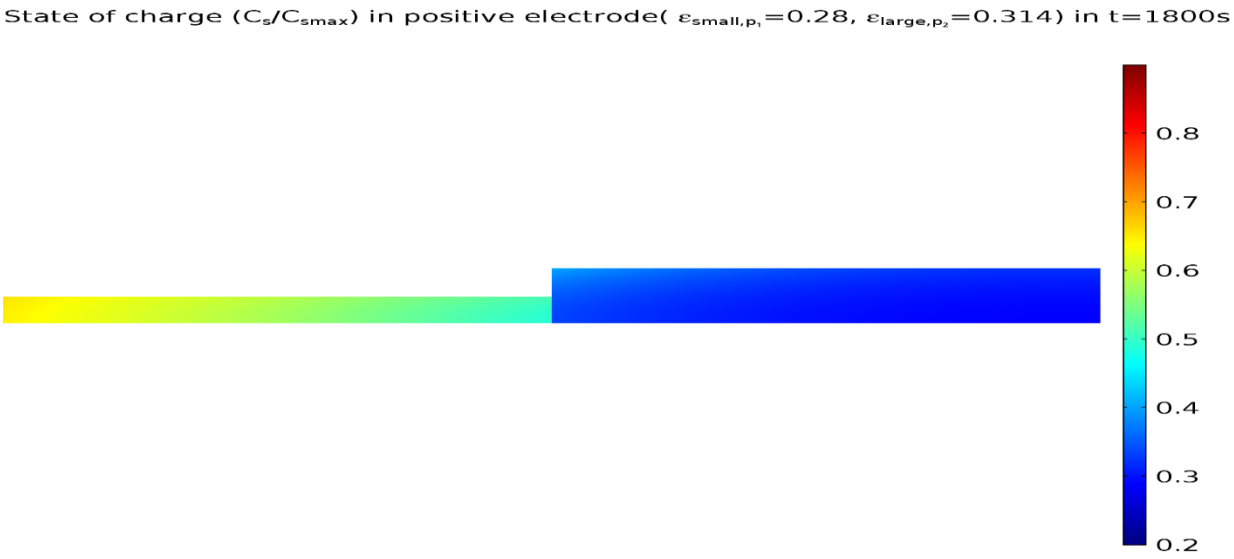

Figure 4.8: SOC distribution in the positive electrode at the end of discharge (t=1800s)

4.3.2 The thickness effect of the two layers on cell performance

The thickness of the two layers was assumed to be the same (a = 2) in the previous section. In this section, the thickness was considered a variable parameter and its effect was analyzed on the cell performance. The larger and smaller particles were assumed to be located near the separator and the current collector, respectively, according to first state of the positive electrode configuration. The ratio of the thickness (a) and ε_{large,p_1} were considered as two variable parameters, while ε_{small,p_2} and the total thickness were kept constant ($\varepsilon_{small,p_2} = 0.35$ and $L_{tot} = 174\ \mu$m). The values of $\varepsilon_{large,p1}$ were determined by Eq. (4.1). Figure 4.9 shows the effect of a variable thickness of the two layers in the positive electrode on the cell voltage-capacity curve during discharge. The optimized value was achieved for a range of a = 1.5 to a = 2, resulting in a larger thickness of the layer composed of smaller particles. In addition, the results indicated that an increase in the thickness of this layer (a = 1.2) led to a decrease in cell voltage at the end of discharge. However, the weak effect of thickness of two layers was observed on cell voltage.

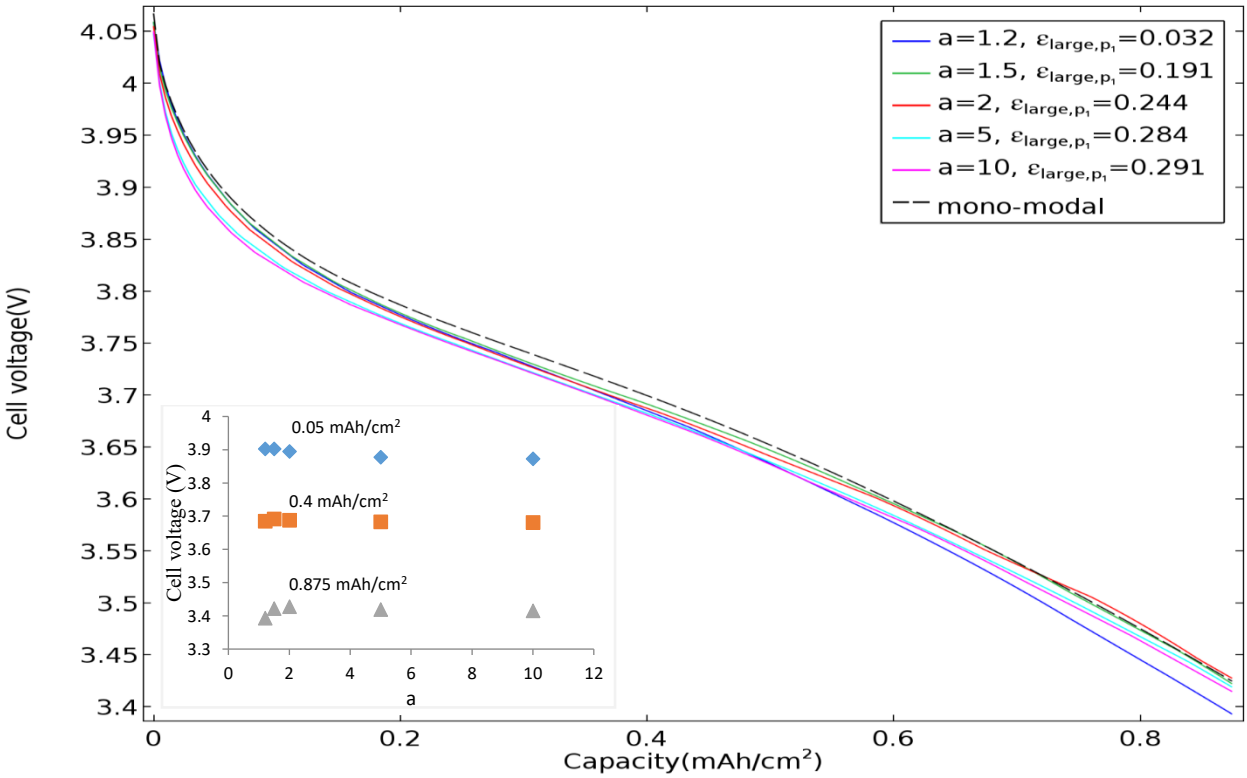

Figure 4.9: Cell voltage versus capacity during discharge for different thickness ratios (a). Inset: Cell voltage plotted against thickness ratio (a) at selected capacities

In Figure 4.10, the contribution from polarization for each transport mechanism is shown as a bar chart at t=100s (start of discharge) and t=1800s (end of discharge) for 3 different thickness ratios (a = 1.2, 1.5 and 10).

Since at the start of discharge, there are more electrolyte next to the separator and lower resistance compared to the back of the electrode, the driving force for mass and charge transfer is

larger. Since for $a = 1.2$, the thickness of the first layer composed of larger particles (the layer next to the separator) was much less than the second layer consisting of smaller particles (the layer next to the current collector), the amount of active material existing in this layer was lower than in the second layer. In spite of the smaller amount of active material, the utilization of active material in the first layer increased because more electrolyte reached the reaction zone and facilitated the reaction kinetics. In fact, most of the polarization in the positive electrode was correlated to the second layer for $a = 1.2$. By increasing the thickness ratio ($a = 1.5$ and $a = 10$), the polarization of the second layer decreased while it increased in the first layer due to the larger thickness and higher resistivity of the first layer. At t=1800s (end of discharge), the intercalation of particles near the current collector was important. Since the second layer of the positive electrode (thickness ratio of $a = 1.2$) had the greater thickness and larger amount of active materials, the mass and charge transport limitations produced higher polarization than for the other cases.

4.4 Conclusion

A P2D model used in our previous work (Chapter 3) [61] was expanded to study the effect of particles position in terms of distance from the separator and current collector in a positive electrode composed of a bi-modal particle size distribution. It was assumed that the positive electrode consisted of two layers: the first layer near the separator and the second layer near the current collector.

The same thickness for each layer was considered initially, with the larger and smaller particles located in the first and second layer, respectively. This assumption resulted in an optimal volume fraction distribution ($\varepsilon_{large,p_1} = 0.244, \varepsilon_{small,p_2} = 0.35$) in which the total polarization of the cell was the lowest. When the location of particles was inverted, a new optimal volume fraction distribution was obtained ($\varepsilon_{small,p_1} = 0.28, \varepsilon_{large,p_2} = 0.314$). The results indicated that for a positive electrode consisting of a bi-modal particle size distribution regardless to the size of particles, the volume fraction of particles near the separator should be less than that of particles near the current collector. In this situation, the higher electrolyte concentration in the reaction zone at the back of the electrode facilitates the Li intercalation reactions, as well as decreases the potential and concentration drops in the electrolyte and produces a more uniform SOC distribution in the solid phase. The analyses indicated that an optimal volume fraction distribution of particles is essential to improve cell performance.

The effect of the thickness of each layer of the positive electrode on cell performance was investigated. It was concluded that the minimum total polarization and highest cell voltage were obtained by increasing the thickness of the layer with smaller particles to an optimal value between $a = 1.5$ and $a = 2$. Increasing or decreasing the thickness of this layer beyond its specific value led to heterogeneities in reaction kinetics, solid and solution phase concentration distributions and potential distributions between two layers that resulted in a higher total cell polarization.

The combination of two different electroactive materials in the positive electrode of a Li-ion battery might be of interest for improving the battery power density [68], [69], and a model should be developed for a blended positive electrode.

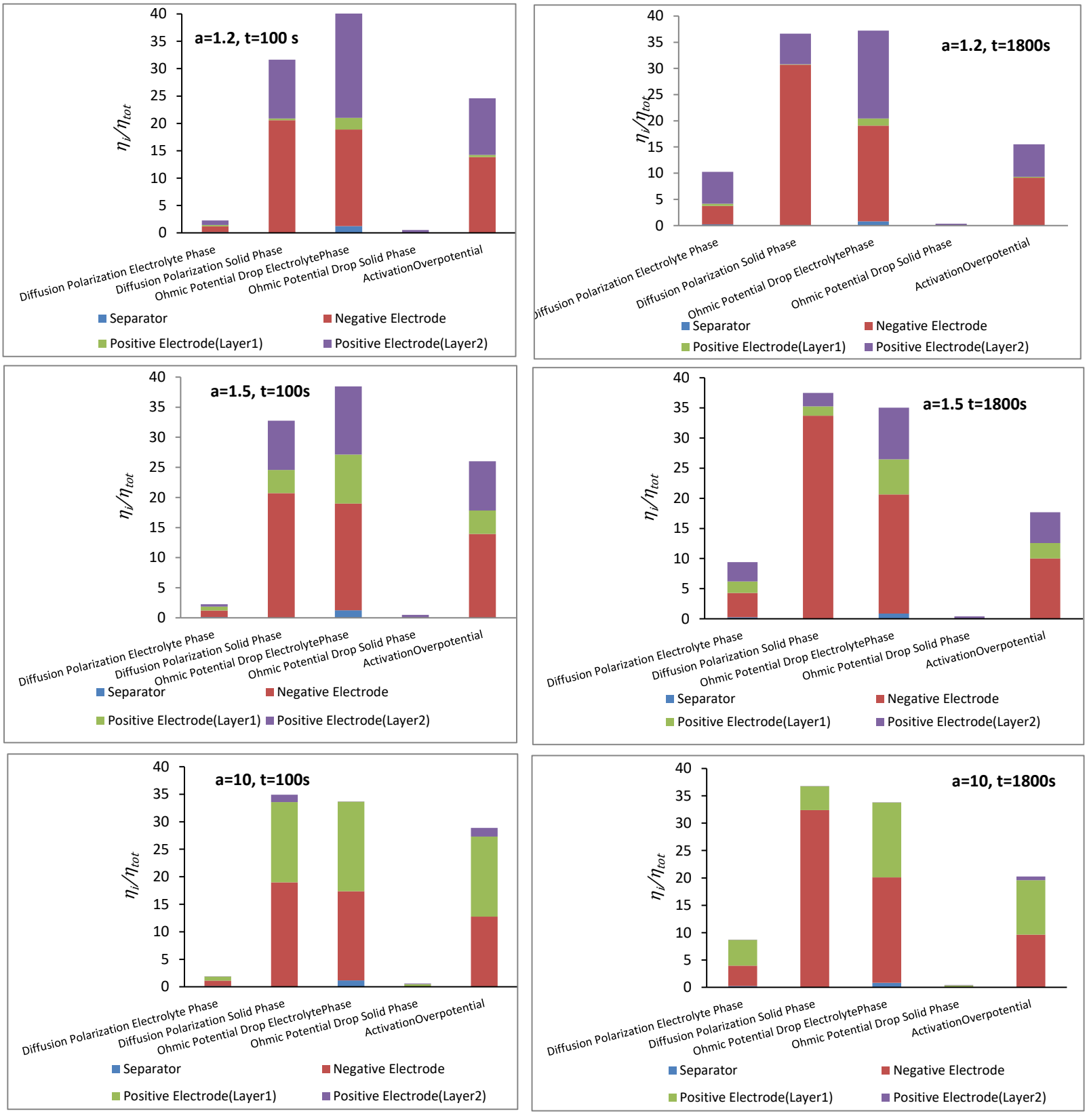

Figure 4.10: A bar chart of the ratio of polarization of each transport mechanism to the total polarization of the cell for different thickness ratios in t=100s and t=1800s

4.5 Acknowledgments

The authors would like to thank Hydro-Québec and the Natural Sciences and Engineering Council of Canada (NSERC) for their financial support.

CHAPITRE 5

Modélisation et simulation d'une cellule Graphite-LiFePO4 commerciale dans une gamme complète de taux de décharge (C-rates)

Titre original: Modeling and simulation of a commercial Graphite-LiFePO4 cell in a full range of C-rates

Auteurs et affiliation:

- **Sara Taslimi Taleghani**: étudiante au doctorat, Université de Sherbrooke, Faculté de génie, Département de génie chimique et de génie biotechnologique.
- **Bernard Marcos:** professeur, Université de Sherbrooke, Faculté de génie, Département de génie chimique et de génie biotechnologique.
- **Gaétan Lantagne:** Institut de recherche d' Hydro-Québec (IREQ), Varennes, QC, J3X 1S1, Canada

Date d'acceptation: 18 juillet 2018

État de l'acceptation: publié

Référence: Journal of Applied Electrochemistry, https://doi.org/10.1007/s10800-018-1239-6

Résumé

Contenu : Cet article présente un modèle pseudo bidimensionnel (P2D) qui décrit le comportement électrochimique d'une cellule cylindrique commerciale 18650 composée d'électrodes graphite et LiFePO4 (LFP). Les simulations ont été réalisées avec le logiciel COMSOL MULTIPHYSICS 5.2. Le modèle a été validé avec des données expérimentales fournies par Hydro-Québec dans une gamme complète de taux de décharge (courants). Le modèle de mosaïque utilisé est basé sur un rayon de particules dépendant du taux de décharge dans les électrodes positives et négatives. La cinétique de la réaction et la diffusion dans la phase solide ont été reconnues comme facteurs limitant la performance de la cellule dans la zone du plateau et dans la zone de pente raide à la fin de la décharge, de la courbe voltage-capacité de la cellule. Puisque la polarisation de diffusion dans une phase solide a joué un rôle important dans la zone de pente raide de la courbe voltage-capacité, le modèle considère un coefficient de diffusion dépendant de la concentration dans l'électrode positive LFP. Basé sur le fait que la surtension d'activation était une polarisation majeure dans la zone du plateau de la courbe voltage-capacité, une résistance de contact sur la surface des particules a été prédite. Cette résistance de contact à la surface des matériaux actifs dans l'électrode positive décrit bien la faible conductivité électronique dans le LFP. En outre, on a observé une bonne concordance entre les résultats simulés et les données expérimentales de décharge pour une gamme complète de taux C.

Résultats : L'étude présentée a mis en évidence les principaux mécanismes de transport contrôlant la performance de la cellule pendant la décharge. En conséquence, la surtension d'activation et la polarisation de diffusion en phase solide ont respectivement limité la performance de la cellule dans la zone du plateau et la zone de pente raide à la fin de la décharge. Les résultats indiquent qu'un coefficient de diffusion dépendant de la concentration et une résistance de contact sur la surface de l'électrode positive peuvent bien décrire les caractéristiques de la limitation du transport de masse et de la faible conductivité électronique dans la structure du LFP.

Contribution au document : Dans l'étude présentée, le comportement électrochimique d'une cellule cylindrique commerciale 18650 composée d'électrodes graphite et $LiFePO_4$ (LFP) a été décrit en utilisant un modèle pseudo bidimensionnel (P2D) en combinaison avec un modèle mosaïque dans une gamme complète de taux C. La nouveauté de ce travail est de reconnaître les principales polarisations qui limitent la performance de la cellule pendant la décharge et de développer un modèle pour décrire les caractéristiques spécifiques des électrodes LFP basées sur ces polarisations.

Abstract

A pseudo two-dimensional model (P2D) was presented to describe the electrochemical behaviour of a commercial 18650 cylindrical cell composed of graphite and LiFePO4 (LFP) electrodes. Simulations were conducted by COMSOL MULTIPHYSICS 5.2. The model validation was done with experimental data taken from Hydro-Québec for a full range of C-rates (currents). A mosaic model based on a C-rate dependent particle radius in positive and negative electrodes was assumed. The reaction kinetics and diffusion in a solid phase were recognized as cell performance limiting factors in the flat area and in the steep area at the end of discharge of the cell voltage-capacity curve, respectively. Since the diffusion polarization in a solid phase played an important role in the steep area at the end of discharge of the cell voltage-capacity curve, a concentration dependent diffusion coefficient in LFP positive electrode was considered. Based on the fact that activation overpotential was a major polarization in the flat area of the cell voltage-capacity curve in addition to decreasing the particle radius at higher C-rates, a contact resistance between the surface of the particles and the solid matrix was predicted. This contact resistance on the surface of active materials in the positive electrode described the feature of low electronic conductivity in LFP. There was a good agreement between the simulated results with experimental discharge data in a full range of C-rates.

Keywords

Graphite-LFP electrochemical cell, Mosaic model, Activation overpotential, Low electronic conductivity

List of Symbols

a	Specific surface area ($\mathrm{m^2 m^{-3}}$)
c	Concentration of Li ($\mathrm{mol\ m^{-3}}$)
c^0	Initial concentration of lithium ($\mathrm{mol\ m^{-3}}$)
$c_{1,max}$	Maximum concentration of lithium in the solid phase ($\mathrm{mol\ m^{-3}}$)
D	Diffusion coefficient ($\mathrm{m^2 s^{-1}}$)
F	Faraday's constant, 96487 ($\mathrm{C\ mol^{-1}}$)
i	Current density ($\mathrm{A\ m^{-2}}$)
i_0	Exchange current density ($\mathrm{A\ m^{-2}}$)
i_m	Local current density in the porous matrix ($\mathrm{A\ m^{-2}}$)
I_{app}	Applied current density of cell ($\mathrm{A\ m^{-2}}$)
j_m	Pore wall flux of lithium-ions ($\mathrm{mol\ m^{-2}\ s^{-1}}$)
k	Reaction rate constant
l	Thickness (m)
r	Radial coordinate (m)
R	Universal gas constant, 8.314 ($\mathrm{J\ mol^{-1}\ K^{-1}}$)

R_c	Contact resistance ($\Omega\ m^2$)
t	Time (s)
t_+^0	Transference number of species Li^+
T	Absolute temperature (K)
U	Open-circuit potential (V)
x	Spatial coordinate (m)

Greek

α_a, α_c	Anodic and cathodic transfer coefficients
ε	Volume fraction or porosity of a phase
η	Overpotential (V)
κ	Ionic conductivity of electrolyte ($S\ m^{-1}$)
σ	Electronic conductivity of the solid phase ($S\ m^{-1}$)
Φ	Electrical potential (V)

Subscripts

ave	Average
eff	Effective value of transport property in porous medium
n	Negative electrode
p	Positive electrode
s	Separator
sur	Surface
1	Solid phase
2	Solution phase

5.1 Introduction

Today, lithium-ion batteries as alternatives to fossil fuels are extensively developed in the automobile industry to improve environmental impacts by decreasing the emission of carbon dioxide [70]. Battery management systems (BMSs) are essential to control and monitor all functions involved in large-scale batteries used in electrified vehicles to maintain their safety and reliability [71]. The distinct features of such batteries, including higher energy and power densities along with cycle durability, have turned them into high energy storage sources [53], [72]. Graphite is used as a common negative electrode material in lithium-ion batteries because of its high electrical conductivity and thermal stability. LFP in comparison with other layered transition metal oxides ($LiCoO_2$ and $LiMn_2O_4$) has been recognized as a promising cathode material due to its specific characteristics [73]. Low cost, safety, non-toxicity, specific capacity, and high stability are distinct features of this material. However, LFP as a phase transformation material has a low electronic conductivity as well as a limitation of mass transport of Li in its

crystal structure which affect its electrochemical performance. Due to these specific features, modeling the behaviour of such electrodes is complicated.

In recent decades, many researchers focused on developing a mathematical model to describe the voltage behaviour of LFP batteries and dynamics of Li intercalation into LFP structure [74]–[80]. First, a shrinking-core model in combination with a porous electrode model was introduced by Srinivasan and Newman [81] to depict the two phase nature of LFP. Srinivasan and Newman [81] just assumed the diffusion of Li through the shell (Li rich phase) that surrounds the core (Li poor phase) and used a mass balance to describe the movement of the phase boundary. Phase transformation was controlled by mass transport in the Li rich phase while phase boundary mobility was considered to be very fast. The shrinking-core model of Srinivasan and Newman [81] was developed by other researchers. Wang et al. [82] considered a core-shell model in which the discharge process was controlled by either diffusion in the Li rich phase or phase boundary mobility or both diffusion and phase boundary mobility. However, diffusion in the Li poor phase was not included in their model. Kasavajjula et al. [83] modified previous models by adding diffusion in the Li poor phase. Using these shrinking-core models is not applicable for complicated charge-discharge processes because the modeling of multiple phase boundaries is very complex and computationally demanding. As an alternative to the shrinking core model, Thorat [84] used a concentration dependent diffusion coefficient in solid phase, referred to a phase change diffusivity, to consider the two phase behavior of LFP. However, this model over-predicted solid phase transport resistance and could not predict the reality of two phase behaviour of LFP. A single particle model was used by Delacourt and Safari [85] to model the onset of charge/discharge curves of a Li-LFP cell. There was a good agreement between the onset of experimental and modeling charge/discharge curves by considering the correlation between particle radius and current density based on a mosaic model [86]. Safari and Delacourt [87] developed a model for Li intercalation/deintercalation in a LFP electrode based on a resistive reactant model inspired by Thomas model [88]. In fact, they considered that the LFP electrode was composed of multiple particles of the same size but with different connectivities to the electrode conductive matrix. Since this model did not embed any features of a porous electrode model, it was only applicable for lower C-rates. Farkhondeh et al. [89] did a comparison between two models of variable solid-state diffusivity (VSSD) and resistive reactant (RR) to describe the Li intercalation/deintercalation process for the LFP electrode in a full range of current densities. They determined that the role of the particle size distribution in the LFP electrode was of significant importance in determining rate capability of this electrode. Maheshwari et al. [90] developed an electrochemical-thermal model for a graphite-LFP based pouch cell. Their model was based on the mosaic model or the current dependent radius based model [86]. They indicated that this approach is equivalent to using a current dependent diffusion coefficient and can be a representative of particle size distribution in the electrode. Farkhondeh et al. [91] described the bi-stable nature of phase change material of LFP by using a single mesoscopic model. They discretized the total active material domain of LFP into meso-scale units with the non-monotonic open circuit potential and insertion/de-insertion resistances among them. The model signified the importance of unit to unit interactions in LFP and described the specific features of this material. Recently, they combined this model with the porous electrode theory [92]. Their results showed a good agreement between experimental data and simulated results during discharge process of a Li-LFP cell at various operating conditions. However, this model is computationally very expensive.

The presented model describes the behavior of a commercial 18650 cylindrical Graphite-LFP cell during discharge process. The features of a porous electrode model were embedded in a pseudo two-dimensional model (P2D). So, it is applicable for higher C-rates as well as lower C-rates. The novelty of this work is recognizing the major polarizations or potential losses inside the cell as main limiting factors of the cell performance and developing a model to describe specific features of LFP electrode based on these polarizations. In fact, the goal of this study is to develop an electrochemical model for a commercial cylindrical Graphite-LFP cell to explain the main transport mechanisms controlling the cell performance during discharge process. To our knowledge, such model that describes comprehensively the transport phenomena occurring inside the Graphite-LFP cell and finds the transport limitations by remarking the major polarizations in each part of cell has not been reported in the previous literature.

Firstly, in the simulation section, a description of the model development, the governing equations and the numerical method to solve them were indicated. Then in the results and discussion section, the portion of each transport process in the total cell potential loss was calculated during discharge and the cell performance limiting factor was determined. In the next step, according to the transport mechanism controlling the cell performance during the different stages of discharge, the model was completed and the results were represented. Finally, the conclusions of this modeling and the future works were stated in the last section.

5.2 Simulation

5.2.1 Model Development

Since the transport limitations at higher currents are significant, a P2D model is proposed. The P2D model considers mass and charge transport in the electrolyte and solid phases, as well as the reaction kinetics in the electrolyte-solid interface. First, Doyle et al. [19] developed a P2D model based on the principles of transport phenomena, electrochemistry and thermodynamics. The concentration and potential in the electrolyte, separator and solid phase were found by solving coupled nonlinear partial differential equations (PDEs). A summary of governing equations has been presented in Table 5.1.

The presented cell consisted of a negative current collector (Cu), negative porous electrode (Li_xC_6), separator, positive porous electrode (LFP) and positive current collector (Al). The electrolyte was composed of $LiPF_6$ salt in a liquid mixture of ethylene carbonate and dimethyl carbonate. Table 5.2 shows all structural and physical parameters used in the model. A scheme of a P2D model is illustrated in Figure 5.1.

Since a particle size distribution was not considered in our model, it was imperative to use a mosaic model [86]. Based on a mosaic model, there is an inverse relationship between the particle radius and the C-rate.

Most battery models considered a spherical geometry for active materials. According to a TEM image of LFP active materials illustrated by Thorat [84], particles had different shapes and were not perfectly spherical. In this study, cylindrical active material particles were assumed.

Table 5.1: Governing equations and boundary conditions for a positive electrode, a negative electrode and a separator in a pseudo two-dimensional model (x and r)

Governing equations	**Boundary conditions**		
	Positive electrode	**Negative electrode**	**Separator**
Mass balance in the electrolyte for a binary salt concentrated electrolyte $\varepsilon_m \frac{\partial c_2}{\partial t} = D_{eff,m} \frac{\partial^2 c_2}{\partial x^2} + a_m (1 - t_+^0) j_m$ Initial condition $c_2\|_{t=0} = c_0$ $m = p \; or \; n$ or s **Hypotheses** Solvent velocity equals to zero Constant transport properties integrating non-ideality effect Constant porosity Structural properties-porosity and tortuosity-integrated in $D_{eff,m}$	$-D_{eff,p} \frac{\partial c_2}{\partial x}\Big\|_{x=l_n+l_s+l_p} = 0$ $c_2\|_{x=l_n+l_s,-} = c_2\|_{x=l_n+l_s,+}$	$-D_{eff,n} \frac{\partial c_2}{\partial x}\Big\|_{x=0} = 0$ $-D_{eff,n} \frac{\partial c_2}{\partial x}\Big\|_{x=l_n,-} = -D_{eff,s} \frac{\partial c_2}{\partial x}\Big\|_{x=l_n,+}$	$c_2\|_{x=l_{n,-}} = c_2\|_{x=l_{n,+}}$ $-D_{eff,s} \frac{\partial c_2}{\partial x}\Big\|_{x=l_n+l_s,-} = -D_{eff,p} \frac{\partial c_2}{\partial x}\Big\|_{x=l_n+l_s,+}$
Potential distribution in solution $\nabla(-\kappa_{eff,m} \frac{\partial \varphi_2}{\partial x} + \frac{2\kappa_{eff,m} RT}{F}(1 - t_+^0) \frac{\partial \ln c_2}{\partial x}) = a_m F j_m$ **Hypotheses** Structural properties-porosity and tortuosity-integrated in $\kappa_{eff,m}$ No reaction in the separator	$i_2\|_{x=l_n+l_s+l_p} = 0$ $\varphi_2\|_{x=l_n+l_s,-} = \varphi_2\|_{x=l_n+l_s,+}$	$i_2\|_{x=0} = 0$ $i_2\|_{x=l_n,-} = i_2\|_{x=l_n,+}$	$\varphi_2\|_{x=l_{n,-}} = \varphi_2\|_{x=l_{n,+}}$ $i_2\|_{x=l_n+l_s,-} = i_2\|_{x=l_n+l_s,+}$
Potentiel distribution in matrix/solid phase $\sigma_{eff,m} \frac{\partial^2 \varphi_1}{\partial x^2} = a_m F j_m$ **Hypotheses** Structural properties-porosity and tortuosity-integrated in $\sigma_{eff,m}$	$i_1\|_{x=l_n+l_s} = 0$ $\frac{\partial \varphi_1}{\partial x}\Big\|_{x=l_n+l_s+l_p} = -\frac{I_{app}}{\sigma_{eff,p}}$	$\varphi_1\|_{x=0} = 0$ $i_1\|_{x=l_n} = 0$	
Mass balance-solid-state diffusion only- in the matrix/solid phase in cylindrical coordinates $\frac{\partial c_1}{\partial t} = \frac{1}{r} \frac{\partial}{\partial r}\left(D_m r \frac{\partial c_1}{\partial r}\right)$ Initial condition $c_1\|_{t=0} = c_1^0$	$\frac{\partial c_1}{\partial r}\Big\|_{r=0} = 0 \quad and \quad -D_m \frac{\partial c_1}{\partial r}\Big\|_{r=R_m} = j_m$		
Reaction rate at the surface of particles (Butler-Volmer equation)			
$i_m = i_0\left(\exp\left(\frac{\alpha_a F \eta_{sur}}{RT}\right) - \exp\left(-\frac{\alpha_c F \eta_{sur}}{RT}\right)\right)$ $i_0 = F \; k \; c_{1,max} (c_2)^{\alpha_a}$ $\eta_{sur} = \Phi_1 - \Phi_2 - U(SOC_{sur})$			
The relation between the reaction rate and the pore wall flux			
$i_m = F j_m$			

Table 5.2: Model Parameters

Parameter			Symbol	Value
Temperature (°C)			T	25
Thickness (μm)	Positive electrode		l_p	64
	Negative electrode		l_n	43
	Separator		l_s	25
Cross section area(m^2)			A_{cell}	0.097
Solid phase volume fraction	Positive electrode		$\varepsilon_{1,p}$	0.339
	Negative electrode		$\varepsilon_{1,n}$	0.45
Separator porosity			ε_s	0.55
Initial salt concentration in the solution (mol m^{-3})			c_2^0	1000
Maximum salt concentration in the solid phase (mol m^{-3})	Positive electrode		$c_{1,p}^0$	22806 [89]
	Negative electrode		$c_{1,n}^0$	31450
Diffusion coefficient of Li in negative electrode (m^2s^{-1})			D_n	$4.8*10^{-15}$
Diffusion coefficient of Li ion in the electrolyte phase (m^2s^{-1})			D_s	$5*10^{-10}$
Transference number			t_+^0	0.363
Ionic conductivity of electrolyte (S m^{-1})			κ	1.3 [89]
Effective electronic conductivity of positive electrode (S m^{-1})			$\sigma_{eff,p}$	6.75 [93]
Reaction rate constant $(mol\ m^{-2}s^{-1}(mol\ m^{-3})^{-1.5})$		Positive electrode	k_p	$4.5*10^{-12}$
		Negative electrode	k_n	$4.2*10^{-12}$
Initial SOC		Positive electrode	SOC_p	0.035 [94]
		Negative electrode	SOC_n	0.811 [94]

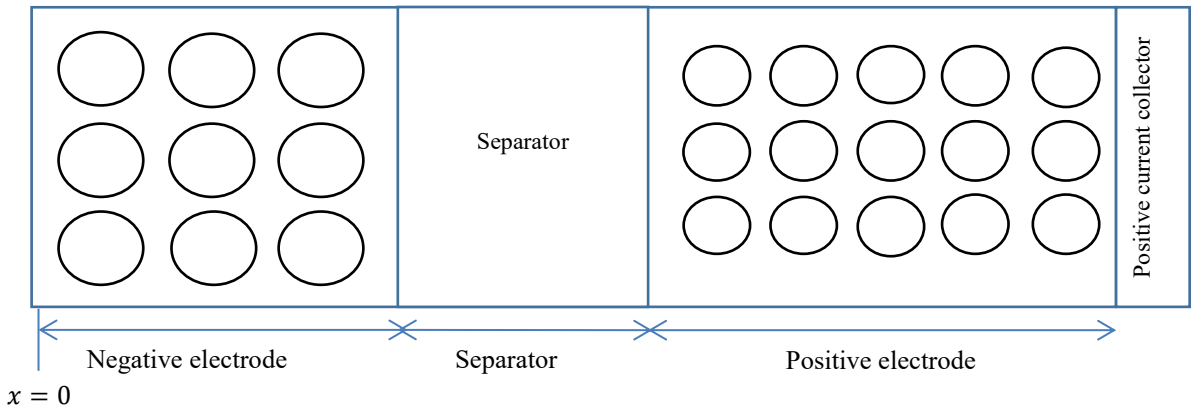

Figure 5.1: An illustration of a P2D model

5.2.2 Numerical Solution

In this paper, the simulations were conducted by COMSOL Multiphysics 5.2 software. To solve the equations, a direct solver of MUMPS (Multifrontal Massively Parallel sparse direct Solver) was utilized. The relative and absolute tolerances were equal to 0.001. Automatically, a physics-controlled mesh was applied to the geometry. The solution time for all simulations was less than 1 minute. The simulated model results are discussed below.

5.3 Results and Discussion

A developed model was used to analyse the experimental data related to a cylindrical cell of Graphite-LFP taken from Hydro-Québec for a full range of C-rates (low and high C-rates). First, simulations were conducted for lower C-rates from C/8 to 1C. A 1C-rate is a current that discharges the cell in 1 hour (here it is equal to 1.05 A). As observed in Figure 5.2, there were three distinct areas in the cell voltage-capacity curve; an early stage of discharge, a flat area and an area with a steep slope at the end of discharge. To find the rate determining step (or cell performance limiting factor), the portion of each polarization related to the total polarization of cell (the total potential loss) was presented in Figure 5.3 for 1C or current of 1.05 A at t=2000 s and t=3500 s as a bar chart. These times corresponded to the polarizations in the flat area and in the end of discharge area, respectively. Table 5.3 shows the required formulations to calculate these polarizations [65].

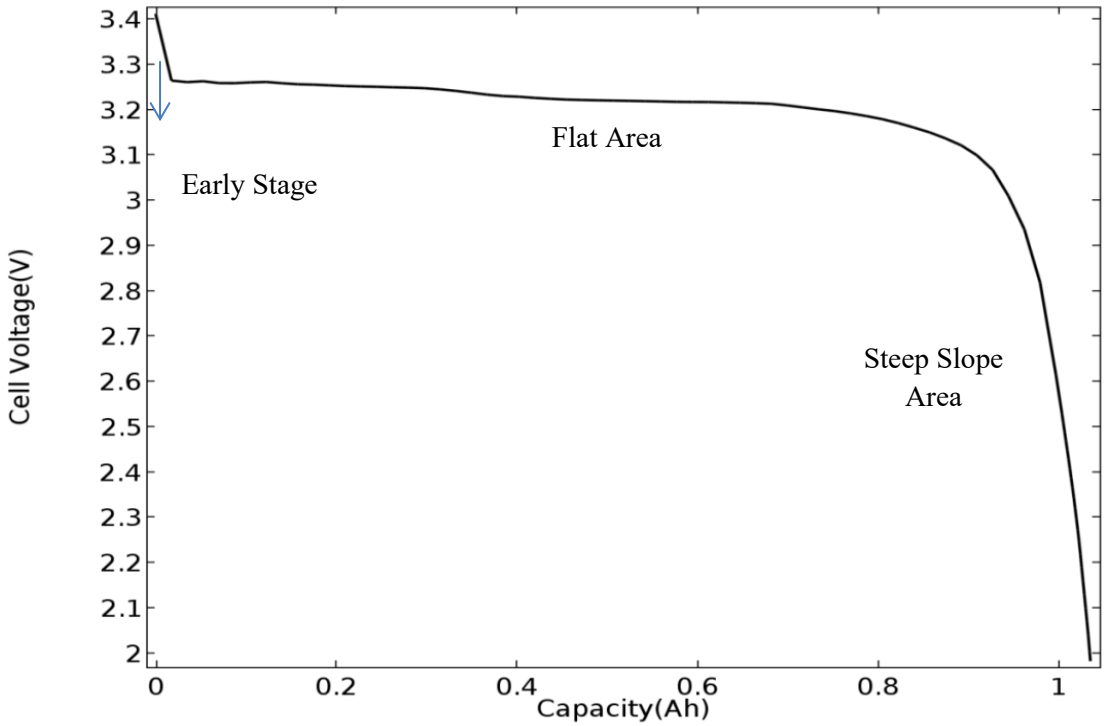

Figure 5.2: An illustration of three distinct areas in cell voltage-capacity curve during discharge process

Table 5.3: Polarization calculations [65]

Diffusion polarization electrolyte phase	$-\frac{1}{\int_0^l a i_m \, dx}\int_0^l \frac{2RT}{C_2 F}(1-t_+^0)\frac{\partial C_2}{\partial x} i_2 dx$
Diffusion polarization solid phase	$\frac{1}{\int_0^l a i_m \, dx}\int_0^l a i_m \, (U_{sur}-U_{ave})dx$
Ohmic potential drop electrolyte phase	$\frac{1}{\int_0^l a i_m \, dx}\int_0^l \frac{i_2^2}{\kappa_{eff}} dx$
Ohmic potential drop solid phase	$\frac{1}{\int_0^l a i_m \, dx}\int_0^l \frac{i_1^2}{\sigma_{eff}}$
Activation overpotential	$\frac{1}{\int_0^l a i_m \, dx}\int_0^l a i_m \, (\Phi_1-\Phi_2-U_{sur})dx$

As presented in Figure 5.3, in t=2000s or in the flat area of cell voltage-capacity curve, the major polarizations are ascribed to the activation overpotentials while in t=3500s or in the steep area at the end of discharge area, the diffusion limitation in solid phase is recognized as a rate determining step.

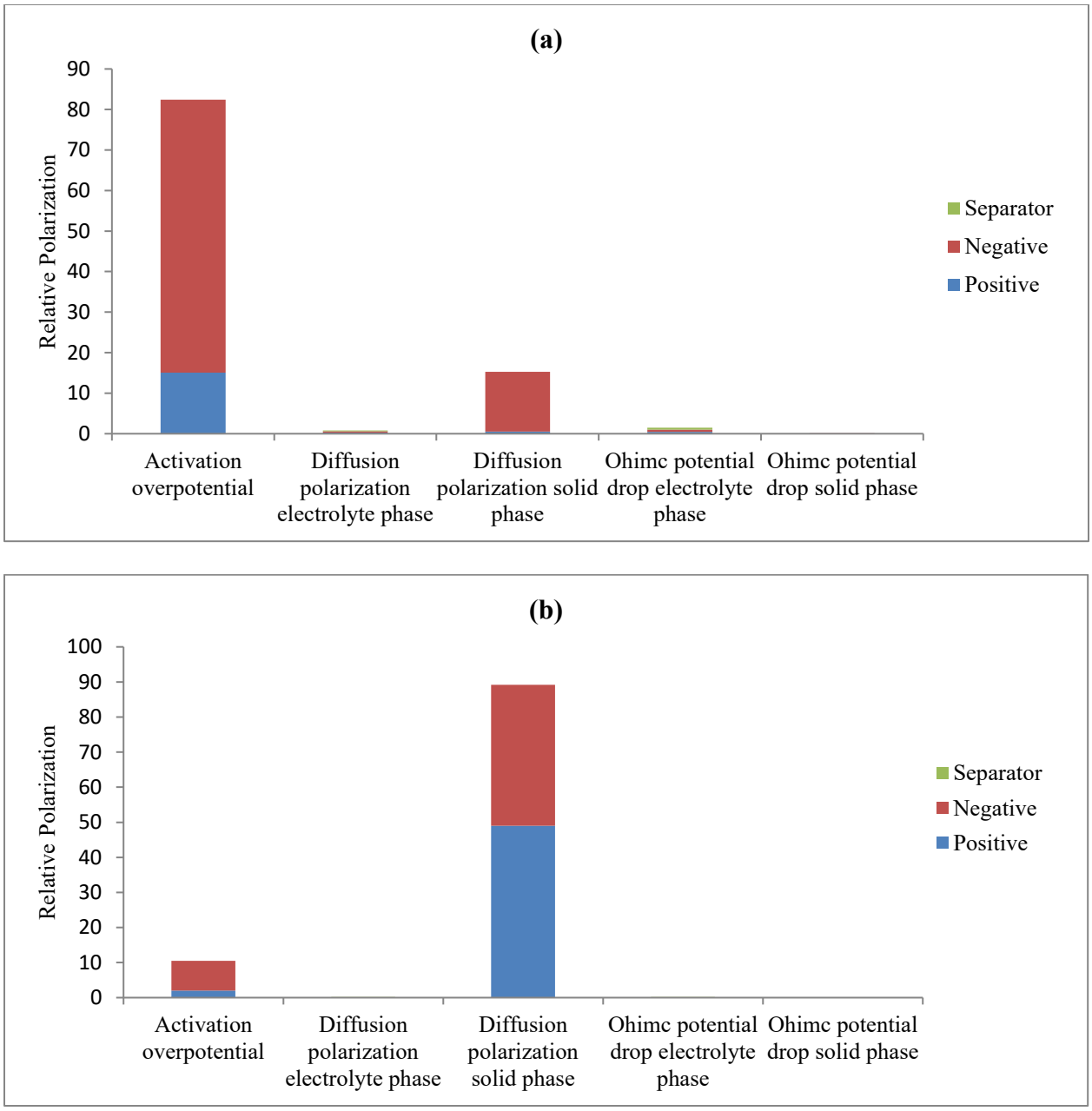

Figure 5.3: The relative polarization distribution for 1C (i=1.05 A) at (a) t=2000s (b) t=3500s

Figure 5.4 shows a comparison of the discharge curves of cell voltage versus capacity of constant diffusion coefficient ($D = 1.9 * 10^{-16} m^2 s^{-1}$) and variable diffusion coefficient models with experimental curves. By considering a constant diffusion coefficient model, there was a good fit between discharge curves and experimental discharge data for all C-rates lower than 1 in the early stage of discharge and also in the flat area of discharge. However, there were discrepancies in the steep area at the end of discharge. Since the diffusion polarization in the solid phase of a positive electrode limited the cell performance at the end of discharge area (Figure 5.3b), a variable diffusion coefficient was substituted for a constant diffusion coefficient in the positive

electrode. The diffusion coefficient was considered as a polynomial function of surface state of charge (SOC_{sur}) of the active materials in positive electrode.

$$D_p = a({SOC_{sur}}^2) + b(SOC_{sur}) + c \tag{5.1}$$

SOC_{sur} was defined by:

$$SOC_{sur} = \frac{c_{1,sur}}{c_{1,max}} \tag{5.2}$$

The values of a, b and c as adjustable parameters are shown in Table 5.4.

Table 5.4: Adjustable parameters of diffusion coefficient function

a	$146.91 * 10^{-16}$
b	$-286.45 * 10^{-16}$
c	$140.48 * 10^{-16}$

The given diffusion coefficient has an inverse correlation with SOC. Safari and Delacourt used an empirical equation for diffusion coefficient [87]:

$$D = \frac{1.184 * 10^{-18}}{(1 + \bar{y})} \tag{5.3}$$

where $\bar{y} = \frac{\bar{c}_1}{c_{1,max}}$ is the average state of charge. They indicated that the diffusion coefficient of the Li rich phase of LFP is lower compared to that of the Li poor phase. Based on Safari's report [87] and also the fact that SOC on the LFP surface increases by conversion of Li poor phase to Li rich phase during discharge process, the inverse correlation between diffusion coefficient and SOC (Eq. (5.1)) seems to be correct.

As seen in Figure 5.4, there was a good fitting between the simulated discharge curves and the experimental data by considering a SOC-dependent diffusion coefficient and discrepancies existing in the steep area at the end of discharge area between two curves reached a minimum value. The results indicated that the limitation of mass transport in LFP structure can be explained by a concentration-dependent diffusion coefficient. It is worth mentioning that using concentration-dependent transport coefficients in other related fields like fuel cells can be useful to simulate precisely transport limitations [95]–[97].

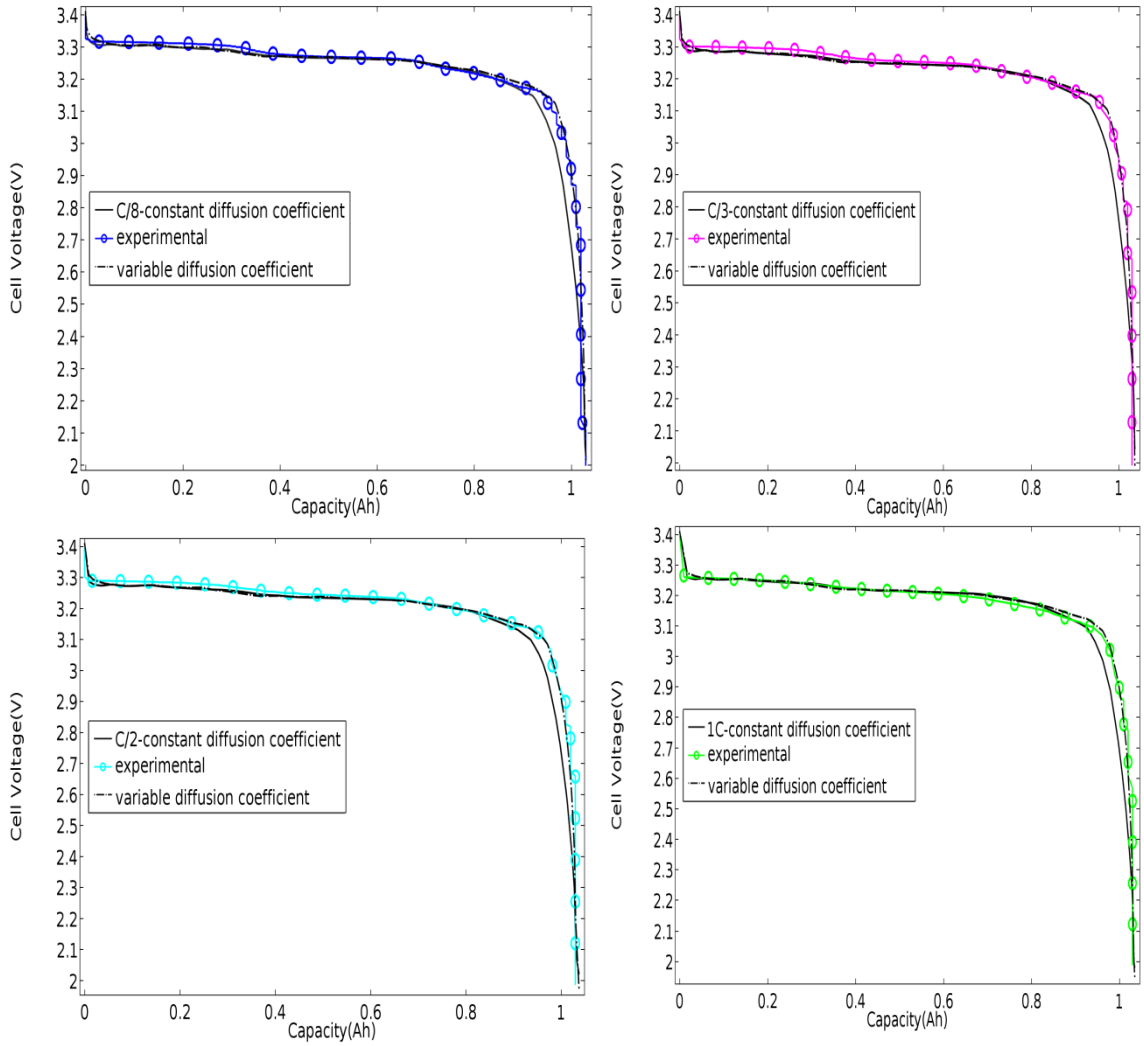

Figure 5.4: A comparison of cell voltage-capacity curves of two models with constant diffusion and variable diffusion coefficients with experimental data at lower C-rates

Figure 5.5 compares the cell voltage-capacity curves of two models without contact resistance ($R_c = 0$) and with contact resistance (R_c) to the experimental data during the discharge process at higher C-rates. The results simulated by the proposed model for lower C-rates were not satisfying for higher C-rates. There was a significant discrepancy between model results and experiments in the flat area of cell voltage curve which was pronounced by increasing the C-rates. In fact, model results showed an overestimated cell voltage compared to the experimental data which indicated an additional cell voltage loss at higher C-rates. As mentioned previously, the activation overpotential was recognized as a major polarization in the flat area of cell voltage-capacity curve. So the additional cell voltage loss was expected to be related to surface reaction kinetics. According to the mosaic model [86], active material particle radius decreases

by increasing the C-rates. Since LFP is a low electronic conductive material, decreasing its active material particle radius was assumed to increase the contact resistance between particle surface and the conductive matrix. This contact resistance decreased the rate of transferring electrons to the surface of particles and therefore increased the activation polarization. Thus, the overpotential used in Butler-Volmer equation should be modified by:

$$\eta_{sur} = \Phi_1 - \Phi_2 - i_m R_c - U(SOC_{sur}) \tag{5.4}$$

Where R_c is a contact resistance between particle surface and the conductive matrix of LFP.

Therefore, a mixed model of variable diffusion coefficient and surface contact resistance was applied for higher C-rates of a discharge process. Simulations were run by considering a particle radius dependent contact resistance on the particle surface of positive electrode. As seen in Figure 5.5, there was a good agreement between simulated results and experiments in the total areas of cell voltage-capacity curve.

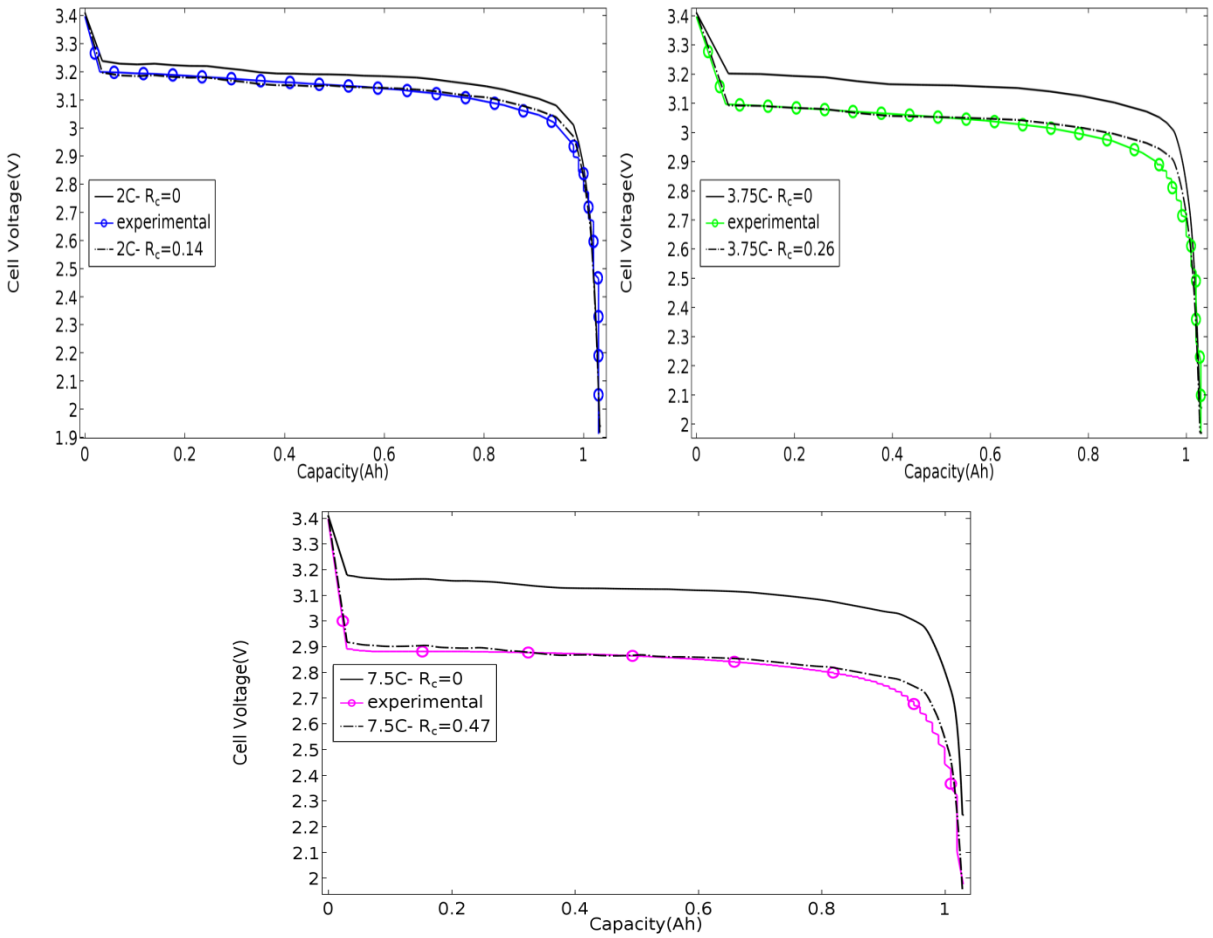

Figure 5.5: A comparison of cell voltage-capacity curves of two models with contact resistance and without contact resistance with experimental data at higher C-rates

Finally, Figure 5.6 illustrates the correlation between radius and C-rates for both electrodes. Based on the mosaic model [86], particle radius at the positive and negative electrodes was assumed to be dependent on the C-rate. Figure 5.6 showed that the particle radius was decreased by increasing the C-rate. This correlation can be explained by the concept that the nucleation of reaction sites (the boundary between Li-rich phase and Li-poor phase) occurs faster at higher C-rates and divides the original domain into smaller diffusion domains. By contrast, the number of formed diffusion domains is lesser at lower current densities. So it is assumed that the size of particles is larger at lower C-rates. Delacourt and Safari [85] described this phenomenon in detail.

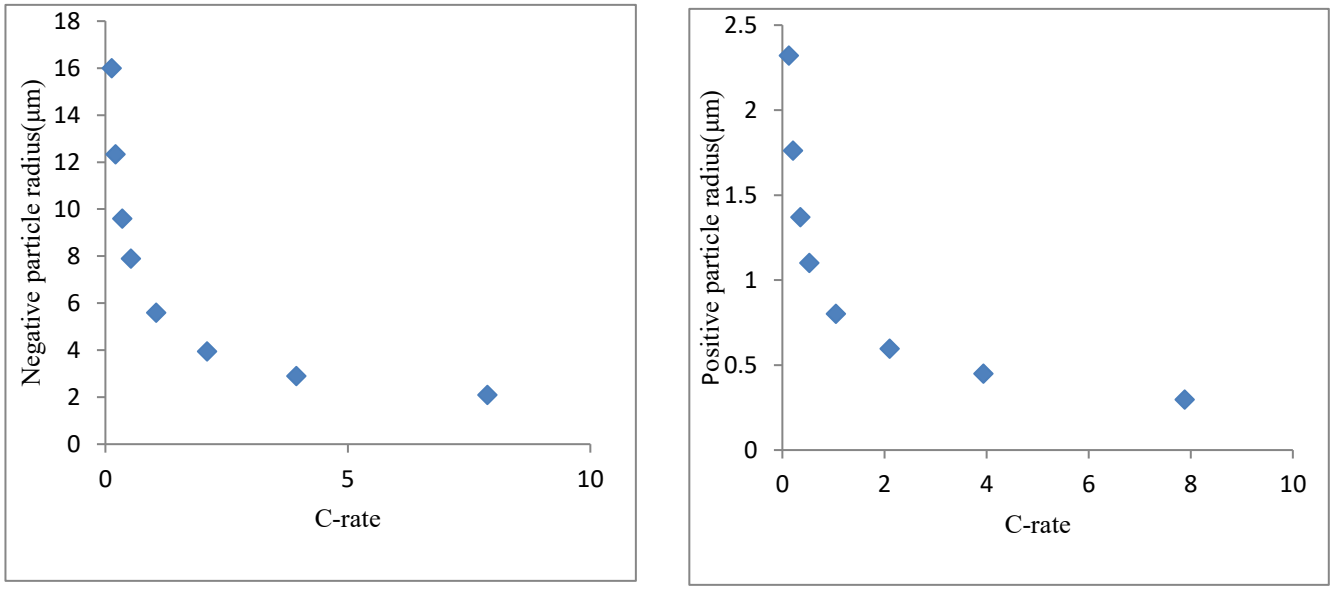

Figure 5.6: The correlation between radius and C-rate for both negative and positive electrodes

5.4 Conclusion

The P2D model of Doyle in combination with a mosaic model [86] was used to describe the transport mechanisms in a commercial 18650 cylindrical graphite-LFP cell. The model was developed to analyse the specific characteristics of LFP in lower and higher C-rates. The described model showed a good agreement with experimental data obtained from Hydro-Québec. Multi regions of cell voltage-capacity curve were explicated during discharge process and major transport mechanisms were recognized. As a result, the activation overpotential and diffusion polarization in solid phase limited the cell performance in the flat area and the steep slope area at the end of discharge, respectively. Comparisons between two models, including constant diffusion coefficient and variable diffusion coefficient, showed that the limitation of mass transport in the LFP structure could be explained by a concentration-dependent diffusion coefficient model. At higher C-rates, the variable diffusion coefficient model failed and could

not explain the cell voltage loss in the flat area of the curve. This cell voltage loss was ascribed to an activation polarization on the particle surface. Thus, a mixed model based on both concentration-dependent diffusion coefficient and contact resistance on the surface of LFP particles was developed at higher C-rates. The results indicated that a contact resistance on the positive electrode surface could elucidate the characteristic of low electronic conductivity of LFP. By increasing the C-rates, the contact resistance increased due to the decrease of the particle radius based on the mosaic model [86].

Safety and life time of batteries are challenges for battery designers. As a future work, the developed model can be applicable for analysing other issues in battery systems such as the thermal management of batteries and degradation mechanisms or capacity fading inside the battery which affect the battery safety and life time. Additionally, transport coefficients can be refined by modifying the correlation between tortuosity and porosity or by including the effect of non-idealities by finding a relationship between activity and concentration similar to that used in ion-exchange membrane of fuel cells [95]–[97].

5.5 Acknowledgments

The authors would like to thank Hydro-Québec and the Natural Sciences and Engineering Council of Canada (NSERC) for their financial support.

CHAPITRE 6

Un modèle électrochimique-thermique pour une cellule cylindrique commerciale de graphite-$LiFePO_4$

Titre original: An electrochemical-thermal model for a commercial cylindrical Graphite-LiFePO4 cell

Auteurs et affiliation:

- **Sara Taslimi Taleghani:** étudiante au doctorat, Université de Sherbrooke, Faculté de génie, Département de génie chimique et de génie biotechnologique.
- **Bernard Marcos:** professeur, Université de Sherbrooke, Faculté de génie, Département de génie chimique et de génie biotechnologique.
- **Gaétan Lantagne:** Institut de recherche d' Hydro-Québec (IREQ), Varennes, QC, J3X 1S1, Canada

Date d'acceptation : à venir

État d'acceptation : en attente de commentaire de partenaire industriel

Résumé

Contenu et Résultats : Un modèle pseudo bidimensionnel (P2D) combiné à un modèle thermique a été développé pour analyser le comportement thermique d'une cellule cylindrique commerciale 18650 de Li-ion pendant la décharge. L'article étudie l'effet des paramètres physico-chimiques dépendant de la température sur le voltage de la cellule et sa température de surface. Des voltages supérieurs et des températures de surface inférieures ont été obtenues avec le modèle en considérant les paramètres dépendant de la température. De plus, l'effet des paramètres dépendant de la température était plus accentué à des taux de décharge plus élevés (courants). Le modèle a été validé avec des données expérimentales fournies par Hydro-Québec pour des taux de décharge élevés. Un bon accord a été obtenu entre les résultats simulés et les données expérimentales. Différentes sources de génération/consommation de chaleur, dont la chaleur entropique, la chaleur de réaction irréversible, la chaleur ohmique et la chaleur produite par la polarisation de diffusion en phase solide ou la chaleur de relaxation, ont été prises en compte dans le modèle. La chaleur générée par la polarisation de diffusion en phase solide a été reconnue comme une source de chaleur majeure à la fin de la décharge, tandis qu'environ 88% de la chaleur totale générée a été attribuée à cette source de chaleur à un taux de 7.5C. De plus, les résultats indiquaient que les températures maximale et minimale ont été rapportées respectivement au centre et à la surface de la cellule.

Contribution au document : Un modèle pseudo bidimensionnel (P2D) couplé à un modèle thermique a été développé pour décrire les comportements électrochimique et thermique d'une cellule cylindrique commerciale 18650 de graphite-LFP pendant la décharge pour des taux de décharge élevés. La contribution de chaque polarisation dans la chaleur totale générée de la cellule a été étudiée. La partie de la chaleur provoquée par le processus de diffusion en phase solide n'a pas été considérée dans la plupart des travaux antérieurs alors que les résultats de cette recherche indiquaient que la chaleur générée par le processus de diffusion en phase solide était une source de chaleur importante à la fin de la décharge.

Abstract

A pseudo two-dimensional model (P2D) combined with a lumped thermal model was developed to analyze the thermal behaviour of a commercial 18650 cylindrical Li-ion cell during discharge. The effect of the temperature dependent physicochemical parameters was studied on cell voltage and cell surface temperature. Higher cell voltages and lower cell surface temperatures were as a result of this dependency. Additionally, the effect of the temperature dependent parameters was more highlighted at higher C-rates (currents). The model was validated with experimental data provided by Hydro-Québec at high discharge rates. There was a good agreement between the simulated results and experimental data. Different heat generation/consumption sources including entropy heat, irreversible reaction heat, ohmic heat and the heat produced by diffusion polarization in solid phase or relaxation heat were considered in the model. The heat generated from the diffusion polarization in solid phase was recognized as a major heat source at the end of discharge in a way that around 0.88 of the total generated heat was ascribed to this heat generation source at 7.5 C-rate. Furthermore, the results indicated that the maximum and minimum temperatures were referred to the center and surface of the cell, respectively.

List of Symbols

a	Specific surface area ($\mathrm{m^2 m^{-3}}$)
c	Concentration of Li ($\mathrm{mol\ m^{-3}}$)
c^0	Initial concentration of lithium ($\mathrm{mol\ m^{-3}}$)
$c_{1,max}$	Maximum concentration of lithium in the solid phase ($\mathrm{mol\ m^{-3}}$)
C_p	Heat Capacity ($\mathrm{J\ kg^{-1} K^{-1}}$)
D	Diffusion coefficient ($\mathrm{m^2 s^{-1}}$)
F	Faraday's constant, 96487 ($\mathrm{C\ mol^{-1}}$)
i	Current density ($\mathrm{A\ m^{-2}}$)
i_0	Exchange current density ($\mathrm{A\ m^{-2}}$)
i_m	Local current density in the porous matrix ($\mathrm{A\ m^{-2}}$)
I_{app}	Applied current density of cell ($\mathrm{A\ m^{-2}}$)
j_m	Pore wall flux of lithium-ions ($\mathrm{mol\ m^{-2}\ s^{-1}}$)
k	Reaction rate constant
l	Thickness (m)
Q	The total generated heat ($\mathrm{W\ m^{-3}}$)
r	Radial coordinate (m)
R	Universal gas constant, 8.314 ($\mathrm{J\ mol^{-1}\ K^{-1}}$)
R_c	Contact resistance ($\Omega\ \mathrm{m^2}$)
t	Time (s)
t_+^0	Transference number of species Li^+

T	Absolute temperature (K)
T_{amb}	Ambient temperature (K)
U	Open-circuit potential (V)
x	Spatial coordinate (m)

Greek

α_a, α_c	Anodic and cathodic transfer coefficients
ε	Volume fraction or porosity of a phase
η	Overpotential (V)
κ	Ionic conductivity of electrolyte (S m^{-1})
λ	Thermal conductivity (W $m^{-1}K^{-1}$)
ρ	Density (kg m^{-3})
σ	Electronic conductivity of the solid phase (S m^{-1})
φ	Electrical potential (V)

Subscripts

eff	Effective value of transport property in porous medium
n	Negative electrode
p	Positive electrode
ref	Reference state
s	Separator
sur	Surface
1	Solid phase
2	Solution phase

6.1 Introduction

Safety and performance are two noticeable factors for battery manufacturers. The battery performance is significantly affected by thermal environment of the inside and the outside of the battery. The battery thermal management is of significant importance because the total generated heat in battery causes a rise in temperature that can lead to a thermal runaway and a decrease in battery performance [98]. Thus, the development of a robust mathematical model that can describe transport mechanisms and thermal behavior of the battery in detail is essential for battery designers.

Most thermal models were the development of Doyle's model [19] by adding an energy balance to his electrochemical model [21], [52], [99]–[103]. Rao and Newman [104] introduced a new method for calculating the total heat generation rate. In this method they considered that the total heat generation rates were obtained from the polarizations or potential losses in different parts of battery. However, they did not consider any effects of heat due to the concentration gradients in

the electrolyte phase and diffusion in solid phase. Guo et al. [105] coupled an energy balance with a modified single particle model in which ohmic potential in solution phase was estimated by a nonlinear resistance. The weakness of this model was neglecting the concentration gradients in the solution phase. Thus it was only applied for low C-rates. Jiang et al. [106] developed a thermal-electrochemical coupling model for Graphite-LFP based Li-ion batteries. Different heat generation/consumption sources including irreversible reaction heat, entropy heat, ohmic heat, contact resistance heat and convective heat released to the ambient were considered in their model. The irreversible reaction heat and the contact resistance heat were recognized as two major thermal sources. A P2D model coupled with a lumped thermal model was developed by Saw et al. [107] to illustrate the temperature distribution across a cylindrical Graphite-LFP cell. They showed that around 80-85% of the total heat generation rate is contributed to the irreversible reaction heat during charge and discharge process. Liu et al. [108] also studied the effect of temperature on Solid-Electrolyte-Interface (SEI) layer formation on the graphite negative electrode surface. Their simulation results indicated that temperature rise increased the SEI layer growth due to accelerating the side reaction kinetics and diffusion.

Most electrochemical-thermal models were not considered the effect of the heat generated by diffusion polarization in solid phase on the total generated heat while it can be important especially in a Graphite-LFP cell. LFP is a promising candidate for the positive electrode of Li-ion batteries due to its high thermal stability, non-toxicity, high capacity and low cost [109]. However, the low electric conductivity and the low diffusivity in its crystal structure can dramatically affect the cell performance. In our previous work [110] (Chapter 5), we showed that diffusion in solid phase was a major limiting factor of a Graphite-LFP cell performance during the end of discharge time. Since each polarization contributes to the heat generation, considering the heat induced by diffusion polarization in the solid phase is vital to understand the cell thermal behavior and can help to design a proper thermal management system. As a novelty of this study, the total generated heat derived by the total polarization of the cell was separated to the heats produced by the internal losses or overpotentials in multi areas of cell and the significance of the overpotential caused by diffusion in solid phase in the total generated heat of the cell was studied. To our knowledge, such work has not been reported in the previous literature.

In the presented study, an electrochemical P2D model was coupled with a thermal model to analyse the temperature distribution across a cylindrical Graphite-LFP cell during discharge. First, a comparison was done between a model considering temperature-dependent physicochemical parameters and the one neglecting this dependency. Then the simulated results were validated with experimental data derived from Hydro-Québec at high discharge rates. Finally, the electro-thermal characteristics of the cell were comprehensively studied and the portion of each polarization in the total generated heat and the dominant heat generation/consumption source were determined.

6.2 Model Development

An electrochemical-thermal model was applied to describe charge, mass and heat transport mechanisms across a commercial 18650 cylindrical Li-ion cell composed of Graphite and LFP during discharge. A cylindrical cell consisted of individual layers wound into a cylinder. Each layer has a micrometer scale in the normal direction to the layer but a centimeter scale in the

sheet direction. A P2D electrochemical model and a two-dimensional axisymmetric thermal model (2D-axisymmetric thermal model) were used to describe the cell electrochemical and the thermal effects, respectively. Figure 6.1 shows a scheme of two models. Since thickness of each layer in a P2D model is small (micrometer scale), a uniform temperature profile was assumed inside the cell. The P2D electrochemical model and 2D-axisymmetric thermal model were coupled to each other by linking the average total generated heat calculated in the P2D model to the energy balance equation in thermal model and by combining the average temperature computed in the thermal model to the electrochemical equations of P2D model. In the following, each model will be described in detail. Table 6.1 shows model parameters in the cell.

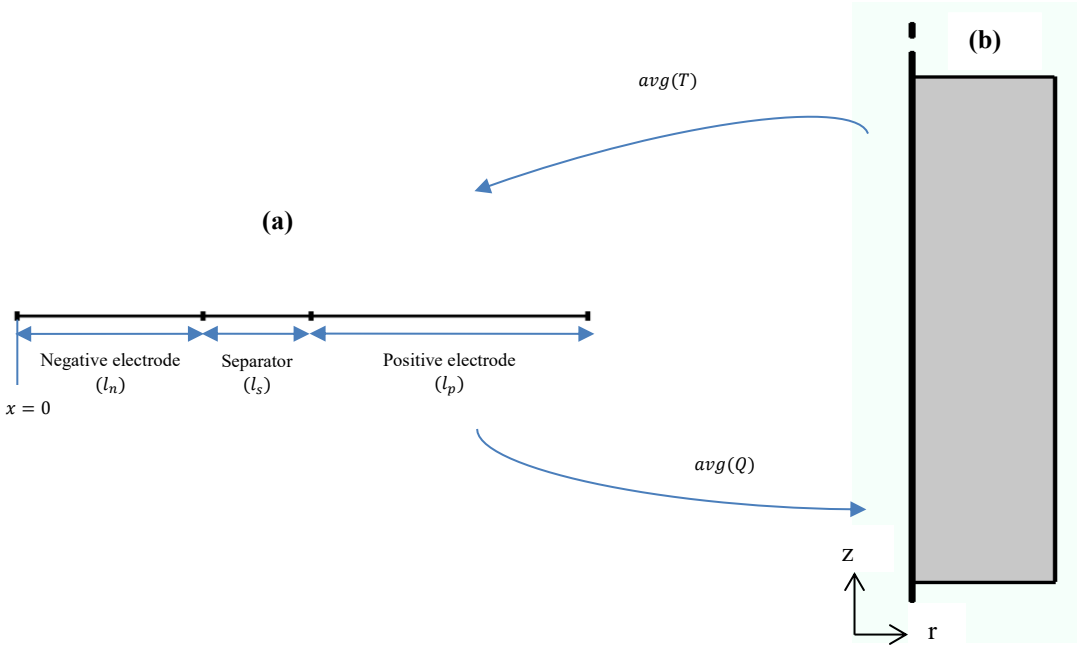

Figure 6.1: A presentation of (a) an electrochemical P2D model (b) a thermal model; and their coupling with the average values of temperature and the total generated heat

6.2.1 Electrochemical P2D model

First, Doyle et al. [19] developed a P2D model based on the various mechanisms including mass and charge transport in the electrolyte and solid phases, as well as the reaction kinetics in the electrolyte-solid interface. Since at higher C-rates transport limitations are noticeable, using the P2D model of Doyle [19] can be beneficial. The cell components were composed of a negative current collector (Cu), negative porous electrode (Li_xC_6), separator, positive porous electrode (LFP) and positive current collector (Al). The electrolyte consisted of $LiPF_6$ salt in a liquid mixture of ethylene carbonate and dimethyl carbonate. A mosaic model [86] based on an inverse relationship between the particle radius and the C-rate was assumed instead of considering a particle size distribution in LFP positive electrode. The governing equations for a P2D model are presented in Table 6.2.

Table 6.1: Model Parameters

Parameter			Symbol	Value
Ambient temperature (°C)			T	25
Thickness (μm)	Positive electrode		l_p	64
	Negative electrode		l_n	43
	Separator		l_s	25
	Positive current collector		$l_{cc,p}$	20
	Negative current collector		$l_{cc,n}$	12
Cross section area(m^2)			A_{cell}	0.097
Cell radius (m)			r_{cell}	$12.9*10^{-3}$
Cell height (m)			h_{cell}	$58.3*10^{-3}$
Cell density (kg m^{-3})			ρ	2903.4
Cell heat capacity (J $kg^{-1}K^{-1}$)			C_p	1105.9
Thermal conductivity in the radial direction (W $m^{-1}K^{-1}$)			λ_r	0.376
Thermal conductivity in the axial direction (W $m^{-1}K^{-1}$)			λ_{axial}	50.26
Heat transfer coefficient (W $m^{-2}K^{-1}$)			h	27
Solid phase volume fraction	Positive electrode		$\varepsilon_{1,p}$	0.339
	Negative electrode		$\varepsilon_{1,n}$	0.45
Separator porosity			ε_s	0.55
Initial salt concentration in the solution (mol m^{-3})			c_2^0	1000
Maximum salt concentration in the solid phase (mol m^{-3})	Positive electrode		$c_{1,p}^0$	22806 [89]
	Negative electrode		$c_{1,n}^0$	31450
Diffusion coefficient of Li in positive electrode (m^2s^{-1})			$D_p = [146.91({SOC_{sur}}^2) - 286.45(SOC_{sur}) + 140.48] * 10^{-16}$	
Diffusion coefficient of Li in negative electrode (m^2s^{-1})			D_n	$4.8*10^{-15}$
Diffusion coefficient of Li ion in the electrolyte phase (m^2s^{-1})			D_s	$5*10^{-10}$
Transference number			t_+^0	0.363
Ionic conductivity of electrolyte (S m^{-1})			κ	1.3 [89]
Effective electronic conductivity of positive electrode (S m^{-1})			$\sigma_{eff,p}$	6.75 [93]
Reaction rate constant ($mol\ m^{-2}s^{-1}(mol\ m^{-3})^{-1.5}$)	Positive electrode		k_p	$4.5*10^{-12}$
	Negative electrode		k_n	$4.2*10^{-12}$
Initial SOC	Positive electrode		SOC_p	0.035 [94]
	Negative electrode		SOC_n	0.811 [94]
Activation energy for charge transfer (J mol^{-1})	Positive electrode		$E_{act,ct,p}$	13000 [94]
	Negative electrode		$E_{act,ct,n}$	20000 [111]
Activation energy for Li ion diffusion in the electrolyte phase (J mol^{-1})			$E_{act,diff}$	26600 [94]
Activation energy for ionic conductivity of electrolyte (J mol^{-1})			$E_{act,c}$	11000 [94]

Table 6.2: Governing equations and boundary conditions in an electrochemical P2D model

Governing equations	**Boundary conditions**		
	Positive electrode	**Negative electrode**	**Separator**
Mass balance in the electrolyte for a binary salt concentrated electrolyte $\varepsilon_m \frac{\partial c_2}{\partial t} = D_{eff,m} \frac{\partial^2 c_2}{\partial x^2} + a_m(1 - t_+^0) j_m$ Initial condition $c_2\|_{t=0} = c_0$ $m = p$ *or* n or s **Hypotheses** Solvent velocity equals to zero Constant transport properties integrating non-ideality effect Constant porosity Structural properties-porosity and tortuosity-integrated in $D_{eff,m}$ No reaction in the separator	$-D_{eff,p} \left.\frac{\partial c_2}{\partial x}\right\|_{x=l_n+l_s+l_p} = 0$ $c_2\|_{x=l_n+l_s,-} = c_2\|_{x=l_n+l_s,+}$	$-D_{eff,n} \left.\frac{\partial c_2}{\partial x}\right\|_{x=0} = 0$ $-D_{eff,n} \left.\frac{\partial c_2}{\partial x}\right\|_{x=l_n,-} = -D_{eff,s} \left.\frac{\partial c_2}{\partial x}\right\|_{x=l_n,+}$	$c_2\|_{x=l_{n,-}} = c_2\|_{x=l_{n,+}}$ $-D_{eff,s} \left.\frac{\partial c_2}{\partial x}\right\|_{x=l_n+l_s,-} = -D_{eff,p} \left.\frac{\partial c_2}{\partial x}\right\|_{x=l_n+l_s,+}$
Potential distribution in solution phase $\nabla(-\kappa_{eff,m} \frac{\partial \varphi_2}{\partial x} + \frac{2\kappa_{eff,m} RT}{F}(1 - t_+^0) \frac{\partial \ln c_2}{\partial x}) = a_m F j_m$ **Hypotheses** Structural properties-porosity and tortuosity-integrated in $\kappa_{eff,m}$ No reaction in the separator	$i_2\|_{x=l_n+l_s+l_p} = 0$ $\varphi_2\|_{x=l_n+l_s,-} = \varphi_2\|_{x=l_n+l_s,+}$	$i_2\|_{x=0} = 0$ $i_2\|_{x=l_n,-} = i_2\|_{x=l_n,+}$	$\varphi_2\|_{x=l_{n,-}} = \varphi_2\|_{x=l_{n,+}}$ $i_2\|_{x=l_n+l_s,-} = i_2\|_{x=l_n+l_s,+}$
Potentiel distribution in matrix/solid phase $\sigma_{eff,m} \frac{\partial^2 \varphi_1}{\partial x^2} = a_m F j_m$ **Hypotheses** Structural properties-porosity and tortuosity-integrated in $\sigma_{eff,m}$	$i_1\|_{x=l_n+l_s} = 0$ $\left.\frac{\partial \varphi_1}{\partial x}\right\|_{x=l_n+l_s+l_p} = -\frac{I_{app}}{\sigma_{eff,p}}$	$\varphi_1\|_{x=0} = 0$ $i_1\|_{x=l_n} = 0$	
Mass balance-solid-state diffusion only- in the matrix/solid phase $\frac{\partial c_1}{\partial t} = \frac{1}{r_{particle}} \frac{\partial}{\partial r}\left(D_m r_{particle} \frac{\partial c_1}{\partial r}\right)$ Initial condition $c_1\|_{t=0} = c_1^0$	$\left.\frac{\partial c_1}{\partial r}\right\|_{r_{particle}=0} = 0 \quad and \quad -D_m \left.\frac{\partial c_1}{\partial r}\right\|_{r_{particle}=R_m} = j_m$		
Reaction rate at the surface of particles (Butler-Volmer equation)			
$i_m = i_0\left(\exp\left(\frac{\alpha_a F \eta_{sur}}{RT}\right) - \exp\left(-\frac{\alpha_c F \eta_{sur}}{RT}\right)\right)$ $i_0 = F\, k\, c_{1,max} (c_2)^{\alpha_a}$ $\eta_{sur} = \varphi_1 - \varphi_2 - i_m R_c - U(SOC_{sur})$			
The relation between the reaction rate and the pore wall flux			
$i_m = F j_m$			

In reference to our previous work [110] (Chapter 5), in the flat area of cell voltage-capacity curve of Graphite-LFP, activation overpotential was a major factor of the polarization or potential loss. Thus, it was presumed that there was a contact resistance between the particles surface and solid matrix in the positive electrode with low electronic conductivity. The insufficient contact between particles surface and solid matrix hindered the transport of electron to the particles surface and increased the activation overpotential. This contact resistance (R_c) appeared in the overpotential used in Butler-Volmer equation as

$$\eta_{sur} = \varphi_1 - \varphi_2 - i_m R_c - U(SOC_{sur}) \tag{6.1}$$

Where η_{sur} , φ_1, φ_2 are the surface overpotential, electrical potential in solid and solution phases, respectively. i_m shows the local current density in the porous matrix and U is the open circuit potential of the electrode.

Figure 6.2 shows the open-circuit potential (U) of Graphite [105] and LFP [94] as a function of state of charge (SOC).

6.2.2 Thermal model

A lumped thermal model based on the average temperature was assumed in this study. The cylindrical cell was composed of multi components of current collectors, electrodes and separator wound and packaged spirally into a cylinder. Since these components have high thermal conductivity compared to the total generated heat, the layer structure of the cell was presumed as a homogenous material which has a fairly uniform temperature profile [107]. The 2D energy balance equation was expressed as

$$\frac{\partial(\rho C_p T)}{\partial t} = \lambda_r \frac{1}{r}\frac{\partial}{\partial r}\left(r\frac{\partial T}{\partial r}\right) + \lambda_{axial}\frac{\partial^2 T}{\partial z^2} + Q \tag{6.2}$$

Since battery system was assumed to be homogenous, the variations of the density and the heat capacity with location were negligible. The cell density, heat capacity and also thermal conductivity in the radial and axial directions were calculated by [112]

$$\rho = \frac{\sum_{i=1}^{5} l_i \rho_i}{\sum_{i=1}^{5} l_i} \tag{6.3}$$

$$C_p = \frac{\sum_{i=1}^{5} l_i C_{p,i}}{\sum_{i=1}^{5} l_i} \tag{6.4}$$

$$\lambda_r = \frac{\sum_{i=1}^{5} l_i}{\sum_{i=1}^{5} l_i/\lambda_i} \tag{6.5}$$

$$\lambda_{axial} = \frac{\sum_{i=1}^{5} l_i \lambda_i}{\sum_{i=1}^{5} l_i} \tag{6.6}$$

Where $i, l_i, \rho_i, C_{p,i}$ and λ_i are the number of cell components , the thickness, the density, the heat capacity and the thermal conductivity of each component, respectively.

The total generated heat was expressed by

$$Q = -\left[q_{totalpolarization} + T\left(\frac{\partial U_p}{\partial T} - \frac{\partial U_n}{\partial T}\right) I_{app}\right] / L_{batt} \tag{6.7}$$

The first term on the right side of the Eq. (6.7) is the heat caused by the total polarization or internal losses inside the cell. The second term is the entropy heat ($\frac{\partial U}{\partial T}$) of Graphite [113] and LFP [114] as a function of SOC are presented in Figure 6.3. The total polarization of the cell is the difference between the cell potential and the cell open circuit voltage. It is equal to the summation of all polarizations occurring in multi areas of the cell. Referring to Nyman's paper [65], the total polarization of cell was separated into different polarizations including the activation overpotential, the ohmic potential drop and the diffusion polarization in both solid and solution phases. Thus, the heat produced by the total polarization of cell can be calculated by:

$$q_{totalpolarization} = q_{irreversible\ reaction} + q_{ohmic} + q_{diffusion,1} \tag{6.8}$$

The heat caused by each polarization inside the cell was introduced in the followings.

The irreversible reaction heat (q_i) the heat induced by activation overpotential was obtained by [115]

$$q_{irreversible\ reaction} = a\ i_m\ \eta_{sur} \tag{6.9}$$

The ohmic heat caused by ohmic potential drop in solid phase, ohmic potential drop in solution phases and diffusion polarization in solution phase was defined as follow [107]

$$q_{ohmic} = \sigma_{eff}\left(\frac{\partial \varphi_1}{\partial x}\right)^2 + \kappa_{eff}\left(\frac{\partial \varphi_2}{\partial x}\right)^2 - \frac{2\kappa_{eff} RT}{F}\left(1 - t_+^0\right)\frac{\partial\ ln\ c_2}{\partial x}\frac{\partial \varphi_2}{\partial x} \tag{6.10}$$

As mentioned before, the heat induced by diffusion polarization in solid phase was not considered in most previous works. The presented study included this heat generation source. During discharge as the current passes, the concentration gradients are formed inside the solid phase. The heat produced during the formation of these concentration gradients in solid phase is equal to the heat exchanged as the current is interrupted and the Li concentration in the electrode becomes uniform after infinite time. This heat is called the relaxation heat. With reference to Nyman's paper [65], the average diffusion polarization was calculated by:

$$Averaged\ diffusion\ polarization\ in\ solid\ phase = \frac{1}{I_{app}} \int_0^l ai_m \left(U(SOC_{surf}) - U(SOC_{ave})\right) dx \tag{6.11}$$

$U(SOC_{surf})$ is the open circuit potential of the electrode immediately after the current interruption and $U(SOC_{ave})$ is the open circuit potential of the electrode at an infinite time after the current interruption. l is the total thickness of the layers forming the cell in P2D model.

Therefore, the local volumetric heat induced by the diffusion polarization in solid phase or relaxation heat was defined as below

$$q_{relaxation} = a\, i_m (U(SOC_{surf}) - U(SOC_{ave})) \tag{6.12}$$

Initial and Boundary Conditions:

The initial value of cell temperature was equal to the ambient temperature [115]

$$T = T_{amb} \qquad t = 0 \tag{6.13}$$

At the boundary of battery, in accordance with the Newton's cooling law, the following boundary condition was expressed. The radiation was neglected in this study [112].

$$-\lambda \nabla T = h(T - T_{amb}) \tag{6.14}$$

Many physicochemical properties, such as the diffusion coefficient and ionic conductivity of electrolyte and reaction rate constants depend on the temperature. The Arrhenius equation was used to represent the temperature dependency of the physicochemical properties and also to couple the thermal model with the electrochemical model.

$$\Theta = \Theta_{ref} exp\left[\frac{E_{act,\Theta}}{R}\left(\frac{1}{T_{ref}} - \frac{1}{T}\right)\right] \tag{6.15}$$

Where Θ, Θ_{ref} and $E_{act,\Theta}$ represent physicochemical parameters, their values at a reference temperature and the required energy activation, respectively.

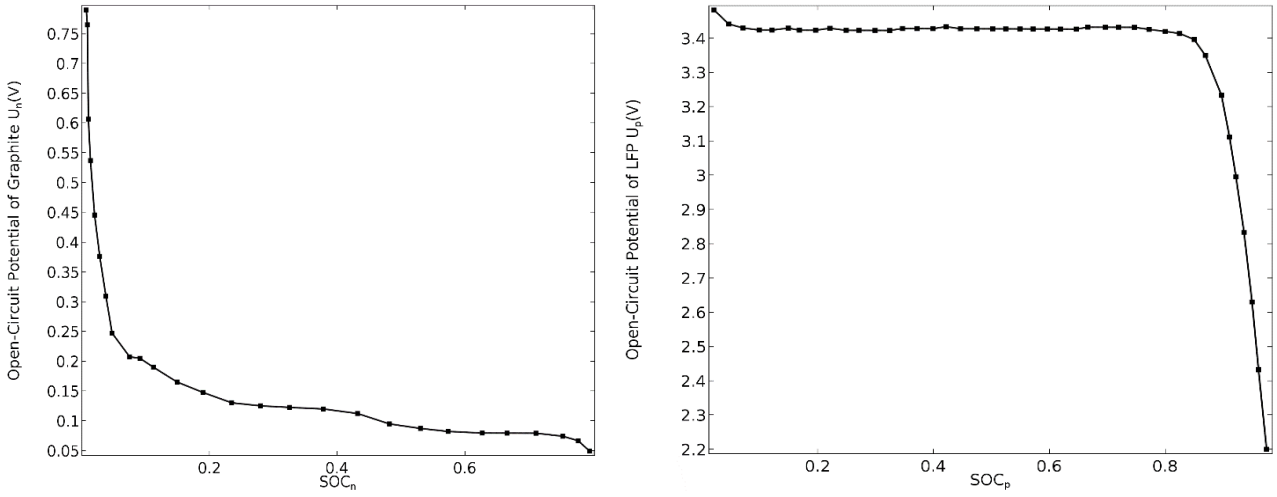

Figure 6.2: Open circuit potential of Graphite [105] and LFP [94] as a function of SOC

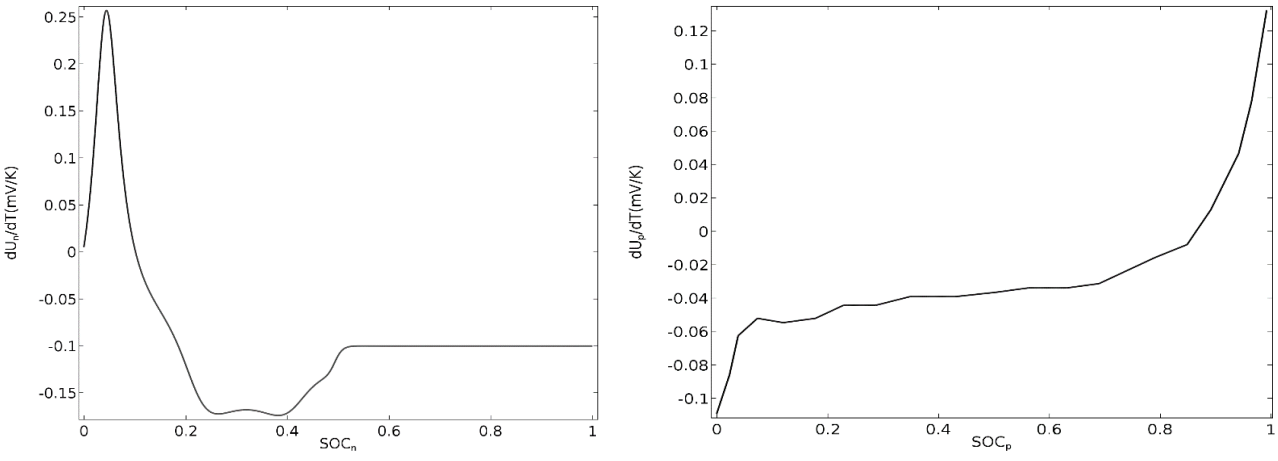

Figure 6.3: Entropy heats of Graphite [113] and LFP [114] as a function of SOC

6.2.3 Numerical Solution

COMSOL Multiphysics 5.2 was used to solve the electrochemical P2D model and thermal model simultaneously. As observed in Figure 6.1 two models were coupled through the average generated heat and the average temperature of the cell. The relaxation heat source in solid phase

as an additional heat source was added to the heat transfer interface of COMSOL. A mesh control edges for 1-D geometry and a mapped mesh for 2-D geometry were selected. A direct solver of MUMPS (Multifrontal Massively Parallel sparse direct Solver) was used to solve the electrochemical and thermal equations and to find the unknown parameters of Electrical potential (φ), Li concentration (c) in solid and solution phases and temperature (T).

6.3 Results and Discussion

6.3.1 The effect of temperature dependent physicochemical parameters on cell voltage and cell surface temperature

Four parameters including Li ion diffusion coefficient in electrolyte, ionic conductivity of electrolyte and reaction rate constants of both negative electrode (Graphite) and positive electrode (LFP) were assumed to be dependent on temperature. The simulated results of a given model were compared with that of a model neglecting the temperature dependent parameters. The results showed that considering temperature dependent parameters in the model led to a higher cell voltage and a lower cell surface temperature for all high C-rates (2C, 3.75C, 7.5C and 10C) as seen in Figures 6.4 and 6.5. The reason is because the temperature raising increased the physicochemical properties resulting to an ionic flux augmentation, a reaction rate expedition and to decrease the cell total polarization and the internal resistances inside the cell. According to Figures 6.4 and 6.5, the differences between two models were intensified at higher C-rates (7.5C and 10C) because the total polarization of cell or the total potential loss was more pronounced at higher C-rates.

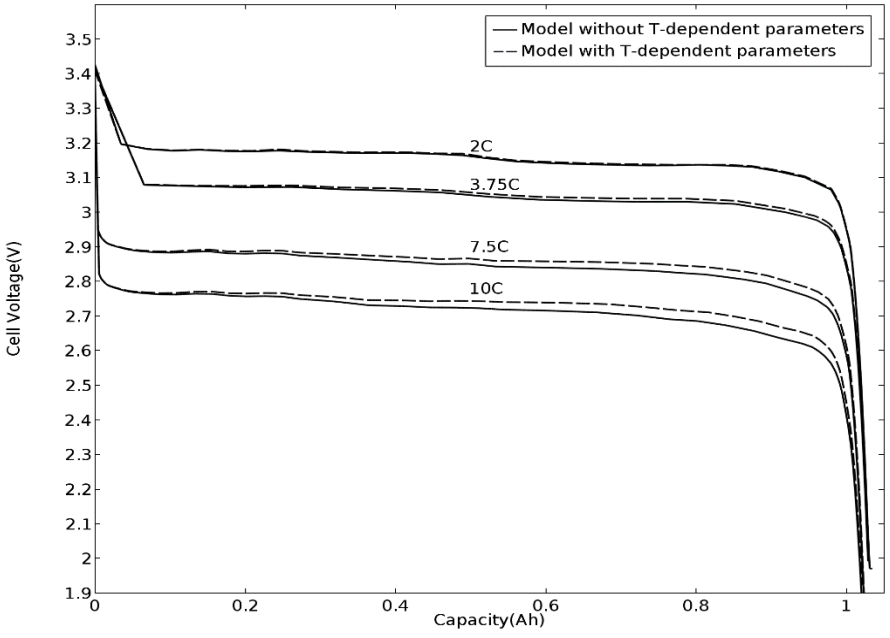

Figure 6.4: A comparison of cell voltage-capacity curves between two models with and without considering T-dependent physicochemical parameters

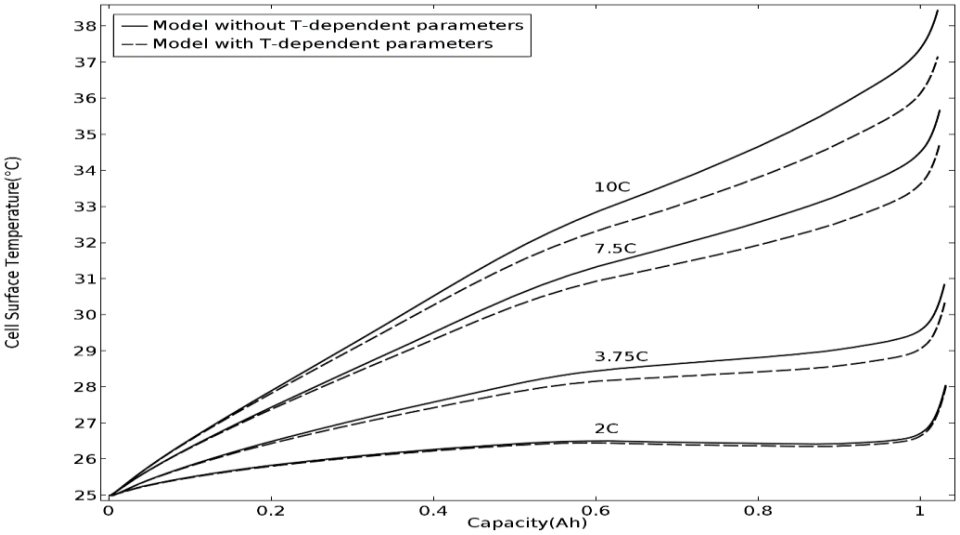

Figure 6.5: Cell surface temperature curves versus capacity for two models with and without considering T-dependent physicochemical parameters

6.3.2 The model validation with experimental data

Based on the previous section, an electrochemical-thermal model based on temperature-dependent parameters was used to be validated with the experimental data referred to a commercial cylindrical cell of Graphite-LFP provided by Hydro-Québec. The experiments were conducted at environmental chamber temperature of 25°C. Figures 6.6 and 6.7 illustrated the evolution of the cell voltage and cell surface temperature versus capacity for different high discharge rates. The results indicated there was an approximate good agreement between simulation results and experimental data. As expected, the higher C-rates bring about the higher cell surface temperatures due to the larger internal resistance inside the cell. Thus recognizing the major transport and thermal mechanisms at higher C-rates is essential for battery manufacturers to design a proper thermal management system.

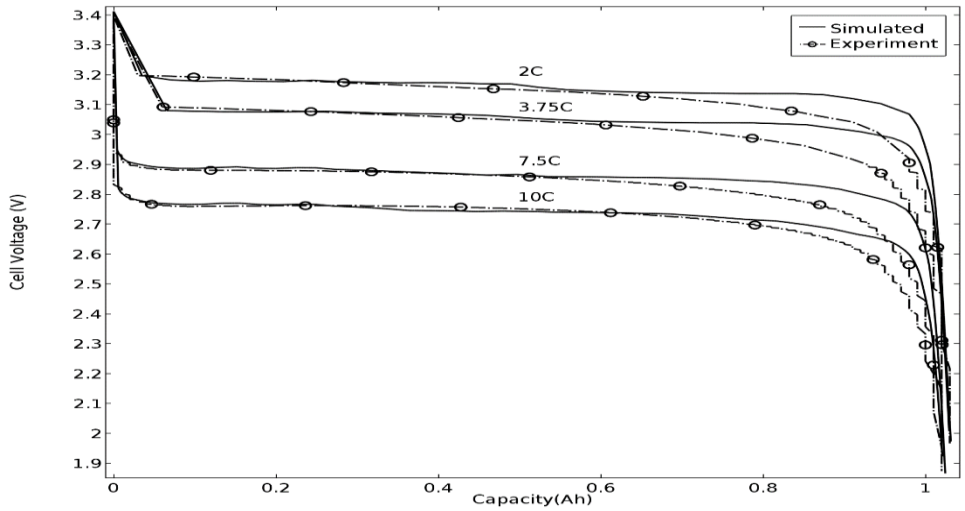

Figure 6.6: Simulated cell voltage-capacity curves compared to experimental data at high discharge C-rates

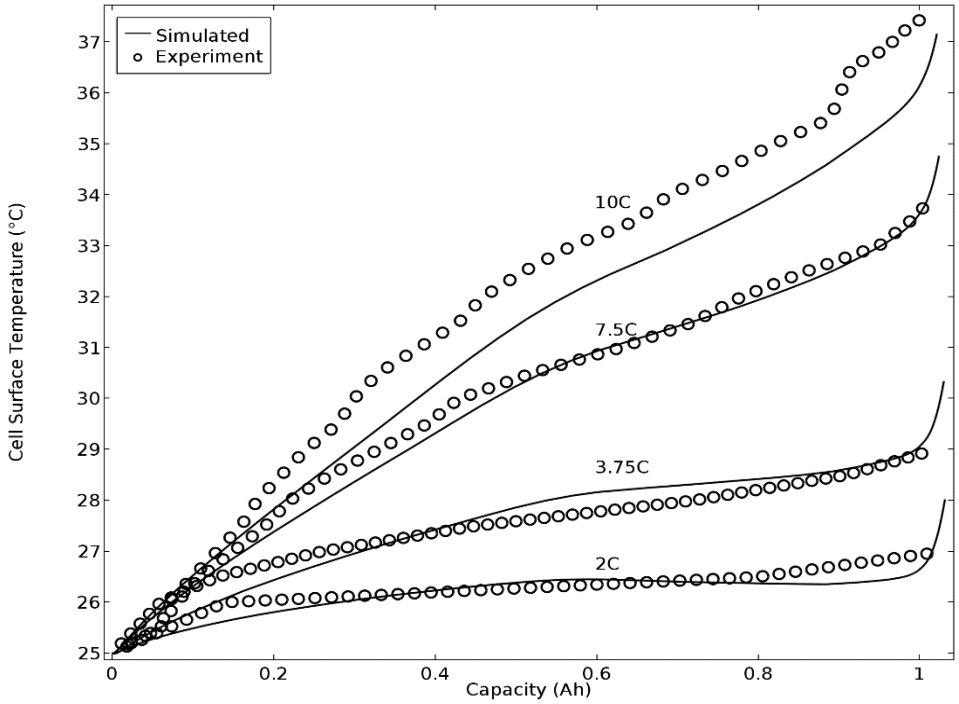

Figure 6.7: Simulated cell surface temperature-capacity curves compared to experimental data at high discharge C-rates

6.3.3 The total generated heat of the cell

The total generated heat of cell was calculated by Eq. (6.7). Figure 6.8 represented the portion of heat originated from each polarization in various components of the cell at the end of discharge (t=468s) for 7.5 C-rate. The results indicated that heat induced by diffusion polarization (relaxation heat) in solid phase of LFP has an enormous contribution in the total generated heat at the end of discharge which confirmed our previous results (Chapter 5). We showed that diffusion of Li species in solid phase of LFP was a main mechanism controlling the cell performance at the end of discharge in our previous paper [110] (Chapter 5). Decreasing particles size of LFP is a method to dominate over the mass transport limitations in LFP which lead to an extreme temperature rise inside the cell at the end of discharge. Figure 6.9 compared the cell surface temperature-capacity curves of two models with and without considering the heat originated from diffusion polarization in solid phase. By considering the heat generated by diffusion polarization in solid phase, the cell surface temperature was increased at all C-rates which showed the significance of considering this term in the total generated heat of the cell.

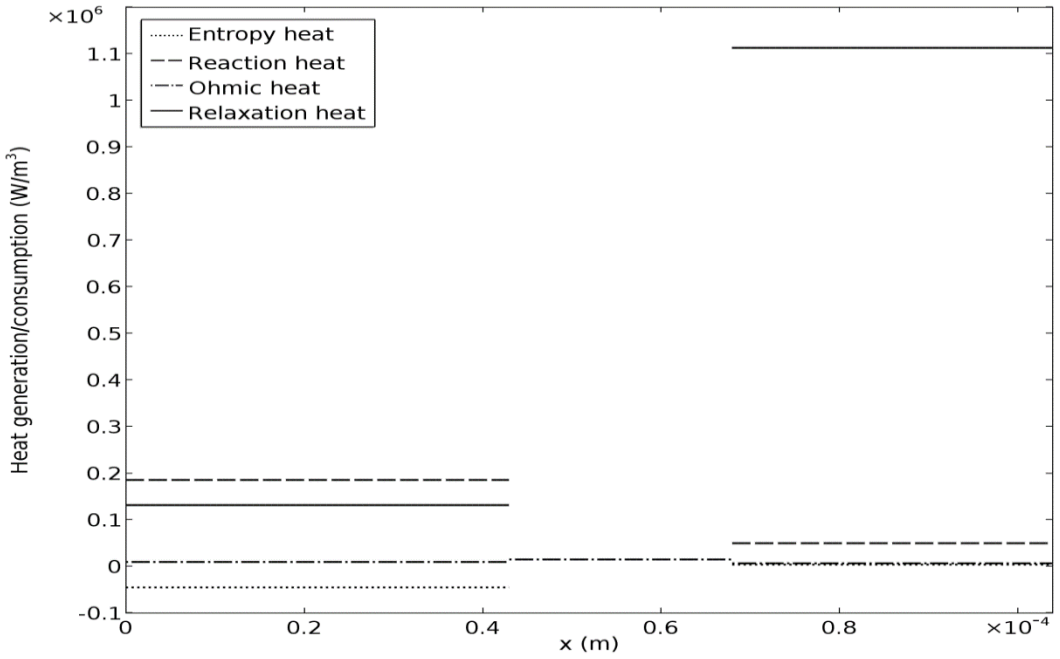

Figure 6.8: Heat generation/consumption in various cell components for 7.5C-rate at the end of discharge (t=468s)

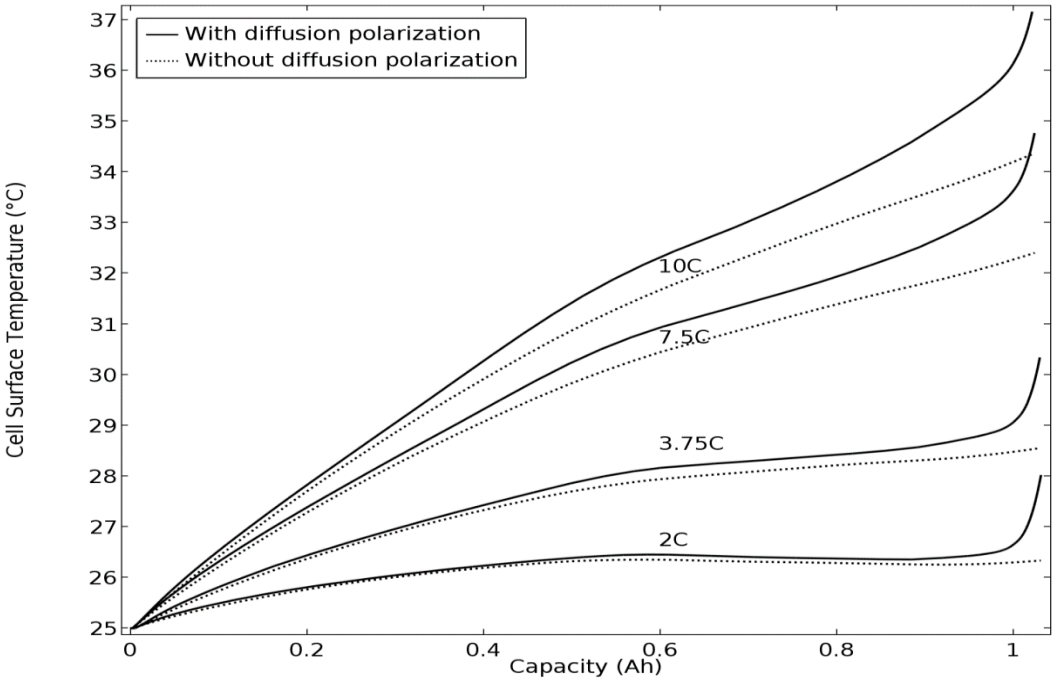

Figure 6.9: Comparisons of cell surface temperature-capacity curves between two models with and without considering the heat originated from diffusion polarization

Figure 6.10 showed the total generated heat, the irreversible reaction heat, the entropy heat, the ohmic heat and the relaxation heat during discharge time at 7.5 C-rate. The irreversible reaction heat was recognized as a major heat generation source in the flat area of cell voltage-capacity curve due to the high activation overpotential in this area as reported by our previous work [110] (Chapter 5). One of the ways to control the generated reaction heat is to coat the LFP with carbon black uniformly leading to increase electronic conductivity of LFP and to decrease activation overpotential in LFP. Additionally, the ratio of each heat related to the total generated heat was illustrated in Figure 6.11 as a bar chart at t= 250s and t=468s at 7.5C-rate. From the given bar chart it was seen that around 0.95 and 0.88 of the total generated heat were related to the reaction heat in the flat area of the cell voltage-capacity curve (t=250s) and the heat caused by diffusion polarization (relaxation heat) in solid phase at the end of discharge (t=468s), respectively.

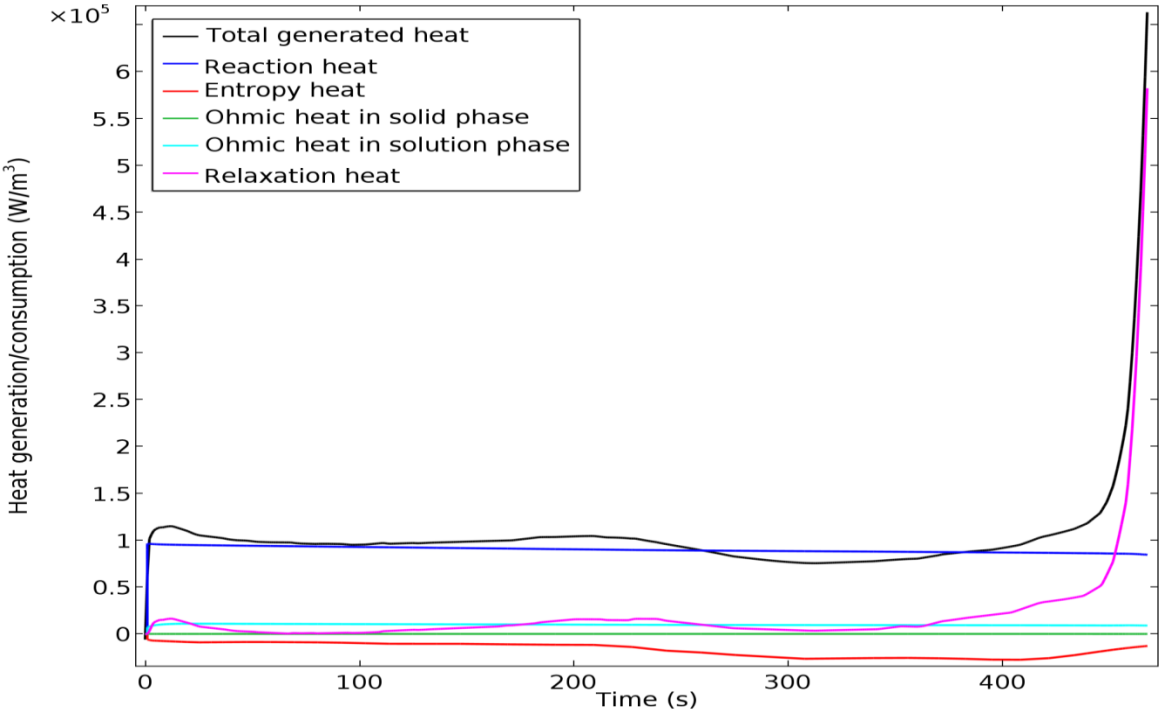

Figure 6.10: heat generation/consumption sources at 7.5C during discharge time

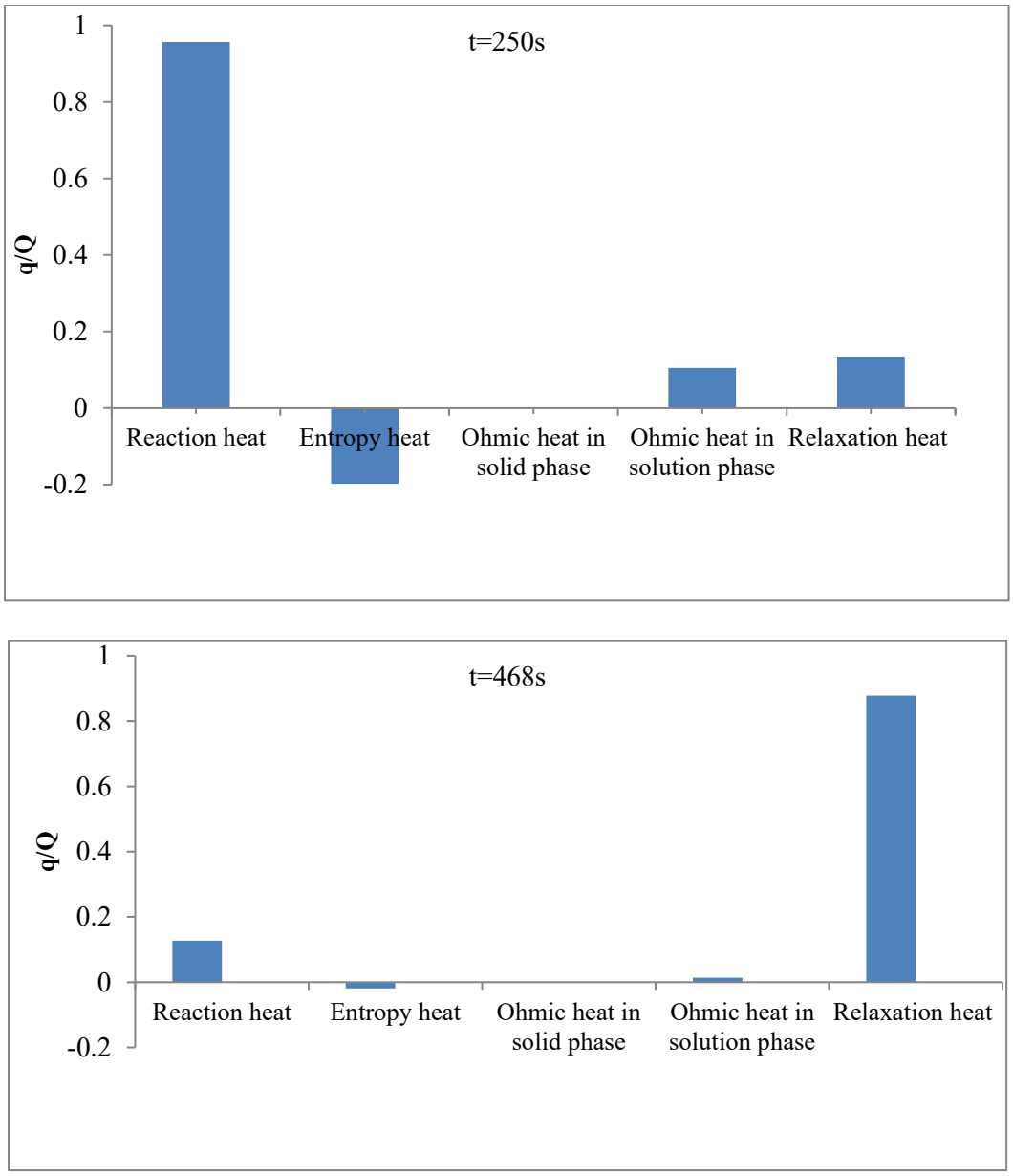

Figure 6.11: The ratio of each heat generation/consumption source to the total generated heat at t=250s and t=468s at 7.5 C

Contours of temperature distribution across the cell at the end of discharge for 7.5 and 10 C-rates were presented in Figure 6.12. The maximum and minimum temperatures were accumulated in the center and the surface of the cell, respectively. The temperature distribution in the axial direction was uniform due to higher conductivity resulting in the smaller Biot number in this direction compared to the radial direction.

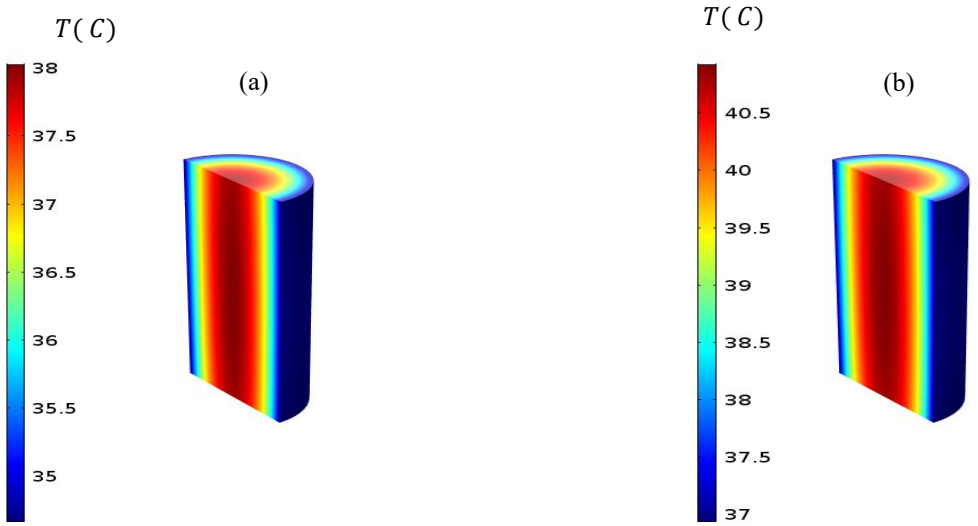

Figure 6.12: Temperature distribution contours at the end of discharge for (a) 7.5C (b) 10C

6.4 Conclusion

An electrochemical P2D model coupled with a lumped thermal model was developed to predict the electrochemical and thermal behaviors across a commercial 18650 cylindrical Graphite-LFP cell during discharge at high C-rates. A detailed study of the transport phenomena occurring inside the cell can be as a beneficial tool to design a proper thermal management system. A comparison was done between a model considering the temperature dependent physicochemical parameters and the one neglecting this dependency. Higher cell voltages and lower surface temperatures were as a result of the dependency of parameters on temperatures. Additionally, the results indicated that the effect of the temperature dependent parameters becomes more pronounced specially at higher C-rates of 7.5 and 10. Furthermore, the results were validated with the experimental data provided by Hydro-Québec. The effect of heat generated by Li diffusion in solid phase or relaxation heat was not considered in the previous models. Since diffusion polarization in LFP was a major limiting factor of cell performance during the end of discharge time, considering the heat originated from this process was essential. The results showed a steep rise in temperature at the end of discharge time as a result of the heat induced by diffusion polarization in solid phase. At 7.5 C-rate, around 0.88 of the total generated heat of cell was related to this heat generation source at the end of discharge. Additionally, the irreversible reaction heat in the flat area of cell voltage-capacity curve during discharge time was a major heat source which meant that reaction limited the cell performance in this area. Two procedures to decrease internal resistances induced by reaction and diffusion and to control the cell temperature are uniform coating of LFP with carbon black and decreasing the particles size of LFP. In addition, the presented temperature contours inside the cell cited that the maximum temperature was located in the central part of the cylindrical cell due to the most heat accumulation. As a future work, the effects of other polarizations such as side reactions in the cell and the contact resistances between connectors and terminals can be included in the model.

6.5 Acknowledgments

The authors would like to thank Hydro-Québec and the Natural Sciences and Engineering Council of Canada (NSERC) for their financial support.

CHAPITRE 7

Conclusion et perspectives

7.1 Conclusion générale

Le travail présenté dans cette thèse a porté sur deux facteurs essentiels dans la conception de batteries électriques : la performance et la sécurité. A l'aide de modèles mathématiques améliorés, il a été possible de mieux comprendre l'effet des propriétés structurelles des batteries sur leur performance et de pouvoir proposer de nouvelles structures pour les batteries futures qui auront ainsi une efficacité plus élevée. Le chapitre 3 a montré comment la performance des cellules Li-ion était affectée par la porosité et de la distribution granulométrique dans l'électrode positive ($Li_yMn_2O_4$) au cours du processus de décharge. L'énergie spécifique maximale a été atteinte pour une porosité d'environ 0.55, alors que la puissance spécifique y avait encore une valeur élevée. Une augmentation ou une diminution au-delà de cette valeur optimale a conduit à une chute de voltage et à des capacités de cellule inférieures en raison des limitations de la cinétique et du transfert de masse dans l'électrode poreuse. De plus, l'analyse de la distribution des tailles de particules différentes (monomodale, bimodale et 3-particules) avec différentes fractions volumiques de petites et grandes particules dans l'électrode positive a montré que la performance de la cellule est extrêmement affectée par la fraction volumique de petites et grandes particules dans un modèle de distribution de la taille des particules. En fait, l'augmentation de la fraction volumique des plus petites particules dans les modèles bimodaux et 3-particules a permis d'améliorer la performance de cellule (augmentation du voltage de cellule, uniformité des densités de courant locales et diminution de la polarisation totale). En outre, différents taux de décharge ont été appliqués à plusieurs modèles de distribution de la taille des particules. Les résultats montrent que la distribution de la taille des particules a un effet plus important sur le voltage de la cellule, la capacité de la cellule et la puissance spécifique de la cellule à des taux de décharge plus élevés.

Comme mentionné au chapitre 3, l'effet de la position des particules dans les modèles de distribution granulométrique a été négligé et il a été supposé que les particules de tailles différentes étaient situées à toutes les positions dans l'électrode positive. Ainsi, le chapitre 4 a développé le modèle présenté du chapitre 3 pour étudier l'effet de la position des particules sur la performance de la cellule, dans une électrode positive composée d'une distribution granulométrique bimodale. En fait, l'électrode positive consistait en deux couches: la première couche à proximité du séparateur et la deuxième couche à proximité du collecteur de courant. Deux états pour deux couches ont été considérés: le premier état supposait que les première et seconde couches étaient respectivement constituées de plus grosses particules et de plus petites particules. Le deuxième état était l'inverse du premier. En considérant la même épaisseur de chaque couche, les résultats ont indiqué que, pour une conception de cette électrode positive quelle que soit la taille des particules, la fraction volumique des particules proches du séparateur devrait toujours être inférieure à celle des particules proches du collecteur de courant. On en déduit que la perte totale de potentiel atteint sa valeur minimale dans cette situation. De plus, l'épaisseur de chaque couche était considérée comme variable. En conclusion, la perte minimale

de potentiel a été atteinte par une valeur optimale entre a=1.5 and a=2 (a est le rapport de l'épaisseur totale de l'électrode positive à l'épaisseur de la couche composée de particules plus petites). Plus on s'écarte de cette valeur spécifique, plus les pertes de potentiel sont importantes en raison des différents mécanismes de transport entre deux couches de l'électrode positive.

Les principaux objectifs du chapitre 5 étaient la compréhension approfondie des mécanismes de transport qui se produisent à l'intérieur d'une cellule Li-ion à base de graphite-LFP et la détection des principaux mécanismes de transport impliqués dans la polarisation des cellules. La polarisation à l'intérieur de la cellule peut provenir de la polarisation de diffusion et de la chute de potentiel ohmique dans les phases solide et solution, de la surtension d'activation et de la résistance de contact entre les différentes parties de l'électrode. La surtension d'activation et la polarisation de diffusion en phase solide ont été identifiées comme des facteurs limitant la performance de la cellule dans la zone du plateau et dans la zone de pente raide de la courbe voltage-capacité de cellule. Les résultats ont montré qu'à des taux de décharge inférieurs, la limitation du transport de masse dans la structure du LFP pouvait être expliquée par un coefficient de diffusion dépendant de la concentration. À des taux de décharge plus élevés, ce modèle n'a pas pu décrire la perte de voltage attribuée à la polarisation d'activation dans la zone du plateau. Au lieu de cela, un modèle mixte basé sur un coefficient de diffusion dépendant de la concentration et une résistance de contact à la surface des particules de LFP a été proposé. La caractéristique de faible conductivité électronique du LFP a été expliquée en considérant la résistance de contact à la surface des particules de LFP. Le chapitre 6 a combiné le modèle électrochimique du chapitre 5 avec un modèle thermique pour évaluer le pourcentage de la chaleur causée par chaque polarisation se produisant dans plusieurs zones de la cellule sur l'ensemble de la chaleur produite à des taux de décharge plus élevés. Puisque la polarisation de la diffusion dans le LFP était le principal facteur limitant de la performance de la cellule en fin de décharge, la chaleur qui en résultait provoquait une forte augmentation de la température en fin de décharge. De plus, la chaleur causée par la surtension d'activation a été reconnue comme une source de chaleur majeure dans la zone du plateau de la courbe voltage-capacité de la cellule. En outre, une comparaison a été effectuée entre un modèle prenant en compte les paramètres physico-chimiques dépendant de la température et celui négligeant cette dépendance. Des tensions de cellules plus élevées et des températures de surface plus basses résultaient de la dépendance des paramètres sur la température. Ces effets sont plus prononcés à des taux de décharge plus élevés. Les contours de température à l'intérieur de la cellule ont montré que la partie centrale de la cellule cylindrique a la température maximale. De plus, le modèle a été validé avec des données expérimentales fournies par Hydro-Québec.

7.2 Suggestions de travaux futurs

- Parfois, les batteries ont besoin de matériaux différents chargés dans différents rapports dans leur électrode positive pour optimiser la puissance de la batterie. Les batteries couramment utilisées dans les voitures sont composées d'une électrode positive avec des composants multiples comme le lithium, le nickel, le manganèse, le cobalt (NMC) ou une combinaison de lithium, nickel, cobalt, aluminium (NCA). La combinaison de ces deux matériaux pourrait entraîner une avancée dans la technologie des batteries. Puisque les propriétés structurales telles que la porosité et la distribution granulométrique dans l'électrode positive sont importantes pour optimiser la puissance de la batterie, le modèle

présenté aux chapitres 3 et 4 serait un outil facilement adaptable pour concevoir une électrode positive mixte.

- Les chapitres 3 et 4 ont étudié l'effet de la distribution de la taille des particules dans l'état isotherme. Le modèle peut être étendu au modèle thermique. Comme l'uniformité du SOC (le rapport des ions Li intercalées dans la phase solide à la concentration maximale de Li) dans la structure d'électrode peut augmenter la puissance de la cellule en raison de la diminution de la résistance interne, il est prévisible que la distribution granulométrique des électrodes affectera la distribution de température à l'intérieur de la cellule et que les modèles développés dans cette thèse permettront d'en prédire les effets.

- En tant que travaux futurs, les effets d'autres polarisations liées aux réactions secondaires se produisant dans la cellule, les résistances de contact entre les connecteurs et les terminaux et le mouvement du courant dans les collecteurs de courant peuvent être facilement ajoutés aux modèles. Dans les batteries de grande taille, les hétérogénéités dans les réactions électrochimiques, le SOC et la température peuvent affecter de manière significative la performance des cellules, la sécurité et la durée de vie des batteries. Ainsi, la discrétisation des batteries en cellules de plus petite taille et la prise en compte de toutes les polarisations qui se produisent à l'intérieur de la cellule peuvent aider à concevoir correctement des batteries de plus grande taille.

- Utiliser le modèle développé pour améliorer la conception des piles commerciales.

RÉFÉRENCES

[1] B. Wu, Y. Ren, and N. Li, “LiFePO4 Cathode Material,” in *Electric Vehicles, The Benefits and Barriers*, S. Soylu, Ed. InTech, 2011.

[2] A. Latz, J. Zausch, and O. Iliev, “Modeling of Species and Charge Transport in Li–Ion Batteries Based on Non-equilibrium Thermodynamics,” in *Numerical Methods and Applications*, I. Dimov, S. Dimova, and N. Kolkovska, Eds. Springer Berlin Heidelberg, 2011, pp. 329–337.

[3] O. Salazar, “Li-Ion battery Model”. *https://www.scribd.com/document/328933488/ Battery,* (2015).

[4] C. M. Julien, A. Mauger, K. Zaghib, and H. Groult, “Comparative Issues of Cathode Materials for Li-Ion Batteries,” *Inorganics*, vol. 2, no. 1, pp. 132–154, Mar. 2014.

[5] W. van Schalkwijk and B. Scrosati, *Advances in Lithium-Ion Batteries*. Springer Science & Business Media, 2002.

[6] M. S. Whittingham, “Lithium batteries and cathode materials,” *Chem. Rev.*, vol. 104, no. 10, pp. 4271–4301, Oct. 2004.

[7] C. M. Doyle, *Design and Simulation of Lithium Rechargeable Batteries*. University of California, Berkeley, 1995.

[8] V. Ramadesigan, P. W. C. Northrop, S. De, S. Santhanagopalan, R. D. Braatz, and V. R. Subramanian, “Modeling and Simulation of Lithium-Ion Batteries from a Systems Engineering Perspective,” *J. Electrochem. Soc.*, vol. 159, no. 3, pp. R31–R45, Jan. 2012.

[9] M. Petit, E. Prada, and V. Sauvant-Moynot, “Development of an empirical aging model for Li-ion batteries and application to assess the impact of Vehicle-to-Grid strategies on battery lifetime,” *Appl. Energy*, vol. 172, pp. 398–407, Jun. 2016.

[10] I. Bloom *et al.*, “An accelerated calendar and cycle life study of Li-ion cells,” *J. Power Sources*, vol. 101, no. 2, pp. 238–247, Oct. 2001.

[11] F. Saidani, F. X. Hutter, R.-G. Scurtu, W. Braunwarth, and J. N. Burghartz, “Lithium-ion battery models: a comparative study and a model-based powerline communication,” *Adv Radio Sci*, vol. 15, pp. 83–91, Sep. 2017.

[12] D. Zhang, B. N. Popov, and R. E. White, “Modeling Lithium Intercalation of a Single Spinel Particle under Potentiodynamic Control,” *J. Electrochem. Soc.*, vol. 147, no. 3, pp. 831–838, Mar. 2000.

[13] S. Santhanagopalan, Q. Guo, P. Ramadass, and R. E. White, “Review of models for predicting the cycling performance of lithium ion batteries,” *J. Power Sources*, vol. 156, no. 2, pp. 620–628, Jun. 2006.

[14] M. B. Pinson and M. Z. Bazant, "Theory of SEI Formation in Rechargeable Batteries: Capacity Fade, Accelerated Aging and Lifetime Prediction," *ArXiv12103672 Cond-Mat Physicsphysics*, Oct. 2012.

[15] B. Rajabloo, W. Wakem, A. Jokar, M. Desilets, and G. M. Brisard, "A Semi-Empirical Aging Model for Lithium Iron Phosphate Electrode," *Meet. Abstr.*, vol. MA2017-01, no. 5, pp. 412–412, Apr. 2017.

[16] M. Doyle and J. Newman, "Analysis of capacity–rate data for lithium batteries using simplified models of the discharge process," *J. Appl. Electrochem.*, vol. 27, no. 7, pp. 846–856, Jul. 1997.

[17] M. Doyle and J. Newman, "Modeling the performance of rechargeable lithium-based cells: design correlations for limiting cases," *J. Power Sources*, vol. 54, no. 1, pp. 46–51, Mar. 1995.

[18] V. Ramadesigan, R. N. Methekar, F. Latinwo, R. D. Braatz, and V. R. Subramanian, "Optimal Porosity Distribution for Minimized Ohmic Drop across a Porous Electrode," *J. Electrochem. Soc.*, vol. 157, no. 12, p. A1328, 2010.

[19] M. Doyle, T. F. Fuller, and J. Newman, "Modeling of Galvanostatic Charge and Discharge of the Lithium/Polymer/Insertion Cell," *J. Electrochem. Soc.*, vol. 140, no. 6, pp. 1526–1533, Jun. 1993.

[20] G. G. Botte, V. R. Subramanian, and R. E. White, "Mathematical modeling of secondary lithium batteries," *Electrochimica Acta*, vol. 45, no. 15–16, pp. 2595–2609, May 2000.

[21] G. G. Botte, B. A. Johnson, and R. E. White, "Influence of Some Design Variables on the Thermal Behavior of a Lithium-Ion Cell," *J. Electrochem. Soc.*, vol. 146, no. 3, pp. 914–923, Mar. 1999.

[22] L. Cai and R. E. White, "Mathematical modeling of a lithium ion battery with thermal effects in COMSOL Inc. Multiphysics (MP) software," *J. Power Sources*, vol. 196, no. 14, pp. 5985–5989, Jul. 2011.

[23] T. F. Fuller, M. Doyle, and J. Newman, "Simulation and Optimization of the Dual Lithium Ion Insertion Cell," *J. Electrochem. Soc.*, vol. 141, no. 1, pp. 1–10, Jan. 1994.

[24] P. Ramadass, B. Haran, R. White, and B. N. Popov, "Mathematical modeling of the capacity fade of Li-ion cells," *J. Power Sources*, vol. 123, no. 2, pp. 230–240, Sep. 2003.

[25] A. Jokar, B. Rajabloo, M. Désilets, and M. Lacroix, "Review of simplified Pseudo-two-Dimensional models of lithium-ion batteries," *J. Power Sources*, vol. 327, pp. 44–55, Sep. 2016.

[26] G. B. Less *et al.*, "Micro-Scale Modeling of Li-Ion Batteries: Parameterization and Validation," *J. Electrochem. Soc.*, vol. 159, no. 6, pp. A697–A704, Jan. 2012.

[27] J. Newman and W. Tiedemann, “Porous-electrode theory with battery applications,” *AIChE J.*, vol. 21, no. 1, pp. 25–41, Jan. 1975.

[28] M. Doyle, J. Newman, A. S. Gozdz, C. N. Schmutz, and J.-M. Tarascon, “Comparison of Modeling Predictions with Experimental Data from Plastic Lithium Ion Cells,” *J. Electrochem. Soc.*, vol. 143, no. 6, pp. 1890–1903, Jun. 1996.

[29] K. West, T. Jacobsen, and S. Atlung, “Modeling of Porous Insertion Electrodes with Liquid Electrolyte,” *Electrochem. Soc. J.*, vol. 129, no. 7, pp. 1480–1485, 1982.

[30] B. Tjaden, S. J. Cooper, D. J. Brett, D. Kramer, and P. R. Shearing, “On the origin and application of the Bruggeman correlation for analysing transport phenomena in electrochemical systems,” *Curr. Opin. Chem. Eng.*, vol. 12, pp. 44–51, May 2016.

[31] D. a. G. Bruggeman, “Berechnung verschiedener physikalischer Konstanten von heterogenen Substanzen. I. Dielektrizitätskonstanten und Leitfähigkeiten der Mischkörper aus isotropen Substanzen,” *Ann. Phys.*, vol. 416, no. 8, pp. 665–679, Jan. 1935.

[32] T. M. Bandhauer, S. Garimella, and T. F. Fuller, “A Critical Review of Thermal Issues in Lithium-Ion Batteries,” *J. Electrochem. Soc.*, vol. 158, no. 3, pp. R1–R25, Mar. 2011.

[33] M. Broussely *et al.*, “Main aging mechanisms in Li ion batteries,” *J. Power Sources*, vol. 146, no. 1, pp. 90–96, Aug. 2005.

[34] P. Ramadass, B. Haran, R. White, and B. N. Popov, “Capacity fade of Sony 18650 cells cycled at elevated temperatures. Part I. Cycling performance,” *J. Power Sources*, vol. 112, pp. 606–613, 2002.

[35] R. Spotnitz and J. Franklin, “Abuse behavior of high-power, lithium-ion cells,” *J. Power Sources*, vol. 113, no. 1, pp. 81–100, Jan. 2003.

[36] S. Zhang, K. Xu, and T. Jow, “Low-temperature performance of Li-ion cells with a LiBF4-based electrolyte,” *J. Solid State Electrochem.*, vol. 7, no. 3, pp. 147–151, Mar. 2003.

[37] A. A. Pesaran, “Battery thermal models for hybrid vehicle simulations,” *J. Power Sources*, vol. 110, no. 2, pp. 377–382, Aug. 2002.

[38] P. Hovington *et al.*, “New Lithium Metal Polymer Solid State Battery for an Ultrahigh Energy: Nano C-LiFePO4 versus Nano Li1.2V3O8,” 16-Mar-2015. [Online]. Available: https://pubs.acs.org/doi/abs/10.1021/acs.nanolett.5b00326.

[39] K. Zaghib *et al.*, “Safe and fast-charging Li-ion battery with long shelf life for power applications,” *J. Power Sources*, vol. 196, no. 8, pp. 3949–3954, Apr. 2011.

[40] M. Oswal, J. Paul and R. Zhao, “A comparative study of lithium ion batteries,” University of Southern California, pp. 2419-2430, 2010.

[41] M. R. Palacín, “Recent advances in rechargeable battery materials: a chemist’s perspective,” *Chem. Soc. Rev.*, vol. 38, no. 9, pp. 2565–2575, Aug. 2009.

[42] J. Newman, “Optimization of Porosity and Thickness of a Battery Electrode by Means of a Reaction-Zone Model,” *J. Electrochem. Soc.*, vol. 142, no. 1, pp. 97–101, 1995.

[43] S. De, P. W. C. Northrop, V. Ramadesigan, and V. R. Subramanian, “Model-based simultaneous optimization of multiple design parameters for lithium-ion batteries for maximization of energy density,” *J. Power Sources*, vol. 227, pp. 161–170, Apr. 2013.

[44] Y. Dai and V. Srinivasan, “On Graded Electrode Porosity as a Design Tool for Improving the Energy Density of Batteries,” *J. Electrochem. Soc.*, vol. 163, no. 3, pp. A406–A416, 2016.

[45] U. von Sacken, E. Nodwell, A. Sundher, and J. R. Dahn, “Comparative thermal stability of carbon intercalation anodes and lithium metal anodes for rechargeable lithium batteries,” *J. Power Sources*, vol. 54, no. 2, pp. 240–245, Apr. 1995.

[46] T. D. Tran, J. H. Feikert, R. W. Pekala, and K. Kinoshita, “Rate effect on lithium-ion graphite electrode performance,” *J. Appl. Electrochem.*, vol. 26, no. 11, pp. 1161–1167, Nov. 1996.

[47] R. Darling and J. Newman, “Modeling a Porous Intercalation Electrode with Two Characteristic Particle Sizes,” *J. Electrochem. Soc.*, vol. 144, no. 12, pp. 4201–4208, Dec. 1997.

[48] M. Meyer, L. Komsiyska, B. Lenz, and C. Agert, “Study of the local SOC distribution in a lithium-ion battery by physical and electrochemical modeling and simulation,” *Appl. Math. Model.*, vol. 37, no. 4, pp. 2016–2027, Feb. 2013.

[49] G. Girishkumar, B. McCloskey, A. C. Luntz, S. Swanson, and W. Wilcke, “Lithium−Air Battery: Promise and Challenges,” 02-Jul-2010. [Online]. Available: https://pubs.acs.org/doi/abs/10.1021/jz1005384.

[50] A. Manthiram, Y. Fu, S.-H. Chung, C. Zu, and Y.-S. Su, “Rechargeable lithium-sulfur batteries,” *Chem. Rev.*, vol. 114, no. 23, pp. 11751–11787, Dec. 2014.

[51] S. A. Hashim Ali and A. K. Arof, “Modeling of discharge behavior of a lithium ion cell,” *J. Alloys Compd.*, vol. 449, no. 1–2, pp. 292–295, Jan. 2008.

[52] Y. Xie, J. Li, and C. Yuan, “Multiphysics modeling of lithium ion battery capacity fading process with solid-electrolyte interphase growth by elementary reaction kinetics,” *J. Power Sources*, vol. 248, pp. 172–179, Feb. 2014.

[53] R. Wagner, N. Preschitschek, S. Passerini, J. Leker, and M. Winter, “Current research trends and prospects among the various materials and designs used in lithium-based batteries,” *J. Appl. Electrochem.*, vol. 43, no. 5, pp. 481–496, May 2013.

[54] J. Meng *et al.*, “Advances in Structure and Property Optimizations of Battery Electrode Materials,” *Joule*, vol. 1, no. 3, pp. 522–547, Nov. 2017.

[55] F. Amalraj Susai *et al.*, “Horizons for Li-Ion Batteries Relevant to Electro-Mobility: High-Specific-Energy Cathodes and Chemically Active Separators,” *Adv. Mater.*, p. 1801348, Jul. 2018.

[56] T. Huang *et al.*, “Linking particle size to improved electrochemical performance of SiO anodes for Li-ion batteries,” *RSC Adv.*, vol. 7, no. 4, pp. 2273–2280, 2017.

[57] K. Lee and D. Kum, “The impact of inhomogeneous particle size distribution on Li-ion cell performance under galvanostatic and transient loads,” in *2016 IEEE Transportation Electrification Conference and Expo, Asia-Pacific (ITEC Asia-Pacific)*, 2016, pp. 454–459.

[58] E. Pohjalainen, T. Rauhala, M. Valkeapää, J. Kallioinen, and T. Kallio, “Effect of Li4Ti5O12 Particle Size on the Performance of Lithium Ion Battery Electrodes at High C-Rates and Low Temperatures,” *J. Phys. Chem. C*, vol. 119, no. 5, pp. 2277–2283, Feb. 2015.

[59] G. S. Nagarajan, J. W. V. Zee, and R. M. Spotnitz, “A Mathematical Model for Intercalation Electrode Behavior I. Effect of Particle-Size Distribution on Discharge Capacity,” *J. Electrochem. Soc.*, vol. 145, no. 3, pp. 771–779, Mar. 1998.

[60] F. Röder, S. Sonntag, D. Schröder, and U. Krewer, “Simulating the Impact of Particle Size Distribution on the Performance of Graphite Electrodes in Lithium-Ion Batteries,” *Energy Technol.*, vol. 4, no. 12, pp. 1588–1597, Dec. 2016.

[61] S. T. Taleghani, B. Marcos, K. Zaghib, and G. Lantagne, “A Study on the Effect of Porosity and Particles Size Distribution on Li-Ion Battery Performance,” *J. Electrochem. Soc.*, vol. 164, no. 11, pp. E3179–E3189, Jan. 2017.

[62] S. Wu, B. Yu, Z. Wu, S. Fang, B. Shi, and J. Yang, “Effect of particle size distribution on the electrochemical performance of micro-sized silicon-based negative materials,” *RSC Adv.*, vol. 8, no. 16, pp. 8544–8551, Feb. 2018.

[63] A. M. Bizeray, S. Zhao, S. R. Duncan, and D. A. Howey, “Lithium-ion battery thermal-electrochemical model-based state estimation using orthogonal collocation and a modified extended Kalman filter,” *J. Power Sources*, vol. 296, no. Supplement C, pp. 400–412, Nov. 2015.

[64] C. Lin and A. Tang, “Simplification and Efficient Simulation of Electrochemical Model for Li-ion Battery in EVs,” *Energy Procedia*, vol. 104, no. Supplement C, pp. 68–73, Dec. 2016.

[65] A. Nyman, T. G. Zavalis, R. Elger, M. Behm, and G. Lindbergh, “Analysis of the Polarization in a Li-Ion Battery Cell by Numerical Simulations,” *J. Electrochem. Soc.*, vol. 157, no. 11, pp. A1236–A1246, Nov. 2010.

[66] D. Guyomard and J. M. Tarascon, “Li Metal-Free Rechargeable LiMn2 O 4 / Carbon Cells: Their Understanding and Optimization,” *J. Electrochem. Soc.*, vol. 139, no. 4, pp. 937–948, Apr. 1992.

[67] Z. Du, D. L. Wood, C. Daniel, S. Kalnaus, and J. Li, “Understanding limiting factors in thick electrode performance as applied to high energy density Li-ion batteries,” *J. Appl. Electrochem.*, vol. 47, no. 3, pp. 405–415, Mar. 2017.

[68] K. Zaghib *et al.*, “Advanced Electrodes for High Power Li-ion Batteries,” *Materials*, vol. 6, no. 3, pp. 1028–1049, Mar. 2013.

[69] C. M. Julien, A. Mauger, A. E. Abdel-Ghany, A. M. Hashem, and K. Zaghib, “Smart materials for energy storage in Li-ion batteries,” *AIMS Mater. Sci.*, 2015.

[70] R. Arvidsson, M. Janssen, M. Svanström, P. Johansson, and B. A. Sandén, “Energy use and climate change improvements of Li/S batteries based on life cycle assessment,” *J. Power Sources*, vol. 383, pp. 87–92, Apr. 2018.

[71] X. Hu, D. Cao, and B. Egardt, “Condition Monitoring in Advanced Battery Management Systems: Moving Horizon Estimation Using a Reduced Electrochemical Model,” *IEEEASME Trans. Mechatron.*, vol. 23, no. 1, pp. 167–178, Feb. 2018.

[72] K. Zaghib *et al.*, “Safe and fast-charging Li-ion battery with long shelf life for power applications,” *J. Power Sources*, vol. 196, no. 8, pp. 3949–3954, Apr. 2011.

[73] A. K. Padhi, K. S. Nanjundaswamy, and J. B. Goodenough, “Phospho-olivines as Positive-Electrode Materials for Rechargeable Lithium Batteries,” *J. Electrochem. Soc.*, vol. 144, no. 4, pp. 1188–1194, Apr. 1997.

[74] M. Farkhondeh and C. Delacourt, “Mathematical Modeling of Commercial LiFePO4 Electrodes Based on Variable Solid-State Diffusivity,” *J. Electrochem. Soc.*, vol. 159, no. 2, pp. A177–A192, Jan. 2011.

[75] T. R. Ferguson and M. Z. Bazant, “Phase Transformation Dynamics in Porous Battery Electrodes,” *Electrochimica Acta*, vol. 146, no. Supplement C, pp. 89–97, Nov. 2014.

[76] M. Mastali, M. Farkhondeh, S. Farhad, R. A. Fraser, and M. Fowler, “Electrochemical Modeling of Commercial LiFePO4 and Graphite Electrodes: Kinetic and Transport Properties and Their Temperature Dependence,” *J. Electrochem. Soc.*, vol. 163, no. 13, pp. A2803–A2816, Jan. 2016.

[77] M. Mastali Majdabadi, S. Farhad, M. Farkhondeh, R. A. Fraser, and M. Fowler, “Simplified electrochemical multi-particle model for LiFePO4 cathodes in lithium-ion batteries,” *J. Power Sources*, vol. 275, no. Supplement C, pp. 633–643, Feb. 2015.

[78] M. Safari, M. Farkhondeh, M. Pritzker, M. Fowler, T. Han, and S. Chen, “Simulation of lithium iron phosphate lithiation/delithiation: Limitations of the core–shell model,” *Electrochimica Acta*, vol. 115, no. Supplement C, pp. 352–357, Jan. 2014.

[79] X. Hu, F. Sun, and X. Cheng, “Recursive calibration for a lithium iron phosphate battery for electric vehicles using extended Kalman filtering,” *J. Zhejiang Univ.-Sci. A*, vol. 12, no. 11, pp. 818–825, Nov. 2011.

[80] X. Hu, S. Li, H. Peng, and F. Sun, “Charging time and loss optimization for LiNMC and LiFePO4 batteries based on equivalent circuit models,” *J. Power Sources*, vol. 239, pp. 449–457, Oct. 2013.

[81] V. Srinivasan and J. Newman, “Discharge Model for the Lithium Iron-Phosphate Electrode,” *J. Electrochem. Soc.*, vol. 151, no. 10, pp. A1517–A1529, Oct. 2004.

[82] C. Wang, U. S. Kasavajjula, and P. E. Arce, “A Discharge Model for Phase Transformation Electrodes: Formulation, Experimental Validation, and Analysis,” *J. Phys. Chem. C*, vol. 111, no. 44, pp. 16656–16663, Nov. 2007.

[83] U. S. Kasavajjula, C. Wang, and P. E. Arce, “Discharge Model for LiFePO4 Accounting for the Solid Solution Range,” *J. Electrochem. Soc.*, vol. 155, no. 11, pp. A866–A874, Nov. 2008.

[84] I. Thorat, “Understanding Performance--Limiting Mechanisms in Li-ION Batteries for High-Rate Applications,” *Theses Diss.*, Apr. 2009.

[85] C. Delacourt and M. Safari, “Analysis of lithium deinsertion/insertion in LiyFePO4 with a simple mathematical model,” *Electrochimica Acta*, vol. 56, no. 14, pp. 5222–5229, May 2011.

[86] A. S. Andersson and J. O. Thomas, “The source of first-cycle capacity loss in LiFePO4,” *J. Power Sources*, vol. 97, no. Supplement C, pp. 498–502, Jul. 2001.

[87] M. Safari and C. Delacourt, “Mathematical Modeling of Lithium Iron Phosphate Electrode: Galvanostatic Charge/Discharge and Path Dependence,” *J. Electrochem. Soc.*, vol. 158, no. 2, pp. A63–A73, Feb. 2011.

[88] K. E. Thomas-Alyea, “Modeling Resistive-Reactant and Phase-Change Materials in Battery Electrodes,” *ECS Trans.*, vol. 16, no. 13, pp. 155–165, Oct. 2008.

[89] M. Farkhondeh *et al.*, “Full-Range Simulation of a Commercial LiFePO4 Electrode Accounting for Bulk and Surface Effects: A Comparative Analysis,” *J. Electrochem. Soc.*, vol. 161, no. 3, pp. A201–A212, Jan. 2014.

[90] A. Maheshwari, M. A. Dumitrescu, M. Destro, and M. Santarelli, “Inverse parameter determination in the development of an optimized lithium iron phosphate – Graphite battery discharge model,” *J. Power Sources*, vol. 307, pp. 160–172, Mar. 2016.

[91] M. Farkhondeh, M. Pritzker, M. Fowler, M. Safari, and C. Delacourt, “Mesoscopic modeling of Li insertion in phase-separating electrode materials: application to lithium iron phosphate,” *Phys. Chem. Chem. Phys.*, vol. 16, no. 41, pp. 22555–22565, 2014.

[92] M. Farkhondeh, M. Pritzker, M. Fowler, and C. Delacourt, “Mesoscopic Modeling of a LiFePO4 Electrode: Experimental Validation under Continuous and Intermittent Operating Conditions,” *J. Electrochem. Soc.*, vol. 164, no. 11, pp. E3040–E3053, Jan. 2017.

[93] M. Ender, A. Weber, and E. Ivers-Tiffée, “A novel method for measuring the effective conductivity and the contact resistance of porous electrodes for lithium-ion batteries,” *Electrochem. Commun.*, vol. 34, no. Supplement C, pp. 130–133, Sep. 2013.

[94] E. Prada, D. D. Domenico, Y. Creff, J. Bernard, V. Sauvant-Moynot, and F. Huet, “Simplified Electrochemical and Thermal Model of LiFePO4-Graphite Li-Ion Batteries for Fast Charge Applications,” *J. Electrochem. Soc.*, vol. 159, no. 9, pp. A1508–A1519, Jan. 2012.

[95] T. A. Zawodzinski, M. Neeman, L. O. Sillerud, and S. Gottesfeld, “Determination of water diffusion coefficients in perfluorosulfonate ionomeric membranes,” *J. Phys. Chem.*, vol. 95, no. 15, pp. 6040–6044, Jul. 1991.

[96] T. E. Springer, T. A. Zawodzinski, and S. Gottesfeld, “Polymer Electrolyte Fuel Cell Model,” *J. Electrochem. Soc.*, vol. 138, no. 8, pp. 2334–2342, Aug. 1991.

[97] Y. Wang and C.-Y. Wang, “Modeling Polymer Electrolyte Fuel Cells with Large Density and Velocity Changes,” *J. Electrochem. Soc.*, vol. 152, no. 2, pp. A445–A453, Feb. 2005.

[98] K. Zaghib *et al.*, “Enhanced thermal safety and high power performance of carbon-coated LiFePO4 olivine cathode for Li-ion batteries,” *J. Power Sources*, vol. 219, pp. 36–44, Dec. 2012.

[99] O. Capron, A. Samba, N. Omar, P. Van Den Bossche, and J. Van Mierlo, “Thermal Behaviour Investigation of a Large and High Power Lithium Iron Phosphate Cylindrical Cell,” *Energies*, vol. 8, no. 9, pp. 10017–10042, Sep. 2015.

[100] W. Fang, O. J. Kwon, and C.-Y. Wang, “Electrochemical–thermal modeling of automotive Li-ion batteries and experimental validation using a three-electrode cell,” *Int. J. Energy Res.*, vol. 34, no. 2, pp. 107–115, Feb. 2010.

[101] M. Ghalkhani, F. Bahiraei, G.-A. Nazri, and M. Saif, “Electrochemical–Thermal Model of Pouch-type Lithium-ion Batteries,” *Electrochimica Acta*, vol. 247, pp. 569–587, Sep. 2017.

[102] A. Melcher, C. Ziebert, M. Rohde, and H. J. Seifert, “Modeling and Simulation of the Thermal Runaway Behavior of Cylindrical Li-Ion Cells—Computing of Critical Parameters,” *Energies*, vol. 9, no. 4, p. 292, Apr. 2016.

[103] C. R. Pals and J. Newman, “Thermal modeling of the lithium/polymer battery I. Discharge behavior of a single cell,” *J. Electrochem. Soc.*, vol. 142, no. 10, pp. 3274–3281, 1995.

[104] L. Rao and J. Newman, “Heat-Generation Rate and General Energy Balance for Insertion Battery Systems,” *J. Electrochem. Soc.*, vol. 144, no. 8, pp. 2697–2704, Aug. 1997.

[105] M. Guo, G. Sikha, and R. E. White, “Single-Particle Model for a Lithium-Ion Cell: Thermal Behavior,” *J. Electrochem. Soc.*, vol. 158, no. 2, pp. A122–A132, Feb. 2011.

[106] F. Jiang, P. Peng, and Y. Sun, “Thermal analyses of LiFePO4/graphite battery discharge processes,” *J. Power Sources*, vol. 243, pp. 181–194, Dec. 2013.

[107] L. H. Saw, Y. Ye, and A. A. O. Tay, “Electrochemical–thermal analysis of 18650 Lithium Iron Phosphate cell,” *Energy Convers. Manag.*, vol. 75, pp. 162–174, Nov. 2013.

[108] L. Liu, J. Park, X. Lin, A. M. Sastry, and W. Lu, “A thermal-electrochemical model that gives spatial-dependent growth of solid electrolyte interphase in a Li-ion battery,” *J. Power Sources*, vol. 268, pp. 482–490, Dec. 2014.

[109] H. Joachin, T. D. Kaun, K. Zaghib, and J. Prakash, “Electrochemical and Thermal Studies of Carbon-Coated LiFePO4 Cathode,” *J. Electrochem. Soc.*, vol. 156, no. 6, pp. A401–A406, Jun. 2009.

[110] S. T. Taleghani, B. Marcos, and G. Lantagne, “Modeling and simulation of a commercial graphite–LiFePO4 cell in a full range of C-rates,” *J. Appl. Electrochem.*, pp. 1–12, Jul. 2018.

[111] R. Yazami, K. Zaghib, and M. Deschamps, “Carbon fibres and natural graphite as negative electrodes for lithium ion-type batteries,” *J. Power Sources*, vol. 52, no. 1, pp. 55–59, Nov. 1994.

[112] S.-C. Chen, Y.-Y. Wang, and C.-C. Wan, “Thermal Analysis of Spirally Wound Lithium Batteries,” *J. Electrochem. Soc.*, vol. 153, no. 4, pp. A637–A648, Apr. 2006.

[113] K. Kumaresan, G. Sikha, and R. E. White, “Thermal Model for a Li-Ion Cell,” *J. Electrochem. Soc.*, vol. 155, no. 2, pp. A164–A171, Feb. 2008.

[114] V. V. Viswanathan *et al.*, “Effect of entropy change of lithium intercalation in cathodes and anodes on Li-ion battery thermal management,” *J. Power Sources*, vol. 195, no. 11, pp. 3720–3729, Jun. 2010.

[115] W. B. Gu and C. Y. Wang, “THERMAL-ELECTROCHEMICAL COUPLED MODELING OF A LITHIUM-ION CELL,” 1999.